Cosmogenic ^{36}Cl Dating of Geomorphic Surfaces and Isotopic Investigation of Soil Water and Paleoclimate, Ajo Mountains, Southern Arizona

by

Beiling Liu

Dissertation

Submitted in Partial Fulfillment of the Requirements

for the Degree of

Doctor of Philosophy in Geoscience with a Specialization in Hydrology

New Mexico Institute of Mining and Technology

Socorro, New Mexico, May 1994

ACKNOWLEDGMENTS

I thank my dissertation advisor, Fred Phillips, for his full support, trust and help in the course of my study. His supervision and guidance was essential for the completion of this dissertation. I also thank my other dissertation committee members, Andrew Campbell, John Hawley and Ronald Dorn (Arizona State University), who provided valuable guidance in isotope analysis, isotope geology, geomorphology and hydrogeology.

Susan Hoines, participated most of the field investigation and sampling and measured Cl concentration for most of soil samples. Discussions with Marek Zreda, Mitch Plummer, Jiamin Wan and Chunhong Li were useful for my research.

I am grateful to Hans Claassen, Alan Riggs and Emily Taylor (USGS) for their help in the field and coordinating the project. June Fabryka-Martin (Los Alamos National Laboratory) provided valuable suggestions for my developing a model of thermal neutron distribution in unstable landforms. Pankaj Sharma and David Elmore (PRIME Lab. Purdue University) measured ^{36}Cl. I thank the personnel at Organ Pipe Cactus National Monument for permission to sample in the monument, especially, Jim Barnett provided valuable information and help.

This research was funded by U.S. Department of Energy Contract 14-08-0001-22693 in cooperation with U.S. Geological Survey Yucca Mountain Project.

Finally, I thank my husband, Changqing Wang, for his understanding, physical and spiritual support, and encouragement during the last four years.

TABLE OF CONTENT

LIST OF FIGURES ..... **vi**

LIST OF TABLES ..... **viii**

LIST OF APPENDICES ..... **ix**

ABSTRACT ..... **x**

1. INTRODUCTION **2**

2. PIEDMONT SYSTEM **5**

2.1. Alluvial Fans 5

2.2. Pediments 7

2.3. Alluvial Fans Vs. Pediments 10

3. THERMAL NEUTRON DISTRIBUTION AND COSMOGENIC ^{36}Cl IN UNSTABLE LANDFORMS **15**

3.1. Introduction 15

3.2. Model of Thermal Neutron Distribution 19

3.3. Effects of Erosion On ^{36}Cl Buildup 29

3.4. Multiple Isotope Systematics 36

3.5. Conclusions 41

4. STUDY AREA **42**

4.1. Hydrogeology 42

4.2. Geomorphology And Soils 45

5. COSMOGENIC ^{36}Cl DATING **51**

5.1. Introduction 51

5.2 Method And Material 53

5.2.1. Method 53

5.2.2. Sample Collection 54

5.2.3. Sample Preparation 55

5.3. Examination Of Chemistry Lab Procedure 56

5.4. Results 59

5.5. Discussions 66

5.5.1. Effects Of Weathering And Transport 66

5.5.2. Implication Of ^{36}Cl Age Distribution 69

5.5.3. Effects Of Inherited ^{36}Cl And Erosion 72

5.5.4. Correlation Between ^{36}Cl Ages And Paleoclimate 78

5.6. Conclusions 79

6. ^{36}Cl IN PETROCALCIC HORIZON 81

6.1. Introduction 81

6.2. Sample Collection And Preparation 83

6.3. Results And Discussions 85

6.4. Conclusions 94

7. SOIL WATER MOVEMENT 96

7.1. Introduction 96

7.2. Material And Methods 98

7.2.1. Sample Collection 98

7.2.2. Sample Preparation And Analysis 100

7.2.3. Method For Estimation Of Evaporation Rate 101

7.2.4. Methods For Estimation Of Downward Water Flux 101

7.3. Results 103

7.4. Discussions 109

7.4.1. Cool Wet Season 109

7.4.2. Summer Monsoonal Season 110

7.4.3. Dry Season 111

7.4.4. Profiles On Qf2 and Qt1 115

7.5. Estimation Of Water Flux 116

7.5.1. Steady-State Evaporation On Qt2 116

7.5.2. Downward Water Flux - Cl Mass Balance 119

7.5.3. Downward Water Flux - Bomb ^{36}Cl 126

7.6. Significance Of Soil Development For Soil Water Regime 129

7.7. Conclusions 130

8. C AND O ISOTOPES IN SOIL CARBONATE 132

8.1. Introduction 132

8.2. Carbonate Precipitation 134

8.3. Sample Collection And Analysis 136

8.4. Results 137

8.5. Discussions 139

8.5.1. O Isotope Composition 139

8.5.2. C Isotope Composition 144

8.6. Conclusions 151

9. SUMMARY OF THE STUDY 153

9.1. Surface Chronology And Geomorphic History 153

9.2. Soil Water Flux And Evolution Of Soil Moisture Regime 165

9.3. Paleoclimatic Change 166

9.4. Future Work and Suggestions 167

REFERENCES 169

APPENDICES 185

LIST OF FIGURES

Figure 2.1 Mountain-Basin Profile 11

Figure 3.1 ^{26}Al Concentration Vs. $^{26}Al/^{10}Be$ Ratio 17

Figure 3.2 Thermal Neutron Distribution In Subsurface 25

Figure 3.3 Thermal Neutron Distributions In Different Rocks 28

Figure 3.4 ^{36}Cl Production Profiles In Rocks 34

Figure 3.5 Relationship Between Apparent And Actual ^{36}Cl Ages 35

Figure 3.6 ^{36}Cl Concentration Vs. $^{36}Cl/^{10}Be$ Ratio 37

Figure 4.1 Geographic Location Of Study Area 43

Figure 4.2 Common Plants In Study Area 46

Figure 4.3 Geomorphic Map In Study Area 47

Figure 4.4 Sketch Of Soil Profiles In Study Area 49

Figure 5.1 Apparent ^{36}Cl Age Distributions 63

Figure 5.2 Comparison of ^{36}Cl Ages Between Qt2 And Debris 68

Figure 5.3 Corrected Mean ^{36}Cl Ages 77

Figure 6.1 Petrocalcic Horizon On Qf1 84

Figure 6.2 ^{36}Cl In Pore Water of Petrocalcic Horizon 87

Figure 6.3 ^{36}Cl Age Distribution In Petrocalcic Horizon 91

Figure 7.1 Photos For Sampled Soil Profiles 99

Figure 7.2 Soil Water Contents From Qt2 104

Figure 7.3 Cl Depth Profiles From Qt2 105

Figure 7.4 δ^2H And $\delta^{18}O$ Depth Profiles From Qt2 106

Figure 7.5 Soil Water and Cl Profiles from Qt1 and Qf2 107

Figure 7.6 δ^2H And $\delta^{18}O$ Profiles From Qf2 108

Figure 7.7 Relationship Between δ^2H And $\delta^{18}O$ 113

Figure 7.8 Cumulative Cl Vs. Cumulative H_2O 120

Figure 7.9 Meteoric ^{36}Cl Fallout As A Function Of Latitude 122

Figure 7.10 Pre-bomb $^{36}Cl/Cl$ Fallout Ratios 123

Figure 7.11 Bomb ^{36}Cl Profile From Qt2 127

Figure 8.1 $\delta^{13}C$ and $\delta^{18}O$ Depth Profile 138

Figure 8.2 Comparison Of O Isotopes From Carbonate And Soil Water . . 141

Figure 8.3 $\delta^{18}O$ Distribution In Time 143

Figure 8.4 T And E Effects On $\delta^{18}O$ In Carbonate 145

Figure 8.5 $\delta^{13}C$ Distribution In Time 148

Figure 8.6 Relationship Between $\delta^{18}O$ and $\delta^{13}C$ In Carbonate 149

Figure 9.1 Sketches Of Geomorphic History (Stage 1 to Stage 3) 154

Figure 9.1 Sketches Of Geomorphic History (Stage 4 to Stage 10) 158

LIST OF TABLES

Table 3.1 Neutron Parameters 26

Table 5.1 Chemical Compositions For Different Size Fractions 57

Table 5.2 Cl Concentrations In Different Size Fractions 58

Table 5.3 Apparent ^{36}Cl Ages 60

Table 5.4 Parameters For ^{36}Cl Ages From Depth Profile 65

Table 5.5 Corrected ^{36}Cl Ages 74

Table 6.1 Cl and $^{36}Cl/Cl$ for Petrocalcic Samples 86

Table 6.2 ^{36}Cl Ages for Petrocalcic Samples 89

Table 6.3 Parameters Relevant to ^{36}Cl Ages 90

Table 7.1 Evaporation Rates 118

Table 7.2 Infiltration Rates 124

LIST OF APPENDICES

Appendix 1 Field Photos Of Sampled Boulders 185

Appendix 2 Procedure For Extracting Cl 186

Appendix 3 Chemical Compositions Of Surface Samples 188

Appendix 4 Procedure For Preparing Petrocalcic Samples 193

Appendix 5 Chemical Compositions Of Petrocalcic Samples 195

Appendix 6 Soil Water Contents And Cl Concentrations 197

Appendix 7 H And O Isotope Compositions 204

Appendix 8 Bomb-^{36}Cl From Soil Profile 208

Appendix 9 Stable Isotope Expressions 210

Appendix 10 C and O Isotope Compositions 212

ABSTRACT

A simple analytical model of thermal neutron distribution in unstable landforms was developed and applied to cosmogenic ^{36}Cl accumulation dating of alluvium and pedogenic carbonates from the piedmont slopes below the western Ajo Mountains, southern Arizona. The apparent ^{36}Cl ages for individual boulders ranged from 500,000 to 13,000 yr. The sequence of ^{36}Cl ages was consistent with the apparent stratigraphic order, but groupings of similar ages on different surfaces indicated a complex pattern of reoccupation and reworking of older surfaces during the deposition of younger ones. The apparent ^{36}Cl ages for the pore water, carbonate and silicate fractions of the petrocalcic horizon from the oldest surface generally ranged between 200,000 and 550,000 yr for the depth interval between the bottom (100 cm) and the top (30 cm) of the petrocalcic horizon. This was consistent with the ages for the two older groupings from the surface boulders, suggesting long-term aggragation since the mid-Pleistocene. The youngest surface gave a distribution of ^{36}Cl ages much older than its independently-inferred mid-to-late Holocene deposition age, however, this distribution was similar to that of ^{36}Cl ages from active channels and hillslopes. The older-than-expected exposure ages are attributed to residence near the surface during very slow erosion on the mountain front. The results show that although cosmogenic nuclide accumulation can help establish chronologies for surfaces in piedmont settings, care must be used in evaluating effects of complex exposure histories.

Soil water movement in the top meter of soil was also investigated using ^{2}H, ^{18}O, and Cl on a seasonal basis during 1991 to 1992, and bomb-^{36}Cl in 1991. The results indicated that the repeated seasonal cyclic movement of soil water in the top 60-80 cm active zone tended to produce a consistent stable isotope composition for the soil water below the active zone in different seasons ($\delta^{2}H \approx -50‰$, $\delta^{18}O \approx -1‰$). This isotopic composition is probably closely related to the composition of the local average annual precipitation and correlated with the air temperature. An average evaporation rate of 35 mm/yr was determined using a steady state diffusion model, which suggested that about 80% of the soil water was lost through transpiration and first stage evaporation before quasi steady-state was reached. The long-term average infiltration rate below the active zone is about 4 mm/yr for a modern-Holocene terrace based on both chloride mass balance and bomb-^{36}Cl methods. In contrast, the average infiltration rate is only 0.02 mm/yr for the two late Pleistocene surfaces with mature soils, based on chloride mass balance. The correlation between the reduction of downward flux and the surface age suggested that increasing soil development has resulted in significant decrease of soil water infiltration and hence an increase in evaporation and surface runoff.

Oxygen-18 isotope in the soil carbonate from the four surfaces in the study area indicated a general trend of increasing $\delta^{18}O$ with decreasing surface age, suggesting that air temperature increased from mid-Pleistocene to Holocene. The $\delta^{13}C$, however, showed a reverse trend of progressive depletion with decreasing age, indicating that the environment became more favorable for C_3 plants (abundant in

temperate areas) than for C_4 plants (favor high temperature and high water stress conditions) from the mid-Pleistocene to the Holocene. This change in the C isotope composition with time for the soil carbonate is interpreted to mean that the local vegetation cover shifted from more to less grass since the mid-Pleistocene.

1. INTRODUCTION

Landform evolution in a piedmont setting is a complex process. It has been described qualitatively by evaluating the geometry of piedmont slopes, the degree of soil development, and the geomorphic characteristics (Birkeland, 1984, Ritter, 1978). These provide information of the age and history of landforms. On the other hand, however, the knowledge of absolute age is necessary in order to better understand the evolving history of piedmonts, which are important environment for human beings in the past, present and future. Cosmogenic nuclide in situ buildup in terrestrial surficial material has provided a possible numerical dating method for determining surface exposure ages and erosion rates of geomorphic surfaces (e.g., Kurz, 1986; Phillips et al., 1986; Nishiizumi et al., 1991). When a rock is exposed to cosmic rays, cosmogenic nuclides begin to form and their production increases until secular equilibrium is reached. ^{36}Cl is one of important cosmogenic nuclides used for surface exposure dating due to its long half life (3.01×10^5 years), high cross section for three nuclear production mechanisms (spallation of ^{39}K and ^{40}Ca and thermal neutron activation of ^{35}Cl), and relatively easy sample preparation. This method has been successfully applied to the samples from glacial moraines (e.g., Phillips et al., 1990; Zreda, 1994), volcanic rocks (Leavy et al., 1987; Zreda et al., 1993), and the Meteor Crater in Arizona (Phillips et al, 1991). It is possible to apply this method for determining absolute ages of geomorphic surfaces in piedmonts.

Pedogenic carbonate commonly accumulates in arid and semiarid areas. It can be considered as an age index of landforms based on carbonate content and on the structure of the carbonate layer (Gile et al., 1966; 1981; Machette, 1985). However, during the development of pedogenic carbonate many variables are difficult to quantify. Consequently, the degree of pedogenic carbonate development provides only approximate estimates of the soil or the landform age. It is desirable to directly measure the numerical ages of pedogenic carbonate or other component of the soil. By direct dating of surficial material and soil components, the geomorphic history will be better constrained, and one should achieve a more accurate picture of landform evolution. Since calcium is one of the targets for the production of cosmogenic ^{36}Cl, it is possible to use cosmogenic ^{36}Cl accumulated in pedogenic carbonate for determining the pedogenic age because high Ca concentration in carbonate allows ^{36}Cl to buildup quickly even though the cosmic-ray intensity decreases in the subsurface.

Stable O and C isotopes in pedogenic carbonate are useful indicators of the paleoenvironment and climate. Basically, O and C isotopic compositions in the pedogenic carbonate are related to meteoric water and the proportion of C_3 to C_4 vegetation, respectively (Cerling, 1984). C_4 plants favor high water stress and high temperature environmental condition, well correlated with night-time temperature in July (Teeri and Stowe, 1976). In contrast, C_3 plants favor temperate environmental conditions although these two types of plants often occur together. O isotopic composition of precipitation is correlated with the mean annual

temperature (Dansgaard, 1964), which is related to latitude, altitude, and seasonal and regional or global change in climate. By studying O and C isotopes in pedogenic carbonate from different age surfaces, the environmental and climatic fluctuations in the past can be traced.

The knowledge of soil water movement and mass transfer under present conditions is necessary to understand the climatic fluctuation and landform evolution in the past. This knowledge is also useful for analyzing contaminant transport in the vadose zone and for evaluating water resources. In arid and semiarid areas vapor transport is an important aspect of soil water movement (Phillips et al., 1988; Knowlton, 1990). ^{2}H and ^{18}O isotopes can provide information on water vapor transport in soil profile and on soil water evaporation (Allison and Barnes, 1983). On the other hand, the liquid flux of soil water can be quantitatively determined based on Cl mass balance (Stone, 1984) and on the location of bomb-^{36}Cl peak in a soil profile (Phillips et al., 1988).

The basic goal of this research is to characterize temporal and spatial evolution of a geomorphic system and the hydrogeologic conditions in piedmont slopes by combining ^{36}Cl, environmental Cl and stable C, O and H isotopes.

2. PIEDMONT SYSTEM

Piedmont is one of the common geomorphic elements in the southwestern United States. Ritter (1978) stated that "the sloping surface that connects the mountain to the level of adjacent plains is called the piedmont". It extends from the mountain front to a flood plain or playa, normally comprises an upper zone of erosional pediment connecting with the mountain front, a middle zone of transition, and a lower zone of aggradation including bajadas or alluvial fans (Dohrenwend et al., 1984; Gile et al., 1981). In general, geomorphic surfaces are genetically related to landforms that developed during an interval of relatively constant environmental conditions. Subsequent environmental changes (such as tectonism, climate and base level) will often produce a new generation of landforms (Gile et al., 1981). Pediments and alluvial fans or bajadas are very important geomorphological units in analysis of the formation and evolution of piedmonts. I will briefly review the definitions of alluvial fans and pediments, and the models of their formations proposed in previous studies.

2.1. Alluvial Fans

An alluvial fan defined by Bull (1984) is a deposit with a distinctive surface -a segment of a cone that radiates downslope from the point where the stream spreads out on the plain. A similar definition has been given by Bryan (1922), and

Cooke and Warren (1973). Alluvial fans often occur in hot desert, and they are particularly common in the western United States. Although deposition is the particular characteristic of an alluvial fan, entrenchment is always a normal process in the evolution of fans (Cooke and Warren, 1973). The morphology of alluvial fans is composed of three basic elements: channels, abandoned areas of former fan surfaces, and depositional surfaces downslope of channels. An inherent feature of fan development is the continuously changing pattern of channels and loci of deposition (Cooke and Warren, 1973). Bull (1984) indicated that the internal structure of a fan reflects the accumulation of vast numbers of beds of different extent and thickness as well as the history of changes in the locations of deposition caused by repeated entrenchment and backfilling of the trunk stream channel leading to the mountains.

Deposition on an alluvial fan can be by both debris flow and water-laid deposits (Bull, 1984). In arid and semiarid areas debris flows may be more important for fan formation because of abundant water over short periods of time at irregular intervals and steep hillslopes having insufficient vegetative cover to prevent rapid erosion (Bull, 1984). Another important condition to produce debris flows is abundant source material on the hillslopes that contains enough sand, silt and clay to provide a matrix of mud for the debris flow. There are several causes responsible for changes in fan deposition, including climate change (e.g., Lustig, 1966), tectonic movement (e.g., Denny, 1967), and the internal adjustment in fan systems (e.g., Hooke, 1968).

2.2. Pediments

The term 'pediment' was first used by McGee (1897) to describe erosional surfaces (rock plains) in Arizona. However, pediments are now used as a designation for different morphological elements by different geomorphologists. Oberlander (1989) defined that a pediment is a gently inclined slope of transportation and/or erosion that truncates rock and connects eroding slopes or scarps to areas of sediment deposition at lower levels. Bull (1984) defined pediments to be erosional surfaces formed by retreat of escarpments and by the continuing planation of rocks and sediments downslope from the escarpments. Bryan (1922), who was based on his investigation in southwestern Arizona where rock pediments are commonly and well developed adjacent to the mountain front, gave the definition that "the pediment is a slope of transportation and is usually covered with a veneer, from 18 inches to 5 feet thick, of debris in transit." Mantled pediments, often formed on granitic terrains, carry a veneer of weathered rock, typically grus or weathered granite in situ, over the still-cohesive bedrock, and the surface may be shaped by wash and rills from the adjacent inselberg residuals (Twidale, 1983). Typical rock pediments refer to exposed weathering fronts (Mabbutt, 1966; Twidale, 1983), and stripped or exhumed forms (e.g. Paige, 1912; Tuan, 1959), which lack transported veneers of other lithologies and expand in upslope direction as hillslopes erode back at constant angle (Oberlander, 1989). They are usually developed on crystalline rocks as a consequence of scarp

recession. As bedrocks are mantled by veneer of weathered rock, they are called mantled pediments (Twidale, 1983), which are formed by wash and weathering and are typical of granitic terrain. The difference between mantled and rock pediments is that mantled pediments reflect the combined effects of the lowering of the weathering front and the development of a regolith, while rock pediments are due to the stripping of that regolith. On the other hand, covered pediments evolve in sedimentary terrains and carry a veneer of coarse clasts derived from the adjacent uplands and transported to the piedmont zone (Twidale, 1983). Glacis pediments or "glacis d'erosion" are terms used more often by French researchers (e.g., Birot, 1968), indicating erosional surfaces bevelling the substrate of a caprock escarpment or truncating erodible material in contact with more resistant lithologies, and maybe veneered with exotic gravels derived from the resistant rocks. Covered pediments can present in various climatic regions although they are well represented in arid and semiarid lands (Twidale, 1983). No matter how pediments may be defined, they have some common characteristics as described by Ritter (1978):

(1) Pediments are erosional surfaces sloping away from a mountain front or escarpment;

(2) They are entirely erosional in their origin;

(3) The surfaces are usually, but not necessarily, cut on the same rocks that make up the mountain;

(4) Pediments may or may not have a thin covering of sediment;

(5) Pediments are usually found in desert regions.

An interesting point concerning pediments has been made by Bull (1984) who observed that in the Basin and Range Province of Arizona, basin fill deposited as alluvial fans could be eroded into a pediment after the tectonic activity ceased. If he is correct, present-day pediments could be remnants of older alluvial fans and the thickness of alluvium beneath such surface could then be much greater than the traditional veneer of pediments.

Three processes involved in the development of pediments were proposed by Cooke and Warren (1973), and summarized into three categories by Ritter (1978), namely headward pediment extension, basinward pediment extension (exhumation), and equilibrium. The basinward pediment extension situation describes how new pediment zones develop farther downslope. In the equilibrium situation the supply of debris to the piedmont and its removal to the base level zone is equal and the system is in a steady-state condition. In this case, the piedmont consists of both depositional features and pediments that are continuously and simultaneously being formed and destroyed. For headward pediment extension, the most typical situation for pediment development, erosional processes allow the pediment to extend into the area of the mountains. Hyperthetical lateral-planation, parallel-retreat and drainage-basin mechanisms have been proposed for producing headward pediment extension (Ritter, 1978). In the lateral planation hypothesis, streams near the mountain front are essentially at grade and have a such heavy sediment load that they cannot cut vertically but tend to migrate and erode

laterally. Extreme migration is presumed to trim back interstream bedrock spurs, forming and maintaining the piedmont angle. In response to changes imposed on the system, the streams will maintain their equilibrium condition by regrading the pediment slope. In the parallel retreat mechanism, after a mountain front achieves its diagnostic slope, weathering and erosion will maintain that declivity by making the surface retreat parallel to itself. The bedrock bench, produced as the front recedes, is swept clean by rill and sheetwash, processes that keep the angle between the mountain front and the original piedmont slope at a constant value. The drainage basin hypothesis arises from the apparent failure of either of the above two models to explain the total morphology along most mountain fronts. There appears to be no dramatic change in gradients where master channels cross the mountain front onto the pediment surface, indicating the viability of lateral planation there and negating the necessity of parallel retreat. The lateral planation will be dominant along the main drainage line, while interfluve areas evolve by weathering and wash.

2.3. Alluvial Fans Vs. Pediments

In the southwestern United States, alluvial fans and pediments commonly coexist in a piedmont system, which starts from a distinct break in slope, or piedmont angle, at the piedmont-slope-mountain-front junction, followed by well-defined rock pediments, and finally extended to alluvial fans (Figure 2.1). There

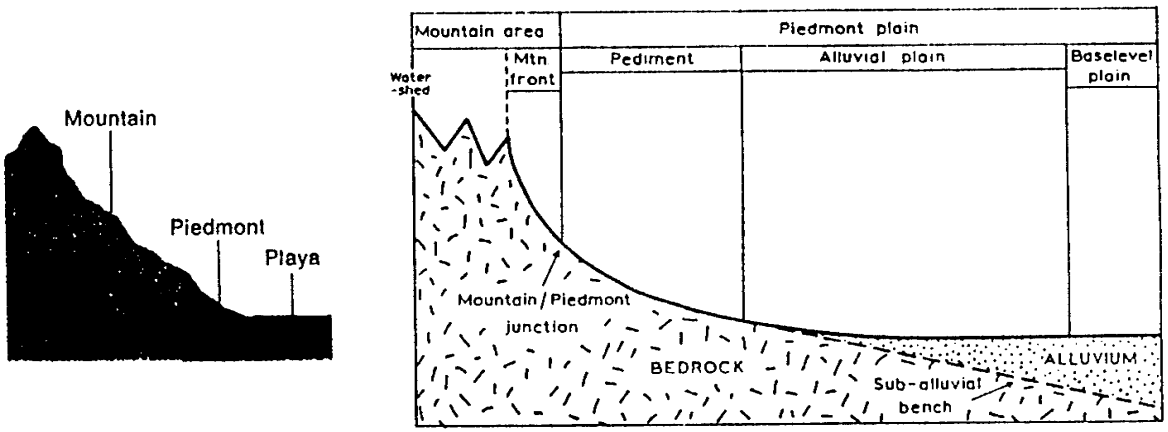

Figure 2.1 Mountain-basin profile in desert areas (Cooke and Warren, 1973). Basic components in a piedmont are pediment, bajadas or alluvial fans, and playa (base level plain).

are also some widespread units of both erosional and depositional origin that do not always neatly fit into geometric and genetic categories (Gile et al., 1981) between typical rock pediments and alluvial fans. Bull (1984) has proposed some criteria to identify whether a surface is an alluvial fan or a pediment, such as the thickness and shape of alluvium. An alluvial fan usually has thicker deposits than a pediment and often is cone-shaped. But, he also indicated that some pediments have approximately conical shapes while many fans are not fan-shaped because they are restricted by larger adjacent fans. Thus, it is difficult to distinguish between pediments and alluvial fans just based on the shape of surfaces and the thickness of deposits. In addition, it is difficult to determine the deposit thickness of a surface without subsurface information. Bull (1984) suggested to use the term alluvial slope as the landforms are of uncertain erosional or depositional origin.

Typically, piedmont slopes consist of two parts, a pediment on the side adjacent to the mountain and a bajada on the basin side (Thornbury, 1965). These two parts usually merge imperceptibly with each other. Some piedmont slopes, however, may not have a pediment portion, instead, alluvial fans are located immediately adjacent to the mountain fronts. For example, Death Valley in California is a structural basin formed by downfaulting of a large block (the "valley"), and upfaulting of the mountain ranges surrounding it. It is a tectonically unstable area where the mountains are being uplifted and Death Valley is still downward-moving today (Harris and Kiver, 1985). The conditions are optimum for fan building; large amounts of coarse, weathered materials that accumulated in the

mountains are flushed out by periodic torrential floods to build fans continuously. On the other hand, some piedmont slopes may not have alluvial fans but have extensive and well developed pediments connecting with the basin floors. Good examples may be found in regions tectonically stable for millions of years, such as Big Bend National Park (Harris and Kiver, 1985) where pediments are widespread with few and small alluvial fans.

Whether a mountain front connects to a pediment or a alluvial fan is primarily controlled by the regional tectonic situation. Based on previous investigation (e.g., Bryan, 1922; Bull, 1984), the former situation usually occurs in the tectonically stable areas for very long period of time, and the latter often occurs in the tectonically active areas where uplifting rate is significant. Bull (1984) proposed a formula to evaluate whether the control on a process is pedimentation or alluviation;

(1) Fan deposits accumulate next to the mountains as

uplift rate $\geq$ channel downcutting rate + fan deposition rate

(2) Pedimentation begins when uplift has ceased

(a) pediment is incised by the streams as

uplift rate $<<$ channel downcutting rate, and

channel downcutting rate $>$ pediment downcutting rate

(b) pediment is not incised by the stream as

uplift rate $<<$ channel downcutting rate, and

channel downcutting rate = pediment downcutting rate

He believed that this formula explains some reasons why alluvial fans are associated with tectonically active mountain fronts, whereas pediments are characteristic of regions in tectonic stability.

The channel downcutting rate is controlled by several factors including local base level, downcutting energy related to climate condition, and downcutting resistance of the eroded mass which can be veneer deposits, bedrock, or both.

3. THERMAL NEUTRON DISTRIBUTION AND COSMOGENIC ^{36}CL IN UNSTABLE LANDFORMS

3.1. Introduction

Since its inception, geomorphic research has been hampered by the difficulties of quantifying rates of geomorphic modification. Although many ingenious indirect approaches have been devised, the histories of geomorphic surfaces have generally not been determinable from measurements on the surfaces themselves. Within the past decade a major advance has been made in this direction with the capability of measuring nuclear species created by the reaction of cosmic radiation with atoms in surficial materials. This capability has been acquired by means of advances in accelerator mass spectrometry (AMS) (e.g., Brown, 1984; Elmore and Phillips, 1987) and in high sensitivity noble gas mass spectrometry (Kurz, 1986).

As a first approximation, geomorphic surfaces can be considered to fall in one of three categories: aggrading, degrading, or stable. If the rate of geomorphic modification is constant, then the amount and decay of cosmogenic nuclides that have accumulated depends only on the nuclide production rates, the time since exposure commenced, and the rate of mass removal or accumulation at the surface. Lal (1991) and Nishiizumi et al. (1991) have shown that in this case the measurement of two different cosmogenic nuclides with different half lives is sufficient to uniquely characterize both the exposure time and the erosion/

aggradation rate. If the ratio of the concentrations of the two nuclides is plotted against the concentration of one of them, a plot such as Figure 3.1 is obtained. Samples that have experienced surface modification at steady rates will fall within what Lal (1991) terms the "steady state erosion island". Within this island they will follow different trajectories, depending on the magnitude of the erosion rate. Samples having variable rates of erosion or more complicated histories may fall outside of the "island".

Although this approach to elucidating geomorphic histories is potentially a powerful one, it makes severe demands on the analytical capabilities. Analytical uncertainties of AMS measurements are typically in the range of 5 to 10 percent. The uncertainty of the ratio of two such analyses (as used in Figure 3.1) will thus typically be close to 10 percent for samples that have been exposed for long enough to accumulate an easily measurable concentration of the cosmogenic nuclide (e.g., Nishiizumi et al., 1991; Brown et al., 1992), and even larger for young samples. As indicated by Figure 3.1, an uncertainty of this magnitude in the ratio will be large enough to nearly bridge the steady state island. Useful evaluation of both erosion rate and exposure time thus demands very high analytical precision.

The high level of required precision is largely dictated by the very similar production behavior of the two nuclides. Both ^{10}Be and ^{26}Al are produced by high energy spallation reactions and their production rate declines exponentially with depth below the surface (Lal and Peters, 1967). The difference in accumulation rate indicated by Figure 3.1 is thus determined by the difference in their half lives

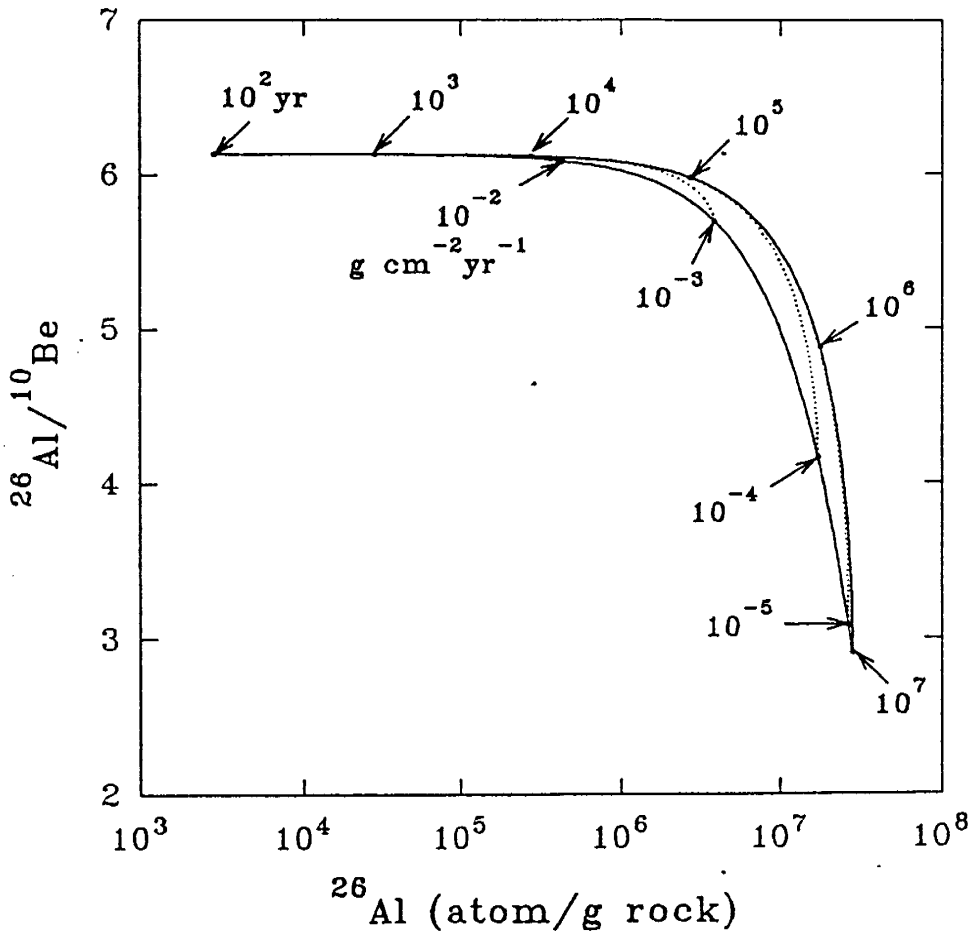

Figure 3.1 ^{26}Al concentration vs. ^{26}Al/^{10}Be ratio. The upper solid line indicates the path that rocks without erosion would follow with increasing time. The bottom solid line is the path defined by rocks at erosional equilibrium, but experiencing differing erosion rates (g cm^{-2} yr^{-1}). The dotted lines are calculated for erosion rates of 10^{-5}, 10^{-4}, 10^{-3} and 10^{-2} g cm^{-2} yr^{-1} with finite exposure age. The production rates for ^{26}Al and ^{10}Be are 36.8 and 6.0 atom (g SiO_2)$^{-1}$, respectively, adopted from Nishiizumi et al. (1989). The calculation assumed high geomagnetic latitude ($\geq$ 60°) and sea level.

(Lal, 1991). One approach to achieving better constrained sample histories without increasing analytical precision would be to use a pair of cosmogenic nuclides with different dependence of production on depth.

One cosmogenic nuclide with a non-exponential depth dependence of production is ^{36}Cl. Chlorine-36 is produced by both high energy spallation reactions and low energy (thermal or epithermal) neutron absorption by ^{35}Cl. Close to the air-land interface the low energy neutron flux is not in equilibrium with the flux of high energy cosmic-ray nucleons from which it is derived, due to the marked difference in the low-energy neutron absorption properties of air and rock. As a result, the production of ^{36}Cl by thermal neutron absorption actually increases for the first several tens of centimeters depth into rock.

Although ^{36}Cl has been used for dating stable surfaces for several years (e.g., Phillips et al., 1986), application to unstable landforms has been hampered by uncertainty regarding the actual distribution of thermal neutrons with depth (Yamashita et al., 1966). In this study a simple analytical model of low-energy neutron behavior is developed and evaluated by using the new measurements of the thermal neutron distribution in the shallow subsurface (Liu et al., 1994a). This model has been used to evaluate the suitability of ^{36}Cl in cosmogenic multiple-nuclide studies of geomorphic histories.

3.2. Model of Thermal Neutron Distribution

The changes in the flux, composition, and energy spectrum of the cosmic ray nucleons as a function of depth in the atmosphere and solid earth are the result of a complex sequence of nuclear interactions and energy transfers. Changes in the characteristics of the cosmic radiation with depth are generally gradual and smooth, but as demonstrated by the experimental data in Liu et al. (1994a), near the land surface an anomaly is observed in the low-energy neutron flux due to the differing thermal neutron absorption and diffusion properties of rocks and atmospheric gases. In this section I develop a simplified model to describe the shape of the thermal neutron profile in this region. The purpose of this model is to obtain a simple but physically-based expression for the thermal neutron flux as a function of depth that can be used in an analytical equation for cosmogenic nuclide production within unstable geomorphic surfaces. Much more comprehensive and realistic models have been presented by Lal and Peters (1967), O'Brien et al. (1978), and Dep et al. (1994). However, the numerical or analytical results of these studies are too complex to be readily used in analytical equations for cosmogenic nuclide production.

Energetic neutrons lose energy primarily by elastic scattering with targets in the media. However, a significant number of neutrons may be captured during the slowing-down process, never reaching thermal energies. The life time of a thermal neutron is proportional to its attenuation length. Therefore, the primary controls

on the thermal neutron flux are the energetic neutron flux, the capture fraction of the energetic neutrons and the attenuation length and diffusion coefficient of thermal neutrons in the media. This is analogous to the fate of the neutrons in a nuclear reactor with moderator (Glasstone, 1955). To obtain a simple mathematical equation describing the thermal neutron profile in the subsurface, the following assumptions and approximations have been made:

(1) steady-state intensity for the primary cosmic radiation,

(2) a unique energy for thermal neutrons (0.025 eV),

(3) the attenuation length for energetic cosmic-ray nucleons is same in the atmosphere as in the rock,

(4) all thermal neutrons are derived directly from spallation and evaporation neutrons produced by high-energy cosmic ray nucleons (i.e., other sources of neutrons, such as radiogenic reactions, muon capture, and photoneutrons, are negligible at the depth of interest).

Given this conceptual model and assumptions, the distribution of thermal neutron flux as a function of depth can be described by a diffusion-type equation that balances thermal neutron production and absorption (e.g., Glasstone, 1955):

$$D_i \frac{d^2\Phi_i}{dZ^2} = \frac{\Phi_i}{\Lambda_{th,i}} - p(E_{th})_i P_f \qquad 3.1$$

where

D_i = thermal neutron diffusion coefficient (g cm^{-2}), i = a (atmosphere), ss (subsurface); calculated based on Stephenson (1954).

Φ_i = thermal neutron flux (neutron cm^{-2} s^{-1}); note that this quantity is equivalent to a neutron concentration and does not constitute a net directional transport in the usual sense of a flux.

Z = cumulative mass density length (g cm^{-2}), specified Z = 0 at land surface elevation, positive downward, and negative upward

$\Lambda_{th,i}$ = effective thermal neutron attenuation length (g cm^{-2})

P_f = production rate of secondary cosmogenic neutrons (neutron g^{-1} s^{-1}), hereafter called fast neutrons (average E $\approx$ 1 MeV, up to 10 MeV or so)

$p(E_{th})_i$ = resonance escape probability (unitless) that a neutron will reach thermal energies without capture. This probability can be calculated by (Fabryka-Martin, 1988):

$$p(E_{th}) = \exp\left[-\frac{I_{eff}}{\sum \xi_i N_i (\sigma_{sc})_i}\right] \qquad 3.2$$

where I_{eff} is the effective resonance integral of the media for absorption of neutrons in the epithermal region (0.5 eV < E_n < 0.1 MeV) in unit of cm^2 g^{-1}, ξ_i is the average log decrement of energy per collision, N_i is the atomic density (atom g^{-1}) of element i, and $(\sigma_{sc})_i$ is the cross section of element i for scattering of neutrons (cm^2).

The distribution of P_f with Z is governed by:

$$\frac{dP_f}{dZ} = -\frac{P_f}{\Lambda_f} \qquad 3.3$$

where Λ_f is the effective fast neutron attenuation length (g cm^{-2}).

Given boundary condition:

$P_f = P_f(0)$ in the atmosphere at land surface elevation ($Z = 0$)

$$P_f = P_f(0) \exp\left(-\frac{Z}{\Lambda_f}\right) \qquad 3.4$$

$P_f(0)$ is a function of altitude and geomagnetic latitude (see Lal, 1991). This exponential relation is approximately accurate only for atmospheric depths greater than 200 g cm^{-2} (Lal and Peters, 1967).

The thermal neutron flux in the atmosphere above the surface is governed by:

$$D_a \frac{d^2\Phi_a}{dZ^2} = \frac{\Phi_a}{\Lambda_{th,a}} - p(E_{th})_a P_f(0) \exp\left(-\frac{Z}{\Lambda_f}\right) \qquad 3.5$$

and the thermal neutron distribution below the land surface is then governed by the equation:

$$D_{ss} \frac{d^2\Phi_{ss}}{dZ^2} = \frac{\Phi_{ss}}{\Lambda_{th,ss}} - Rp(E_{th})_a P_f(0) \exp\left(-\frac{Z}{\Lambda_f}\right) \qquad 3.6$$

where R is the ratio of thermal neutron production in subsurface to atmosphere at $Z = 0$, expressed as:

$$R = \frac{P_{th,ss}(0)}{P_{th,a}(0)} = \frac{p(E_{th})_{ss}}{p(E_{th})_a}\sqrt{\frac{A_{ss}}{A_a}} \qquad 3.7$$

where A is average atomic weight of the elements composing either air or ground.

The general solution for 3.1 is:

$$\Phi_i = C1 \exp\left(-Z\sqrt{\frac{\Sigma_{th,i}}{D_i}}\right) + C2 \exp\left(Z\sqrt{\frac{\Sigma_{th,i}}{D_a}}\right) + \frac{-Rp(E_{th})_a P_f(0)}{D_i \Lambda_f^{-2} - \Sigma_{th,i}} \exp\left(-\frac{Z}{\Lambda_f}\right) \qquad 3.8$$

$$\cong C1 \exp\left(-Z\sqrt{\frac{\Sigma_{th,i}}{D_i}}\right) + C2 \exp\left(Z\sqrt{\frac{\Sigma_{th,i}}{D_i}}\right) + \frac{Rp(E_{th})_a P_f(0)}{\Sigma_{th,i}} \exp\left(-\frac{Z}{\Lambda_f}\right)$$

where C1 and C2 are the constants of integration, $\Sigma_{th,\,i}$ is the thermal neutron macroscopic absorption cross section, which is the reciprocal of the thermal neutron effective attenuation length, and R will be one for the atmosphere.

Equation 3.8 was solved subject to the following boundary conditions:

$$(a) \quad \Phi_{ss}(\infty) = 0$$

$$(b) \quad \Phi_{ss}(0) = \Phi_a(0)$$

$$(c) \quad \frac{d\Phi_{ss}(0)}{dZ} = \frac{d\Phi_a(0)}{dZ}$$

$$(d) \quad \Phi_a(Z) = p(E_{th})_a P_f(0) \Lambda_{th,a} \exp\left(-\frac{Z}{\Lambda_f}\right) \qquad for\ Z << 0$$

The solutions for the thermal neutron flux in the subsurface and in the atmosphere are given by:

$$\Phi_{ss} = p(E_{th})_a P_f(0)\left[R\Lambda_{th,ss} \exp\left(-\frac{Z}{\Lambda_f}\right) + \frac{L_a^{-1} + \Lambda_f^{-1}}{L_a^{-1} + L_{ss}^{-1}}\left(\Lambda_{th,a} - R\Lambda_{th,ss}\right) \exp\left(-\frac{Z}{L_{ss}}\right)\right] \qquad 3.9$$

$$\Phi_a = p(E_{th})_a P_f(0)\left[\Lambda_{th,a} \exp\left(-\frac{Z}{\Lambda_f}\right) + \frac{\Lambda_f^{-1} - L_{ss}^{-1}}{L_a^{-1} + L_{ss}^{-1}}\left(\Lambda_{th,a} - R\Lambda_{th,ss}\right) \exp\left(\frac{Z}{L_a}\right)\right] \qquad 3\text{-}.10$$

where:

L_i = thermal neutron diffusion length (g cm^2) = $\sqrt{\frac{D_{th,i}}{\Sigma_{th,i}}}$

Equation 3.9 is of the form:

$$\Phi_{ss} = \Phi_{ss}^{*} \exp\left(-\frac{Z}{\Lambda_f}\right) + F\Delta\Phi^{*} \exp\left(-\frac{Z}{L_{ss}}\right) \qquad 3.11$$

where :

$$\Phi_{ss}^{*} = p(E_{th})_a P_f(0) R\Lambda_{th,ss} \qquad 3.12$$

$$\Delta\Phi^{*} = p(E_{th})_a P_f(0)\left(\Lambda_{th,a} - R\Lambda_{th,ss}\right) \qquad 3.13$$

$$F = \frac{L_a^{-1} + \Lambda_f^{-1}}{L_a^{-1} + L_s^{-1}} \qquad 3.14$$

Φ_{ss}^{*} is the thermal neutron flux that would be observed at the land surface if the thermal neutrons did not diffuse upward into the atmosphere (see Figure 3.2). $\Delta\Phi^{*}$ is the difference between the thermal neutron fluxes in the air and ground at the land surface elevation, in the absence of an interface, and F is a weighting factor that determines the balance of the endmembers in the actual interface fluxes.

In Figure 3.2 I compare the thermal neutron distribution predicted by Equation 3.11, using the parameters in Table 3.1, with the thermal neutron data obtained from the concrete block experiment (Liu et al., 1994a). Based on fully-weighted linear-squares fit of the Cd-shielded neutron counting data with depth, Λ_f was determined to be 170 g cm^{-2}. This value is in very good agreement with Lal (1991). $P_f(0)$ was treated as a fitting parameter. The values of the other parameters were

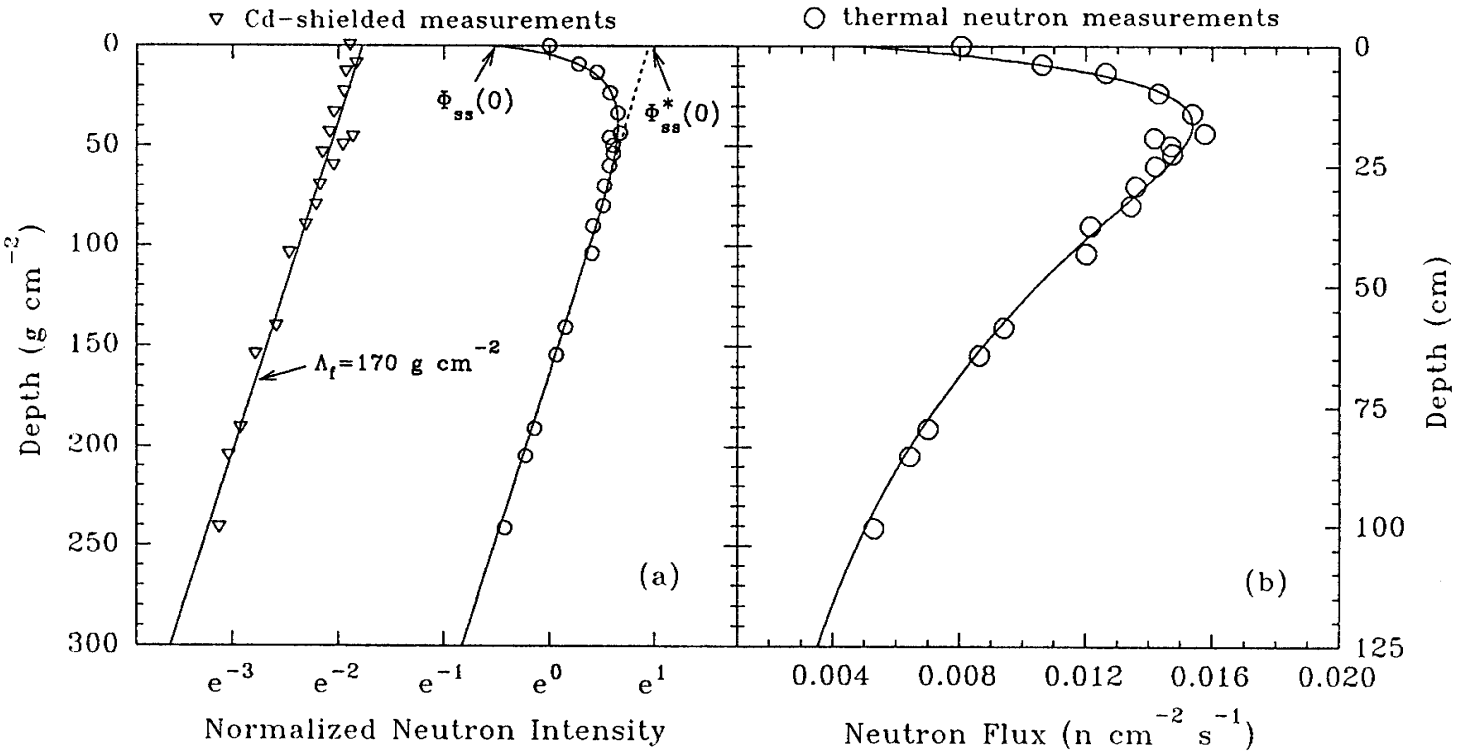

Figure 3.2 Thermal neutron distribution in subsurface. The figure is directly taken from Liu et al. (1994a). (a) Semilogarithmic plot illustrating the calculation of fast neutron attenuation length from the Cd-shielded data and the normalized thermal neutron distribution. $\Phi_{ss}(0)$ is the normalized thermal neutron flux at the land surface and $\Phi^*_{ss}(0)$ is the normalized thermal neutron flux that would have been observed if the atmosphere had the same thermal neutron absorption properties as the solid earth. (b) Arithmetic plot comparing measured data (circles) with prediction from Equation 3.9.

Table 3.1 Neutron Parameters For Different Media

Type of Medium	$\Sigma_{th,i}$ ($cm^2\ g^{-1}$)	L_i ($g\ cm^{-2}$)	$p(E_{th})_i$	R	A ($g\ mole^{-1}$)
Atmosphere	0.0602	3.9	0.56	1	14.5
Concrete	0.0066	17.0	0.97	2.23	24
Basalt	0.0083	17.1	0.93	2.22	26
Granite	0.0067	22.6	0.79	1.80	24
Carbonate	0.0042	24.2	0.91	2.09	24
Basalt*	0.0075	22.6	0.64	1.53	26
Granite*	0.0066	23.8	0.70	1.59	24
Carbonate*	0.0038	28.2	0.78	1.79	24

The Σ_{th} and $p(E_{th})$, and the chemical compositions used for calculating L, R and A of different rock types are adopted from Fabryka-Martin (1988).

* for dry condition.

calculated from the chemical analysis of the concrete (Liu et al., 1994a) and from the chemical composition of the atmosphere given by Manahan (1991), and are listed in Table 3.1. The parameters for different rock types are also included in the table.

In general, the predicted distribution in Figure 3.2 is in good agreement with the neutron-counting data. The point of greatest deviation is at the land surface, where the model underestimates the measured flux. This discrepancy may be a result of higher water content at the concrete surface. The top of the concrete slab was sprayed regularly with water during counting to prevent cracking and was then covered with plastic tarp. High water content at the surface due to condensation on the concrete under the tarp could result in more rapid thermalization of the neutrons and a higher flux.

In Figure 3.3 we compare the distribution of thermal neutron flux with depth, calculated from three different rock types using Equation 3.9 and the parameter values in Table 3.1, with the distributions calculated by Dep et al. (1994) using a much more comprehensive Monte Carlo neutron transport code. In general, the analytical result agrees well with the numerical model, indicating that Equation 3.9 should be suitable for calculating thermal neutron production in compositionally variable types of rocks.

The limitations of Equation 3.11 that are inherent in its basic assumptions should be emphasized. Probably the most critical of these is the neglect of intermediate energy interactions. Variations in the rate of neutron thermalization

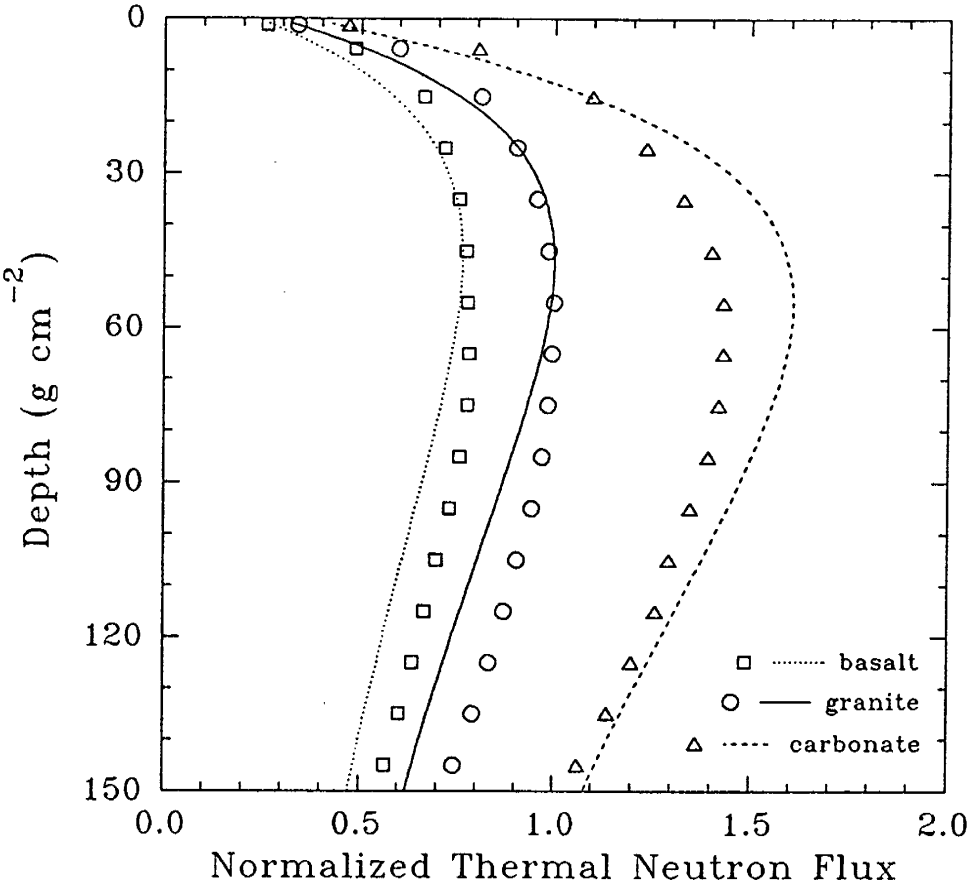

Figure 3.3 Thermal neutron distributions in rocks. The figure is directly taken from Liu et al. (1994). The lines represent the thermal neutron distributions in different rock types calculated using Equation 3.9, and the symbols represent the results calculated by the numerical model of Dep et al. (1994).

can potentially have a profound effect on the thermal neutron distribution. Hydrogen is the most effective neutron energy moderator and both theoretical (O'Brien et al., 1978) and experimental (Edge, 1959; Kodama et al., 1985) results have shown that water content can very strongly influence the thermal neutron distribution with depth. Equation 3.11 is thus most suitable for simulating the thermal neutron profile in dense, low porosity rock and will probably be significantly in error for moist soils, or circumstances where water or snow cover the surface for significant periods of time.

EFFECTS OF EROSION ON ^{36}Cl BUILDUP

Cosmogenic ^{36}Cl production in rocks is caused by spallation of ^{39}K and ^{40}Ca and thermal neutron activation of ^{35}Cl. These two components have different behaviors near the air-ground boundary as described above. The production rate due to spallation is maximum at the surface and decreases exponentially with increasing depth (Kurz, 1986):

$$P_s(Z) = P_s(0)\exp\left(-\frac{Z}{\Lambda_f}\right) = \left(\Psi_K C_K + \Psi_{Ca} C_{Ca}\right)\exp\left(-\frac{Z}{\Lambda_f}\right) \qquad 3.15$$

where P_s stands for ^{36}Cl production rate due to spallation (atom g^{-1} yr^{-1}), Ψ_K and Ψ_{Ca} are production rates for ^{36}Cl from spallation of ^{39}K (atom (mole K)$^{-1}$ yr^{-1}) and ^{40}Ca (atom (mole Ca)$^{-1}$ yr^{-1}) at the land surface respectively, and C_K and C_{Ca} represent concentrations of K and Ca in moles g^{-1}.

In contrast, the production rate due to thermal neutron activation reaches maximum at the depth that the thermal neutron flux is maximum. This can be described by:

$$P_n(Z) = \frac{f}{\Lambda_{th,ss}}\left[\Phi^*_{ss}\exp\left(-\frac{Z}{\Lambda_f}\right) + F\Delta\Phi^*\exp\left(-\frac{Z}{L_{ss}}\right)\right] \qquad 3.16$$

where P_n represents ^{36}Cl production rate due to thermal neutron activation, and f is the thermal neutron absorption fraction of ^{35}Cl, which depends on the chemical composition of the matrix (Phillips et al., 1986; Zreda et al., 1991):

$$f = \frac{\sigma_{35}N_{35}}{\Sigma_{th,ss}} \qquad 3.17$$

where σ_{35} is the thermal neutron absorption cross section of ^{35}Cl and N_{35} is the atomic concentration of ^{35}Cl.

Most landforms are not stable over long periods of time, but in many cases undergo more or less constant erosion. Erosion will result in a lower nuclide accumulation rate for nuclides produced by reactions with fast neutrons. For ^{36}Cl, however, erosion may result in a more rapid ^{36}Cl accumulation rate at the land surface than for the stable case, depending upon the magnitude of the erosion rate and the contribution of thermal neutron activation to the total production. A constant erosion rate can be represented by:

$$\frac{dZ}{dt} = -\varepsilon \qquad 3.18$$

where ϵ is the erosion rate (g cm^{-2} yr^{-1}). For a landform created at a specific time, t, the solution for 3.18 is:

$$Z = Z_o - \varepsilon t \tag{3.19}$$

where Z_o is the depth of the present land surface at t = 0.

The dependence of cosmogenic radionuclide accumulation upon the production rate and decay constant can be given by:

$$\frac{dN}{dt} = P - \lambda N \tag{3.20}$$

where t is the exposure time, N is the concentration of the existing radionuclide at time t, P is the radionuclide production rate (a function of depth beneath the land surface and erosion rate), and λ is the decay constant of the radionuclide. Substituting 3.15, 3.16 and 3.19 into 3.20:

$$\frac{dN_{36}}{dt} = \frac{f}{\Lambda_{th,ss}}\left[\Phi^*_{ss}\exp\left(-\frac{Z_o - \varepsilon t}{\Lambda_f}\right) + F\Delta\Phi^*\exp\left(-\frac{Z_o - \varepsilon t}{L_{ss}}\right)\right] + P_s(0)\exp\left(-\frac{Z_o - \varepsilon t}{\Lambda_f}\right) - \lambda_{36}N_{36} \tag{3.21}$$

The solution of 3.21 for the initial condition $N_{36} = 0$ at $t = 0$ is:

$$N_{36} = \frac{P_s(0) + f\Phi^*_{ss}/\Lambda_{th,ss}}{\varepsilon/\Lambda_f + \lambda_{36}}\left[\exp\left(-\frac{Z_o - \varepsilon t}{\Lambda_f}\right) - \exp\left(-\lambda_{36}t - \frac{Z_o}{\lambda_f}\right)\right] + \frac{fF\Delta\Phi^*_{ss}/\Lambda_{th,ss}}{\varepsilon/L_{ss} + \lambda_{36}}\left[\exp\left(-\frac{Z_o - \varepsilon t}{L_{ss}}\right) - \exp\left(-\lambda_{36}t - \frac{Z_o}{L_{ss}}\right)\right] \tag{3.22}$$

This equation can be used to calculate ^{36}Cl abundance in rocks for a scenario in which a rock buried deeply in the subsurface is suddenly exposed on the surface due to a geological event and subsequently experiences continuous and constant erosion.

If a sample is taken from a boulder surface, then Z = 0, and $Z_o = \epsilon t$. Thus, 3.22 becomes:

$$N_{36} = \frac{P_s(0) + f\Phi^*_{ss}/\Lambda_{th,ss}}{\varepsilon/\Lambda_f + \lambda_{36}}\left\{1 - \exp\left[-\left(\lambda_{36} + \frac{\varepsilon}{\Lambda_f}\right)t\right]\right\} + \frac{fF\Delta\Phi^*_{ss}/\Lambda_{th,ss}}{\varepsilon/L_{ss} + \lambda_{36}}\left\{1 - \exp\left[-\left(\lambda_{36} + \frac{\varepsilon}{L_{ss}}\right)t\right]\right\} \quad 3.23$$

Equation 3.23 contains two unknowns: erosion rate and exposure age. Two or more cosmogenic radionuclides with different half lives are therefore necessary to constrain the sample history, except in the special case in which the buildup of ^{36}Cl has reached equilibrium at a constant erosion rate so that the time variable can be dropped from the equation:

$$N_{36} = \frac{P_{s(ls)} + f\Phi^*_{ss}/\Lambda_{th,ss}}{\varepsilon/\Lambda_f + \lambda_{36}} + \frac{fF\Delta\Phi^*/\Lambda_{th,ss}}{\varepsilon/L_{ss} + \lambda_{36}} \quad 3.24$$

or the case in which there is no erosion:

$$N_{36} = \frac{P_s(0) + P_n(0)}{\lambda_{36}}\left[1 - \exp(-\lambda_{36}t)\right] = \frac{\Psi_K C_K + \Psi_{Ca} C_{Ca} + f\Phi_{ss}(0)/\Lambda_{th,ss}}{\lambda_{36}}\left[1 - \exp(-\lambda_{36}t)\right] \quad 3.25$$

where $\Phi_{ss}(0)/\Lambda_{th,ss}$ is equivalent to the thermal neutron absorption rate at the land surface.

Although the measurement of two cosmogenic nuclides in a single sample can

potentially constrain both exposure time and erosion rate, many studies have, for practical reasons, utilized only a single cosmogenic nuclide (e.g., Phillips et al., 1990; Kurz et el., 1990). Although such studies have used surface texture criteria to attempt to limit sampling to uneroded materials, the possibility must be considered that undetected erosion will cause the apparent cosmogenic age to underestimate the actual exposure age. In this respect, ^{36}Cl may be somewhat more robust than purely spallogenic nuclides. Figure 3.4 illustrates ^{36}Cl production profiles for rock compositions such that production mechanisms range from entirely spallogenic to entirely neutron activation. In reality, most rocks fall in the intermediate range. For example, the average percentage of neutron activation production for the Bloody Canyon glacial moraine boulders reported by Phillips et al. (1990) was 34 $\pm$ 11. For these intermediate proportions, the total ^{36}Cl production profile is roughly constant for the first 20 cm or more depth, and thus erosion will not reduce surface buildup to as great a degree as it will for a purely spallogenic nuclide having an exponential decrease of production with depth. In Figure 3.5 the apparent ^{36}Cl buildup age (using Equation 3.25) is compared with the actual exposure age for rocks having varying proportions of spallogenic and thermal neutron production and varying erosion rates. The figure shows that the rocks with 50 percent thermal neutron production yield more robust age estimates than those with 100 percent spallogenic production. Rocks with a very high percentage of thermal neutron production could even yield overestimates of the exposure age if erosion rates are low.

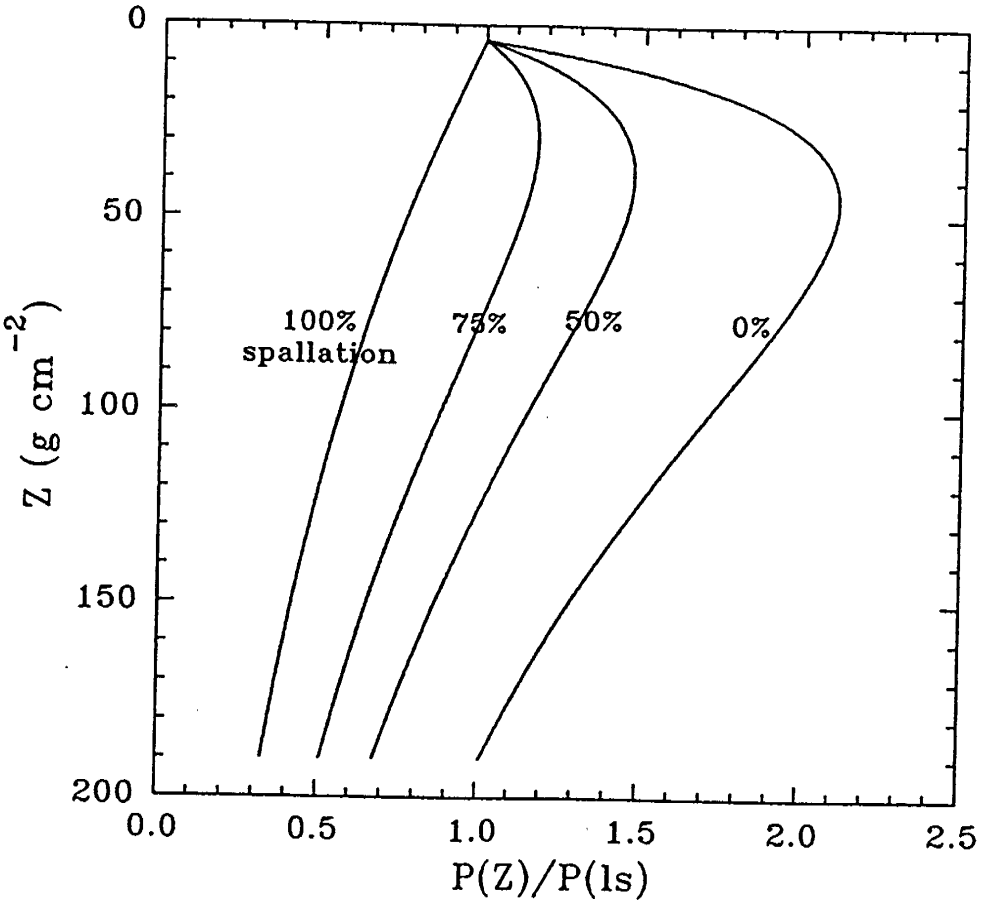

Figure 3.4 ^{36}Cl production profiles in rocks. Normalized ^{36}Cl production profiles in rocks are calculated for rock compositions such that production ranges from entirely spallogenic to entirely neutron activation using Equations 3.15 and 3.16. The production rates for spallogenic ^{36}Cl were employed from Zreda (1994). $P_f(0)$ was specified to be 732 n g^{-1} yr^{-1}.

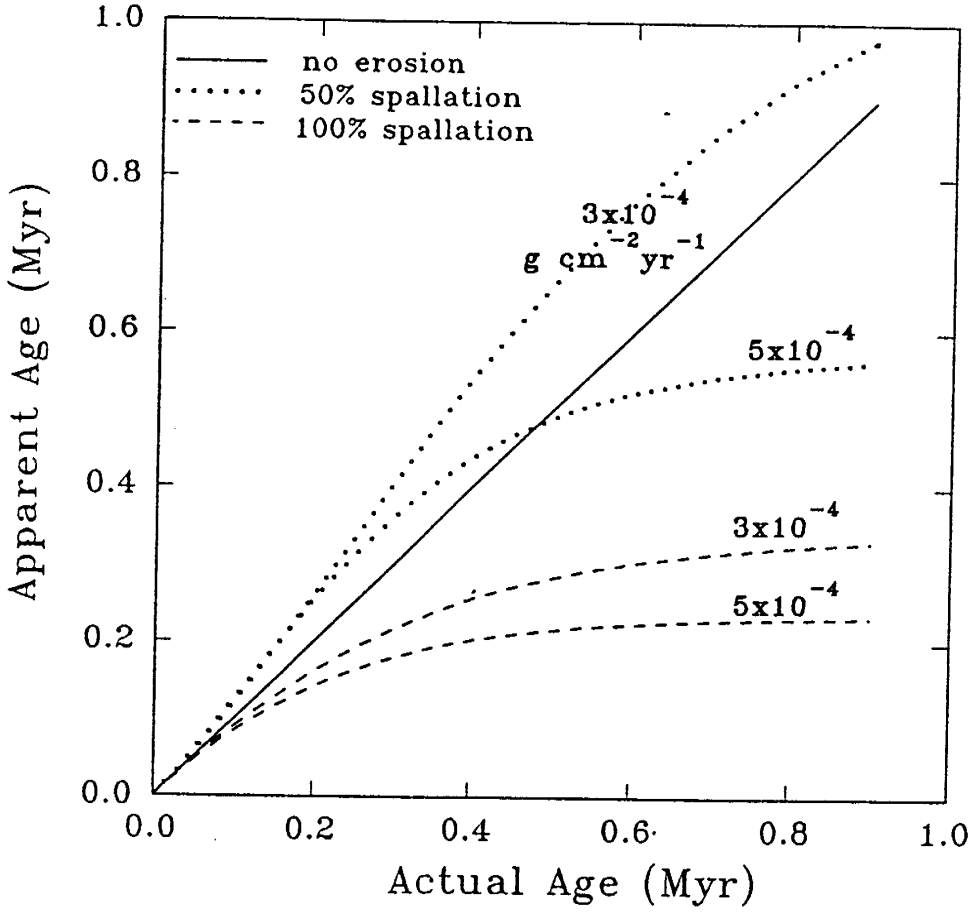

Figure 3.5 Relationship between apparent and actual ^{36}Cl ages. The apparent ages are calculated by using Equation 3.25, and the actual ages are calculated by using Equation 3.23 for 50% (dotted line) and 100% (dashed line) spallation with erosion rates of $3x10^{-4}$ and $5x10^{-4}$ g cm^{-2} yr^{-1}, respectively.

MULTIPLE ISOTOPE SYSTEMATICS

The ratio of the concentrations of two cosmogenic nuclides is a useful indication of the exposure age and erosion rate (e.g., Lal, 1991; Nishiizumi et al., 1991). The ratio of ^{36}Cl to a spallogenic nuclide, i, as a function of time and erosion rate is given by:

$$\frac{N_{36}}{N_i} = \frac{(P_s(0) + f\Phi^*_{ss}/\Lambda_{th,s})(\lambda_i + \varepsilon/\Lambda_f)\left\{1 - \exp\left[-(\lambda_{36} + \varepsilon/\Lambda_f)t\right]\right\}}{P_i(0)(\varepsilon/\Lambda_f + \lambda_{36})\left\{1 - \exp\left[-(\lambda_i + \varepsilon/\Lambda_f)t\right]\right\}} + \frac{fF\Delta\Phi^*(\lambda_i + \varepsilon/\Lambda_f)\left\{1 - \exp\left[-(\lambda_{36} + \varepsilon/L_{ss})t\right]\right\}}{\Lambda_{th,ss}P_i(0)(\lambda_{36} + \varepsilon/L_{ss})\left\{1 - \exp\left[-(\lambda_i + \varepsilon/\Lambda_f)t\right]\right\}} \quad 3.26$$

For cases where erosion is constant over such a long period that steady state is reached, Equation 3.26 reduces to :

$$\frac{N_{36}}{N_i} = \frac{(P_s(0) + f\Phi^*_{ss}/\Lambda_{th,ss})(\lambda_i + \varepsilon/\Lambda_f)}{P_i(0)(\lambda_{36} + \varepsilon/\Lambda_f)} + \frac{fF\Delta\Phi^*(\lambda_i + \varepsilon/\Lambda_f)}{\Lambda_{th,ss}P_i(0)(\lambda_{36} + \varepsilon/L_{ss})} \quad 3.27$$

For cases where erosion is negligible, Equation 3.26 reduces to:

$$\frac{N_{36}}{N_i} = \frac{\lambda_i(P_s(0) + f\Phi_{ss}(0)/\Lambda_{th,ss})\left[1 - \exp(-\lambda_{36}t)\right]}{\lambda_{36}P_i(0)\left[1 - \exp(-\lambda_i t)\right]} \quad 3.28$$

In Figure 3.6 ^{10}Be is used as an example of the behavior of ^{36}Cl together with a purely spallogenic nuclide. A ^{10}Be production rate of 6.0 atoms g^{-1} $(SiO_2)^{-1}$ yr^{-1} is assumed (Nishiizumi et al., 1989) and is normalized to the bulk rock composition. ^{36}Cl production parameters were taken from Zreda et al. (1991).

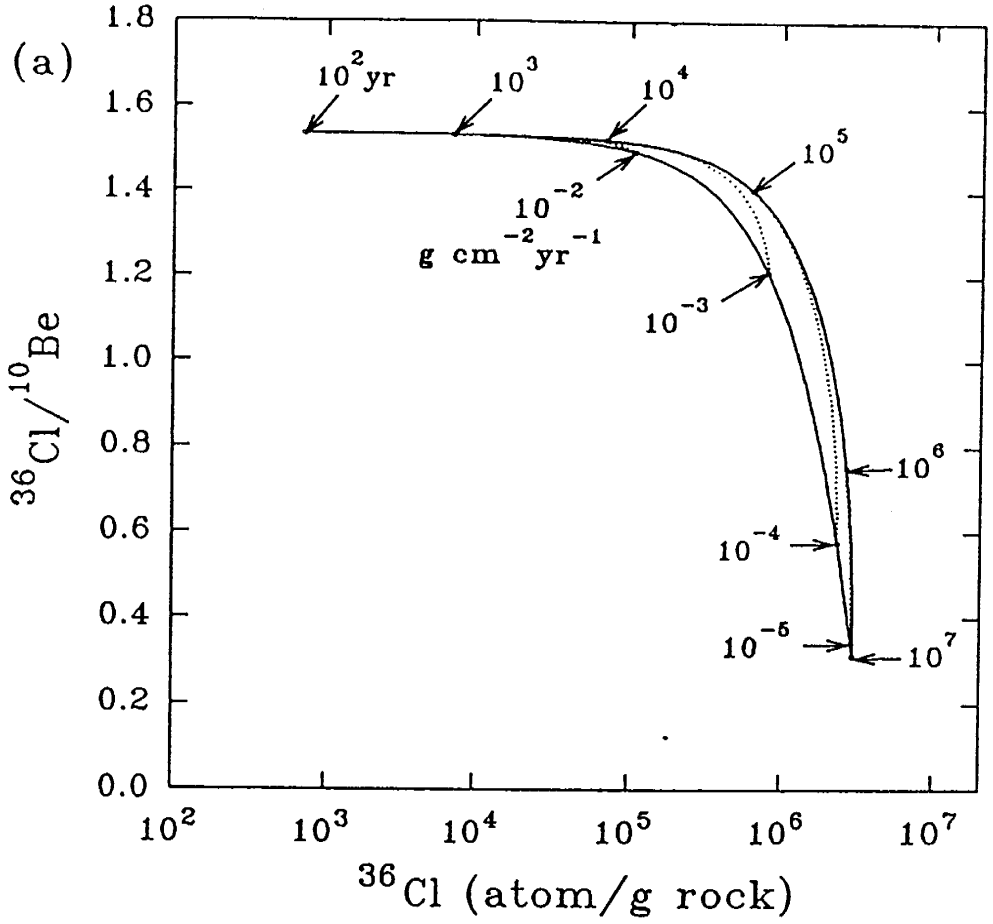

Figure 3.6 ^{36}Cl concentration vs. $^{36}Cl/^{10}Be$ ratio. The calculation assumes high geomagnetic latitude ($\geq 60°$) and sea level elevation. The production rate for ^{10}Be is taken from Nishiizumi et al. (1989) and normalized to the rock composition. (a) 100% ^{36}Cl production by spallation. The upper solid line indicates the path that a rock without erosion would follow with increasing time using Equation 3.28. The bottom solid line is the path that a rock at secular equilibrium would follow with increasing erosion rate using Equation 3.27. The dotted lines are calculated for erosion rates of 10^{-2}, 10^{-3}, 10^{-4}, 10^{-5} g cm^{-2} yr^{-1} with finite exposure ages using Equation 3.26.

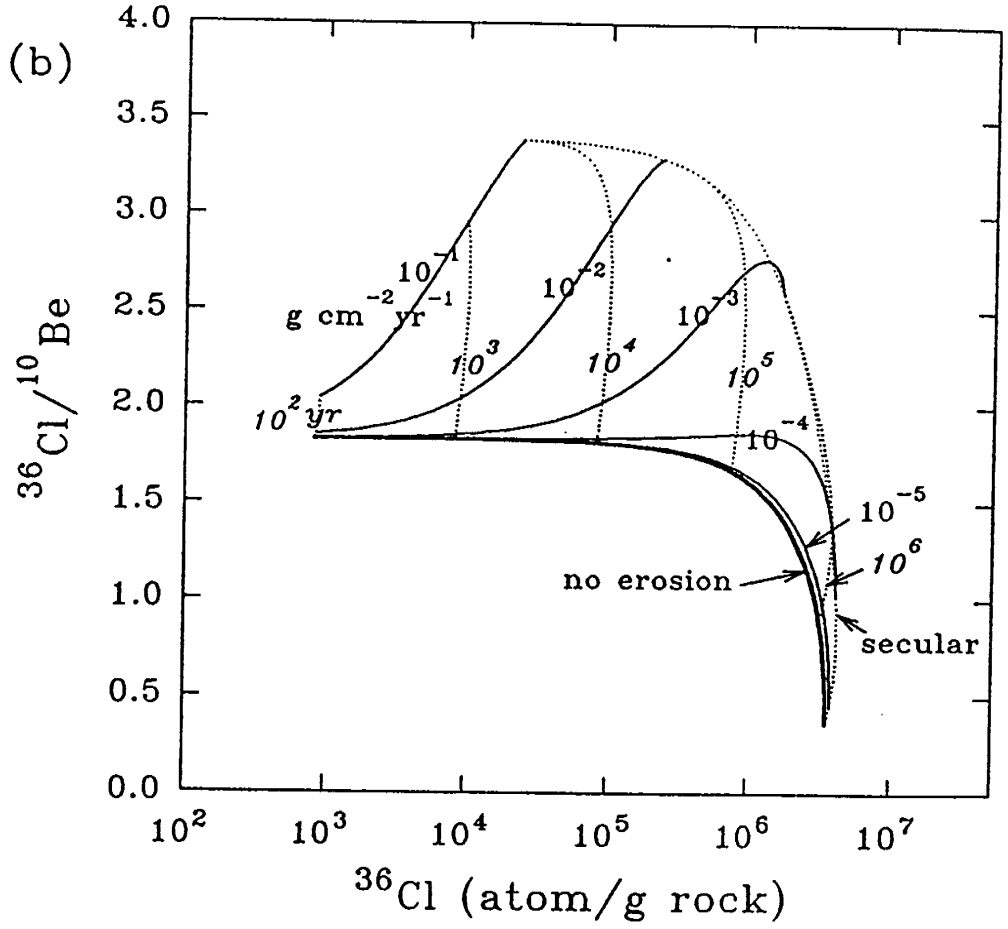

Figure 3.6(b) 50% ^{36}Cl production by spallation and 50% by neutron activation. The solid lines indicate the path that a rock with a specified erosion rate would follow with increasing time. The positions corresponding to specific times are indicated by the dotted lines. The heavy solid line indicates the case of no erosion.

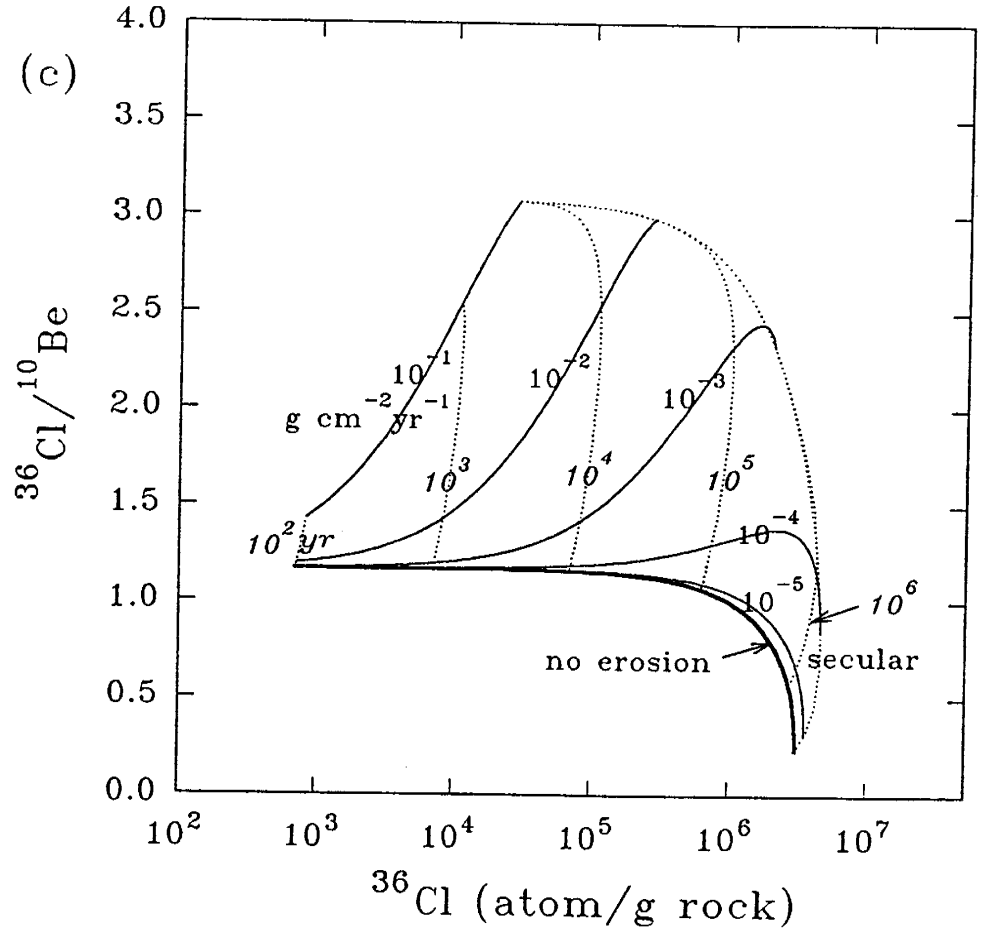

Figure 3.6(c) 100% ^{36}Cl production by neutron activation. The significance of the lines is as in (b).

Figure 3.6a shows the ratio $^{36}Cl/^{10}Be$ as a function of the ^{36}Cl concentration for a rock in which 100 percent of the ^{36}Cl production is by spallation. This pattern is very similar to that illustrated for ^{26}Al and ^{10}Be in Figure 3.1. Figure 3.6b is the same, but in this case the rock has 50 percent ^{36}Cl production by spallation and 50 percent by neutron activation. In Figure 3.6b the solid lines indicate the path that a rock with the specified erosion rate would follow with increasing time (Equation 3.26). The positions corresponding to specific times are indicated by the dotted lines. The heavy solid line indicates the case of no erosion (Equation 3.28) and the top dotted line the case of secular equilibrium ratio as a function of erosion rate (Equation 3.27). Figure 3.6c is given for a rock with 100 percent of the ^{36}Cl production by thermal neutron activation. The significance of the lines is as in Figure 3.6b. Similar results could be obtained by separating out of a rock sample minerals having predominately spallation production of ^{36}Cl (e.g., potassium feldspar) and minerals having predominately neutron activation production (e.g., quartz).

Comparison of Figure 3.6a with 3.6b and 3.6c illustrates the advantages in sensitivity that result from using both spallogenic and thermal neutron produced nuclides as a pair. For a constant level of analytical precision (say $\pm$ 10 percent for the ratio), Figures 3.6b and 3.6c permit a much more definitive resolution of the geomorphic parameters than does the spallogenic pair in Figure 3.6a. As for any approach using nuclide pairs, the uncertainty in the resulting geomorphic inferences will also depend on the uncertainty in the production parameters of both

nuclides. Multiple-nuclide studies on samples with geologically well-constrained histories would be desirable for this purpose.

3.5. Conclusions

The measurement of multiple cosmogenic nuclides is potentially useful for simultaneously determining both the age and the erosion rate of landforms. The major limitation on the implementation of this idea has been that for nuclides with similar depth dependencies of the production, the difference in their accumulation patterns is controlled only by the difference in their half-lives. In most cases the difference in accumulation is so small that only with considerable analytical effort can useful inferences be made about the geomorphic history.

We have measured the depth dependence of the thermal neutron flux and used this to calculate the depth dependence of ^{36}Cl production. This dependence of production on depth causes a marked difference in the rate of ^{36}Cl accumulation from the accumulation rate of purely spallogenic nuclides on eroding surfaces. Our calculations indicate that the application of ^{36}Cl in concert with a purely spallogenic nuclide will provide a more definitive method for elucidating geomorphic histories.

4. STUDY AREA

The study area is located on the western piedmont of the Ajo Mountains within Organ Pipe Cactus National Monument in south-central Arizona (Figure 4.1). Physiographically, it lies in the northern Sonoran Desert, one of three sub-provinces of the Southern Basin and Range province. The monument is located approximately 160 km west of Tucson and southwest of Phoenix. The southern edge of the monument coincides with the international border between the United States and Mexico. The monument covers approximately 1320 km^2, in which the elevations range from a low of about 300 m in the southwest corner near Cerro Blanco to a high of 1466 m at the top of Mont Ajo.

4.1. Hydrogeology

The western piedmont of the Ajo Mountains has a very gentle slope of approximately 1° to northwest with an abrupt transition region (about 7° slope) to the steep (40°-60°) Ajo Mountains. The study area elevation ranges between 630 and 660 m. The mountains consist entirely of mid-Tertiary volcanic rocks varying in composition from andesite to rhyolite and trachyte, and they were formed by high angle normal faulting and tilting of the middle Tertiary volcanic rocks (Shafiqullah et al., 1980). The youngest K-Ar whole rock age (for untilted rocks) is 15.2 myr (Shafiqullah et al., 1980). The study area is in the Sonoran Desert

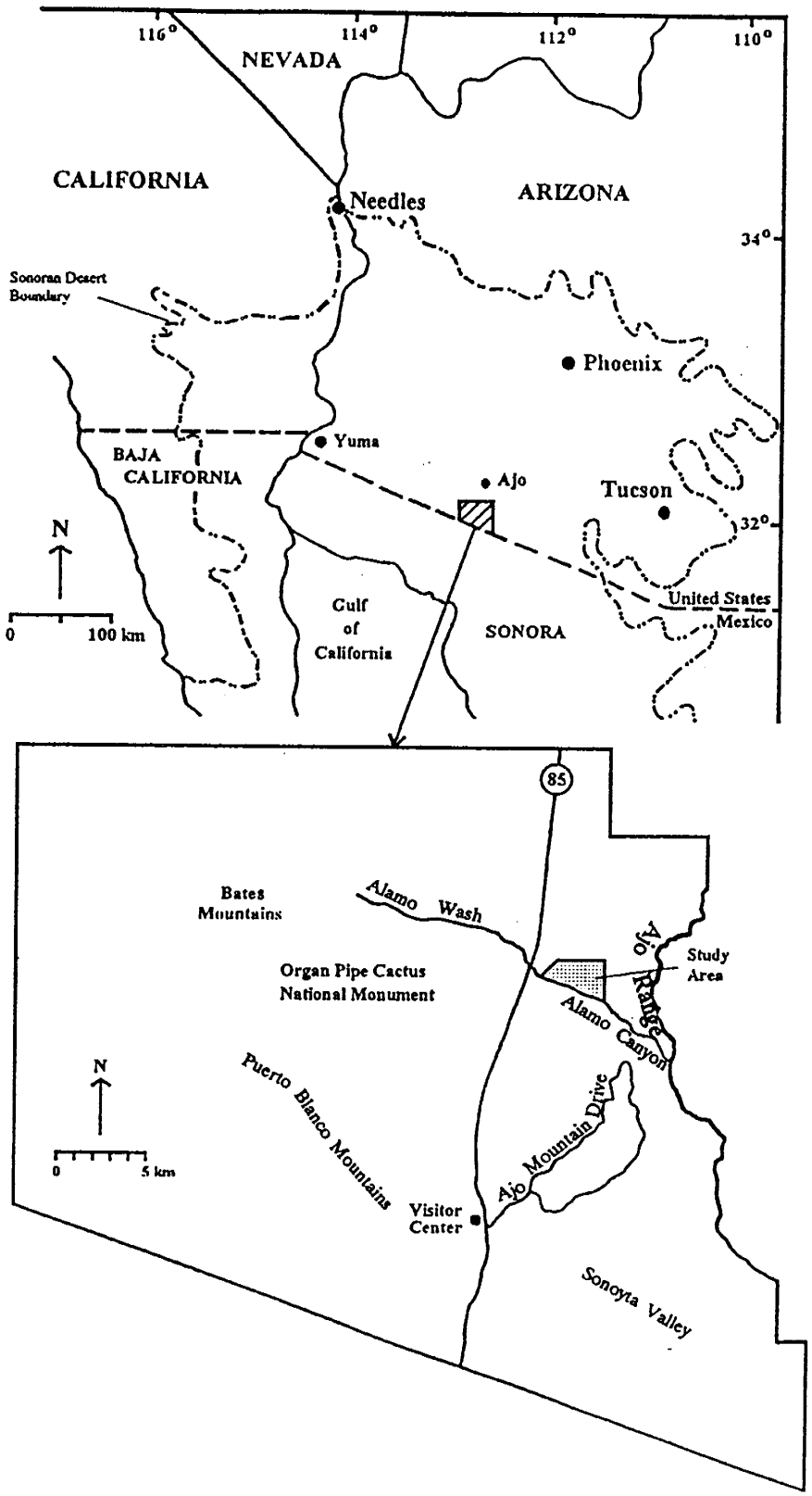

Figure 4.1 Geographic location of study area (after Dunbier, 1970; and Official Map and Guide of organ Pipe Cactus National Monument).

province, which is a tectonically stable region where active tectonics ceased approximately 6 to 10 myr ago (Shafiqullah et al., 1980; Morrison, 1991a). The base level of the trunck streams have been approximately stable through the Pleistocene (Bryan, 1922). Presumably, the landforms in this area have been developed on the structural framework of the late Tertiary geology and topography.

The climate of the Sonoran Desert is marked by extreme heat and low rainfall (Dunbier, 1968). Rainfall in this area is characteristic of the northwestern Sonoran Desert. Winter frontal storms tend to be light and steady while summer monsoonal rains are usually heavy but localized and brief thunderstorms (Dunbier, 1968 Simpson, 1991). The mean annual precipitation is about 250 mm at the Organ Pipe Cactus National Monument Park Service Center at 510 m elevation (Van Devender, 1987), 15 km south of the study area. About half of the precipitation occurs during the winter while the other half occurs mainly during the summer monsoonal season (Dunbier, 1968; Hendricks, 1985). Temperature is usually above 0 °C all year round, with mean air temperature of 10 to 13 °C in January and of 29 to 32 °C in July (Hendricks, 1985). In a broad region of the northern Sonoran Desert, the potential annual evapotranspiration is approximately 1830 mm (Montgomery and Harshbarger, 1989) while the actual annual evapotranspiration is generally 175 -250 mm (Hendricks, 1985). The low rainfall and high temperature with consequent high evapotranspiration combine to make it in the drier and hotter region of the United States.

There are a few springs and seeps within the monument, but streams are all

ephemeral, and most of them drain towards the northwest, although a few streams in the southern part of the monument go to the south into Mexico (Dodge, 1964).

Vegetation in the monument exhibits an outstanding variety of plants because two distinctively different vegetative zones of the Sonoran Desert converge here from the west, the lower Colorado Subdivision, and from the east, the Arizona upland Subdivision. The plants commonly found in the study area are cresotebush, triangle-leaf bursage, white bursage, paloverde, saguaro, cholla and ocotillo (Figure 4.2). Organ pipe cactus is often found in the hillslopes (see Figure 4.2).

4.2. Geomorphology and Soils

In this study area, four major geomorphic units have been previously mapped by Simpson (1991). They are two alluvial fan units (Qf1, Qf2) and two fluvial terrace units (Qt1, Qt2), plus active fan channels (Qfc) (Figure 4.3). Qf1 is usually located on the topographically highest points, and Qf2 is situated topographically below Qf1, but above the two terraces. The terrace Qt2 is only approximately one meter above the active stream channels while Qt1 is located above Qt2 and inset into the alluvial fan surfaces.

The degree of the soil development among the units are quite different. In general, the soils are gravelly to very gravelly sandy loam to loamy clay. Secondary carbonate commonly occur on the alluvial fans, terraces, and on the channel floors and walls, with different morphological stages for different units. The soil profile

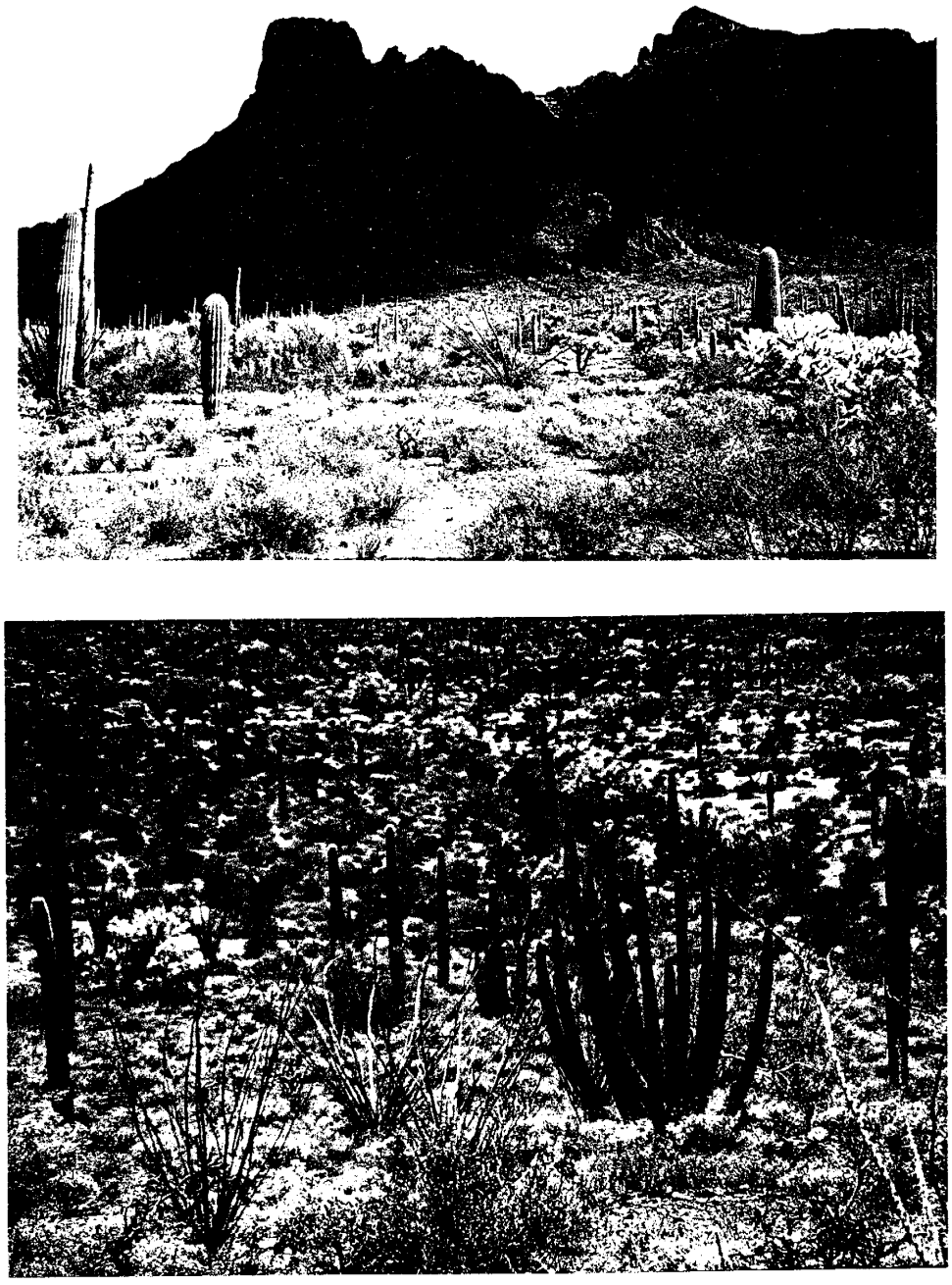

Figure 4.2 Common plants in study area.

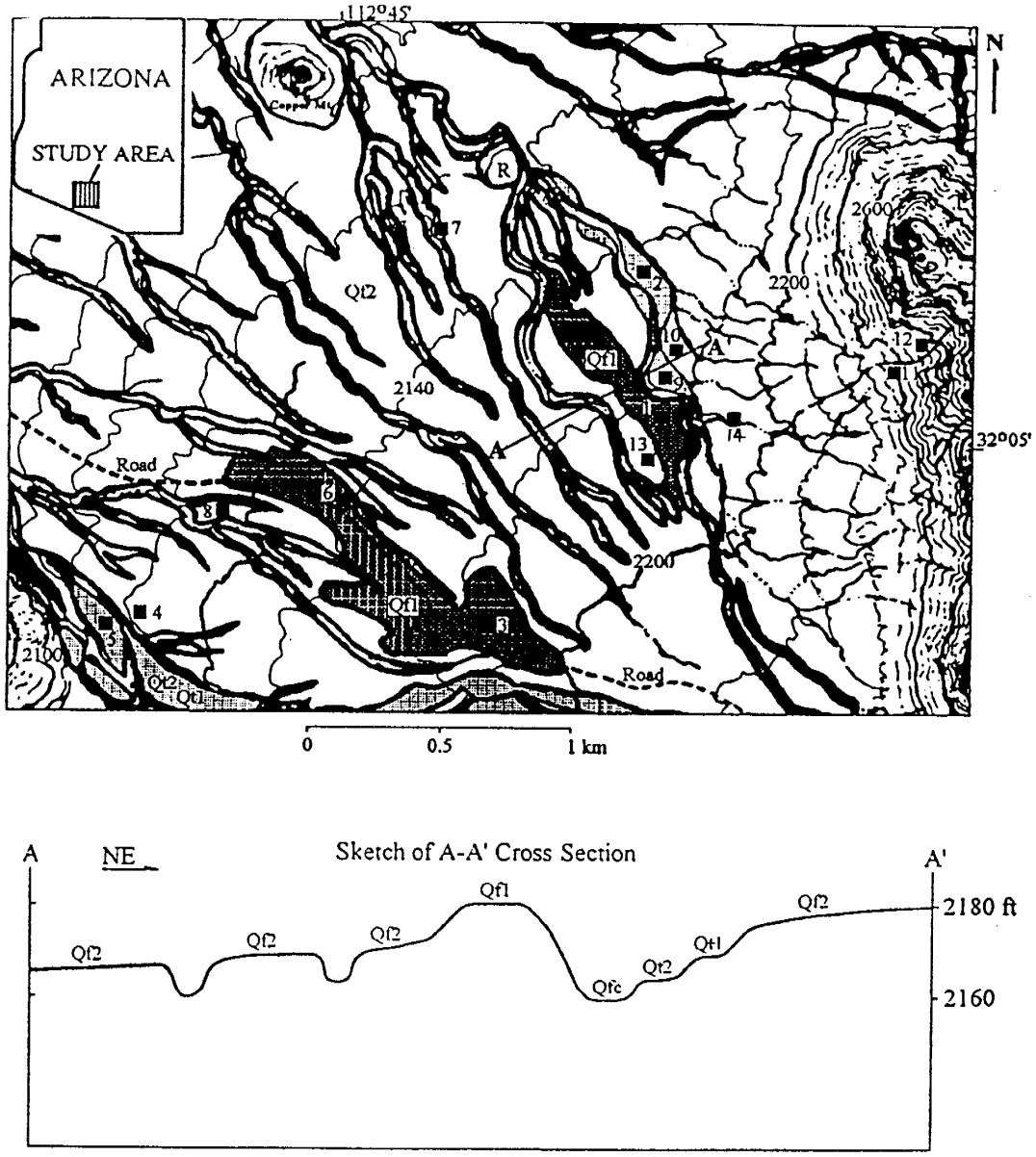

Figure 4.3 Geomorphological map in study area (after Simpson, 1991). Qf1 is the old fan surface, Qf2 the young fan surface, Qt1 the old terrace, and Qt2 the young terrace which is not distinguished in the map. R represents exposed bedrock. Sampling locations are marked by filled squares with site numbers. A cross section of the major surfaces is also shown in the map. The topographic contours are expressed in feet.

on Qf1 is characterized by a well developed petrocalcic horizon generally mantled by an A and Bk horizon approximately 30 cm thick. The petrocalcic horizon (km horizon) is massive and indurated, generally about 2 m thick with Stage IV carbonate morphology of Gile et al. (1966) or even the more advanced stage V or VI of Machette (1985). The petrocalcic horizon consists of strongly cemented volcanically-derived silicate clasts and massive or laminar layer carbonate. There is no dissolution of the carbonate or fractures observed in the calcrete from the sampled soil pit, although fractures were observed in the arroyo exposures. The soil profile on Qf2 generally does not have a petrocalcic horizon. Rather, approximately 20 to 30 cm below the surface it has either a secondary carbonate-rich layer (Bk horizon) where there is continuous pebble coatings and some interpebble fillings, or a clay rich layer (Bt horizon) where the pebbles and fine particles are partially cemented by clays with some secondary carbonate but has a strong argillic horizon approximately 30 cm thick. The Bk horizon on this surface commonly has Stage I to early stage III carbonate morphology of Gile et al. (1966) depending on the locations. The soils on Qt2 are weakly developed with Stage I to early II carbonate morphology of Gile et al (1966), indicating by thin, discontinuous pebble coatings of carbonate. Qt1 has more advanced carbonate morphology than Qt2, represented by a Bk horizon with stage II carbonate morphology of Gile et al (1966) located approximately 30 cm below the surface. A comparison of the soil profiles on Qt2, Qt1, Qf2 and Qf1 is shown in Figure 4.4.

Based on the degree of soil development, the ages of the geomorphic

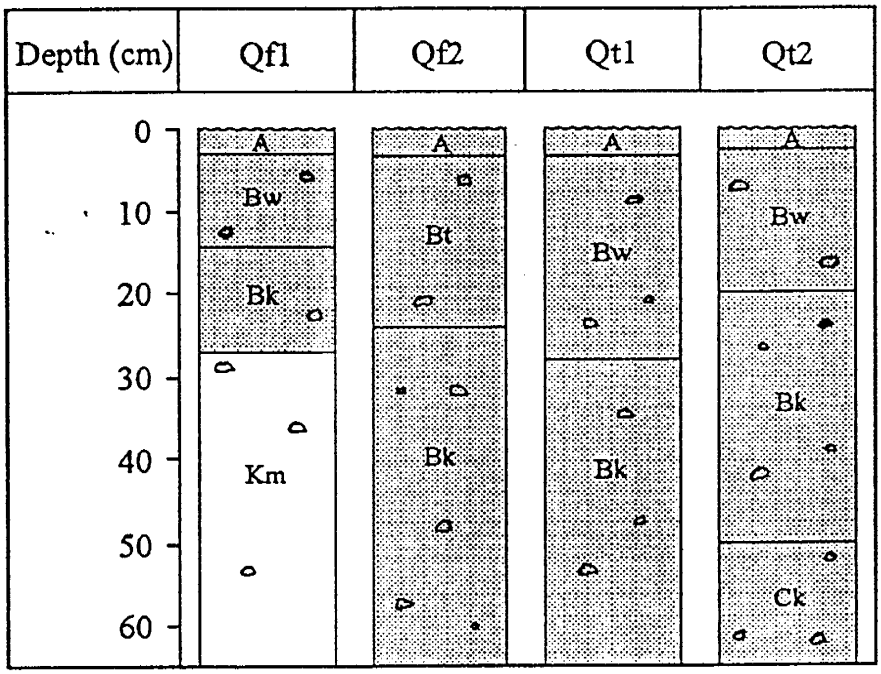

Figure 4.4 Sketch of soil profiles in study area. The profiles are based on the soils at sampling site #9 (Qt2, Qt1), #10 (Qf2) and #6 (Qf1).

units estimated by Simpson (1991) are early to middle Pleistocene for Qf1, latest Pleistocene to middle Holocene for Qf2, early to middle Holocene for Qt1, and late Holocene or modern for Qt2.

5. COSMOGENIC ^{36}Cl DATING

5.1. Introduction

In general, geomorphic surfaces are genetically related to landforms that developed during an interval of relatively constant environmental conditions. Subsequent environmental changes (such as tectonism, climate and base level) will often produce a new generation of landforms (Gile et al., 1981). Thus, alluvial surface chronology is very important for investigating geomorphic histories and associated paleoenvironmental conditions. In the Sonoran Desert the effect of tectonic movement on landform evolution since Quaternary has been considered to be negligible because significant high angle-faulting ceased well before the beginning of the Quaternary (Shafiqullah et al.; 1980, Morrison, 1991a). Presumably, climate change and internal adjustment of geomorphic system should be the primary controls of the landform modification on the basis of the overall Tertiary structure framework.

A conventional approach for determining alluvial surface chronology is to evaluate the degree of soil development combined with analysis of other morphological features of landforms, such as terrace, relief, and pavement. The degree of soil development is considered to be an age index for morphostratigraphic constraint, by which the geomorphic evolution and surface ages can be interpreted (e.g., Gile, et al., 1981; Harden et al., 1985). However, a limitation of

the soil-development constraint is that in addition to weathering time, soil profile development is also controlled by numerous other factors, especially local climate, hydrogeology, vegetation and lithology (Jenny, 1941). The difficulty of accounting for these additional variables introduces significant uncertainty into surface age estimates based on degree of soil development (Birkeland, 1984).

In the past decade, several cosmogenic nuclides in surficial materials have been applied to numerical dating of landforms (e.g., Klein et al., 1986; Kurz, 1986; Phillips et al., 1986; Jull et al., 1989) by means of accelerator mass spectrometry (AMS) and high sensitivity noble gas mass spectrometry. Recently, it has been proposed to use multiple cosmogenic radionuclides to constrain both surface age and erosion rate (Lal, 1991; Nishuiizumi et al., 1991). In addition to some physical and chemical parameters, the accumulation of cosmogenic nuclides in the surficial material depends on the surface exposure history, which is related to the geomorphic evolution of landforms. An ideal case for cosmogenic nuclide dating of landforms is that in which the surfaces have not undergone previous exposure to cosmic radiation and have been stable since they formed. In nature, some situations often meet this criteria, such as volcanic rocks, glacial moraines, and meteor craters, although the world is never ideal. Some success has been achieved in cosmogenic accumulation datings (e.g., Phillips et al., 1990; Phillips et al., 1991; Kurz et al., 1990; Nishiizumi et al., 1991; Zreda et al., 1993). In a piedmont system, a new geomorphic surface could be formed out of a older surface as a result of a depositional event induced by climatic change, tectonic activity or by

internal readjustment of the geomorphic system. The situation is thus more complicated and challenging. In this study, cosmogenic ^{36}Cl has been used to investigate alluvial surface ages in a piedmont slope of the study area. This chapter gives the ages of the alluvial surfaces based on cosmogenic ^{36}Cl dating and discusses the interpretation and limitations of ^{36}Cl for determining geomorphic histories of cosmogenic ^{36}Cl.

5.2. Methods and Material

5.2.1. Methods

Cosmogenic ^{36}Cl accumulation in surficial material is a function of time, erosion rate and the cosmogenic ^{36}Cl production rate which is controlled by cosmic-ray intensity and chemical composition of the material. By measuring ^{36}Cl accumulated in surficial material, the exposure age for a stable surface (i.e., negligible erosion) may be calculated by Equation 3.25, which is equivalent to the equations of Phillips et al., 1986:

$$t = -\frac{1}{\lambda_{36}} \ln\left[1 - \frac{(R_m - R_0)\lambda_{36}N}{EL_n(\Psi_K C_K + \Psi_{Ca} C_{Ca} + \Psi_n)}\right] \qquad 5.1$$

where t represents exposure time (yr), λ_{36} is ^{36}Cl decay constant (2.30×10^{-6}), R_m the measured $^{36}Cl/Cl$ ratio, R_0 the background level of $^{36}Cl/Cl$ ratio supported by neutrons derived from U and Th in the material, N the concentration of Cl (atoms per kg rock), EL_n the scaling factor for elevation above sea level and geomagnetic

latitude, Ψ_K and Ψ_{Ca} are production rates due to spallation of ^{39}K and ^{40}Ca (atoms per kg rock per unit concentration of K_2O and CaO) at sea level, high geomagnetic latitude ($\geq 60°$) and at land surface, C_K and C_{Ca} are concentrations of K and Ca (wt% of K_2O and CaO), respectively, and Ψ_n is the production rate due to thermal neutron activation of ^{35}Cl at sea level, high geomagnetic latitude ($\geq 60°$) and at surface. Ψ_n is determined by the chemical composition of the exposed material (see Equation 3.17) multiplied by the thermal neutron absorption rate (n per kg rock per yr).

At shallow depths, the total of cosmogenic ^{36}Cl accumulation as a function of depth beneath a stable surface may be calculated using Equation 3.15 and 3.16. It is more common for surfaces to be continuously undergoing change as a result of weathering and erosion, or deposition, than for them to be completely stable. Since cosmic-ray intensity is a function of mass shielding depth (Lal and Peters, 1967; Lal, 1988), the actual accumulation of cosmogenic nuclides will hence also be affected by erosion rate (Nishuiizumi et al., 1986; 1991; Lal, 1991). For the case of steady-state erosion, the cosmogenic ^{36}Cl accumulation as a function of erosion rate and time can be described by Equation 3.23. The steady-state erosion rate, ϵ, can be obtained from Equation 3.24 if the exposure time, t, goes to infinity.

5.2.2. Sample Collection

Collection of appropriate samples is of critical importance in order to obtain ^{36}Cl ages representative of the history of the geomorphic units. The criteria for

collecting samples amenable to the use of Equation 5.1 for calculating cosmogenic ^{36}Cl surface exposure ages are (1) the samples have remained in a stable position (i.e., not rolled or split) since they were exposed to the atmosphere; (2) they have not experienced previous exposure to cosmic radiation; (3) the land surface has remained relatively stable so that effects of soil erosion on ^{36}Cl accumulation are negligible. We sampled boulders that best met the sampling criteria. Nine surface boulders from Qf1, four from Qf2, three from Qt1 and seven from Qt2 were collected. The photos for some sampling locations and boulder samples can be found in Appendix 1. Two surface gravel samples (each sample consisting of surface clasts in the 1 - 2 cm size range) were collected from Qf2 and Qt2, and one sample of the top 10 cm soil increment was collected from Qf1. In addition, four boulder samples were collected from a large debris flow levee at the point where one of the arroyos entered the piedmont at an elevation of 730 m, one cobble was collected from the active channel at the same location, and one sample of bedrock was collected on the mountain front at an elevation of 780 m. Furthermore, five cobble samples were collected from one meter depth profile on Qt2. The depth profile of ^{36}Cl can provide an internal check of the surface stability and a check for inherited ^{36}Cl. All of the sample locations are marked with filled squares and reference numbers in Figure 4.3.

5.2.3. Sample Preparation

Preparation and $^{36}Cl/Cl$ analysis followed the procedure described in Zreda et

al. (1991), except that Cl for ^{36}Cl analysis was extracted from the rock samples by direct precipitation from the HF-HNO_3 reagent rather than by air stripping in order to achieve better recovery of Cl (see details in Appendix 2). Recently revised ^{36}Cl production rates (Zreda, 1994) were applied in the calculations, i.e., 1600 atoms (kg rock)$^{-1}$ (K_2O%)$^{-1}$ yr^{-1} and 515 atoms (kg rock)$^{-1}$ (CaO%)$^{-1}$ yr^{-1} for spallation of ^{39}K and ^{40}Ca, respectively, and 313000 n (kg rock)$^{-1}$ yr^{-1} for the thermal neutron stopping rate. The scaling factors for elevation and geomagnetic latitude were calculated based on Lal (1991). The fast neutron attenuation length of 170 g cm^{-2} was used in the relevant calculations below. The rocks were assumed to be dry, which may cause slight underestimation of the exposure age due to neglecting the enhanced rate of neutron energy moderation by the hydrogen in water (Fabryka-Martin, 1988).

5.3. Examination of Chemistry Lab Procedure

Properly handling sample preparation, extraction and purification is as importance as precisely measuring ^{36}Cl on accelerator mass spectrometry. The major procedures to achieve AgCl precipitation from silicate rocks for ^{36}Cl analysis are grading, leaching (see Zreda, 1994 for details), dissolving, precipitation and purification (see Appendix 2 for details). During grading and leaching, sample particles smaller than 200 meshes (<0.075 mm) were usually discarded. This is expected to remove meteoric Cl and secondary carbonate while the Cl cooperated

into the rocks and in situ ^{36}Cl will not be affected. This procedure will assure the measured ^{36}Cl represents the in situ ^{36}Cl accumulation. In order to test the possibility of fractionation in chemical composition and in Cl and ^{36}Cl concentrations between the discarded fine fraction and the remaining coarser fraction, three types of experiments were performed in terms of major and trace element compositions, Cl concentration and $^{36}Cl/Cl$ ratio in the samples.

Three samples in size fractions of 28 - 200 meshes (0.6 - 0.075 mm) and >200 meshes were measured for chemical compositions (Table 5.1).

Table 5.1 Chemical Compositions For Different Size Fractions

Sample#	SiO_2	TiO_2	Al_2O_3	Fe_2O_3	MnO	MgO	CaO	Na_2O	K_2O	OP_2O_5	LOI	Sum
BD 1-1	59.1	1.29	17.2	5.29	0.09	0.81	3.79	4.30	4.06	0.25	1.75	98.3
BD1-1*	58.9	1.30	16.5	6.63	0.11	1.02	3.46	4.06	4.33	0.36	2.05	99.1
BD 2	69.3	0.58	14.5	3.13	0.05	0.64	2.05	4.15	4.03	0.12	1.25	100.1
BD 2*	67.3	0.62	15.6	3.43	0.06	0.96	2.91	4.12	3.56	0.16	1.45	100.5
BD 3-1	72.5	0.19	12.9	2.05	0.08	0.24	1.10	4.12	4.29	0.05	1.55	99.3
BD3-1*	70.0	0.15	15.0	1.56	0.07	0.22	1.14	4.83	4.94	0.05	1.45	99.6

*Fine fractions smaller than 200 meshes.

In general, the chemical compositions for the two size fractions are similar, except that the fine fraction for the samples BD 2 and BD 3-1 contain slightly more

Al and Ca, reflecting weathering product and secondary carbonate in them. This result indicates that it is necessary to remove the fine particles smaller than 200 meshes to minimize the effect of meteoric ^{36}Cl in the weathering product and to correct the secondary carbonate in the silicate rocks. In addition, the result shows that this size differentiation did not affect the actual bulk rock chemical composition.

The effect of leaching on total Cl concentration in size fractions of 35-60, 60-150 and <150 meshes was also tested. The result in Table 5.2 indicates that the Cl concentrations in the three fractions are similar after leachated in deionized water three times, suggesting that the size differentiation did not affect the bulk Cl concentration in the rock samples.

Table 5.2 Cl Concentrations In Different Size Fractions

Sample#	OP 91-6 (35-60)	OP 91-6 (60-150)	OP 91-6 (>150)	OP 91-6*
Cl (ppm)	71	70	70	72
Sample#	OP90-11 (35-60)	OP90-11 (60-150)	OP90-11 (>150)	OP90-11*
Cl (ppm)	43	47	40	36

Note: Samples with * were processed by the normal procedure described in Zreda (1994).

Finally, $^{36}Cl/Cl$ ratio was measured for the 35-60 particle fraction and the leachate of the finest fraction (<150 meshes) for sample OP91-6. Compared with the $^{36}Cl/Cl$ ratio of this sample processed by the normal procedure, the ^{36}Cl ratio for the leachate (668×10^{-15}) is much lower but close to the ratio for the meteoric water in this area (400×10^{-15}) estimated by this study. The 35-60 fraction has a same ratio ($1287 \pm 53 \times 10^{-15}$) as the normally processed sample ($1223 \pm 139 \times 10^{-15}$) within analytical uncertainty. This suggests that the size differentiation does not affect the sample $^{36}Cl/Cl$ ratio, but the leachable ^{36}Cl would reduce the ratio if the meteoric ^{36}Cl were not removed by leaching.

The above experiments indicate that the sample processing procedure for the in situ ^{36}Cl study helps to remove meteoric Cl and ^{36}Cl and secondary carbonate while the intrinsically chemical property of rock samples is not affected.

5.4. Results

Table 5.3 presents the measured $^{36}Cl/Cl$ ratios, the apparent ^{36}Cl exposure ages based on Equation 5.1 and the relevant parameters for the samples from different geomorphic units. The chemical compositions of the samples can be found in Appendix 3. The ^{36}Cl ages are also plotted in a graph for comparison (Figure 5.1). The apparent cosmogenic ^{36}Cl exposure ages for the boulders on the youngest surface, Qt2, range from 13,100 to 61,900 yr with a mean of 35,300 yr. The ^{36}Cl age for a sample of the surface gravels (approximately 1-2 cm in diameter) on Qt2

Table 5.3 Apparent ^{36}Cl Ages and Relevant Parameters

Sample #	Unit	Site #	Altitude m	EL_n	$\Sigma\sigma_i N_i$ cm^2/kg	Cl ppm	K_2O %	Ca_2O %	$^{36}Cl/Cl$ $x10^{-15}$	Age $x10^3$ yr
OP 90-7 boulder	Qt2	2	640	1.41	7.43	44.6	4.12	3.99	233 ± 20	13.1 ±1.1
OP 90-8 boulder	Qt2	2	640	1.41	5.34	33.4	4.71	1.37	599 ± 41	26.6 ±1.9
OP 90-9 boulder	Qt2	2	640	1.41	7.96	58.8	4.18	4.29	488 ± 41	35.3 ±3.0
OP 90-10 boulder	Qt2	2	640	1.41	4.82	50.2	4.72	1.08	683 ± 40	43.7 ±2.7
OP 91-3 boulder	Qt2	5	630	1.40	6.15	121	3.66	2.70	266 ± 18	38.2 ±2.7
OP 91-4 boulder	Qt2	5	630	1.40	8.81	72.8	4.51	3.09	320 ± 14	28.5 ±2.7
OP 91-5 boulder	Qt2	5	630	1.40	5.55	341	5.00	1.05	268 ± 23	61.9 ±5.7
BD 6cm cobble	Qt2	2	640	1.41	7.48	46.0	4.06	3.79	726 ± 38	45.7 ±2.5
BD 28cm cobble	Qt2	2	640	1.41	8.15	57.1	3.46	4.45	353 ± 16	26.9 ±1.3
BD 50cm cobble	Qt2	2	640	1.41	5.92	32.2	4.26	1.32	282 ± 16	19.0 ±1.1
BD 86cm cobble	Qt2	2	640	1.41	4.75	10.4	4.02	1.15	848 ± 34	35.0 ±1.5

Table 5.3 Cont.

BD 114cm cobble	Qt2	2	640	1.41	5.60	15.1	4.41	1.29	359 ± 22	24.4 ±1.1
S5 #1 gravel	Qt2	7	630	1.40	5.50	36.8	4.56	1.74	855 ± 58	42.8 ±3.1
OP 392-2 boulder	Qt1	9	650	1.42	5.85	84.1	3.29	3.56	517 ± 21	57.8 ±2.5
OP 392-3 boulder	Qt1	9	650	1.42	5.88	79.1	4.18	2.41	972 ± 69	100 ±8
OP 1092-5 boulder	Qt1	2	650	1.42	5.11	49.8	3.37	3.21	474 ± 31	33.5 ±2.3
OP 91-1 boulder	Qf2	4	640	1.41	5.36	57.4	6.23	1.62	2050 ±167	134 ±13
OP 91-2 boulder	Qf2	4	640	1.41	5.56	86.4	3.35	3.72	1051 ± 35	130 ±5
OP 392-4 boulder	Qf2	10	660	1.43	9.15	63.9	4.21	3.80	1010 ± 40	85.1 ±3.7
OP 1092-3 boulder	Qf2	13	660	1.43	4.62	36.8	4.51	0.79	971 ± 45	49.8 ±2.4
S3 #1 gravel	Qf2	8	650	1.42	5.28	42.2	4.49	1.05	605 ± 71	34.8 ±4.2
OP 90-1 boulder	Qf1	1	650	1.42	5.05	57.4	2.03	2.21	1009 ± 78	125 ±11
OP 90-2 boulder	Qf1	1	650	1.42	6.27	1226	4.28	1.56	863 ± 68	521 +88/-73
OP 90-3 boulder	Qf1	1	650	1.42	4.95	55.5	5.31	1.23	1978 ±130	138 ±11
OP 90-5 boulder	Qf1	1	660	1.43	8.67	53.1	4.63	3.18	3206 ±219	267 +26/-25

Table 5.3 Cont.

OP 90-11 boulder	Qf1	3	650	1.42	5.30	35.7	5.27	2.19	5191 ±379	280 +30/28
OP 90-12 boulder	Qf1	3	660	1.43	6.35	110	3.60	3.40	349 ± 22	45.6 ±3.0
OP 90-13 boulder	Qf1	3	670	1.44	5.97	55.1	3.60	2.76	2399 ±150	228 +19/-18
OP 91-6 boulder	Qf1	6	650	1.42	6.58	71.6	3.48	3.29	1223 ±139	133 +18/-17
OP 91-7 boulder	Qf1	6	650	1.42	5.08	36.5	4.55	3.68	2131 ±186	99.8 ±10
CP#2 5cm soil	Qf1	6	650	1.42	6.95	41.4	3.66	3.09	1090 ±110	78.1 +8.7/-8.5
OP 392-5 cobble	Qfc	11	730	1.51	5.20	36.3	4.32	1.43	840 ± 80	43.9 ±4.4
OP 392-12 boulder	Deb.	11	730	1.51	7.25	38.6	3.85	4.75	517 ± 75	26.2 ±3.9
OP 392-13 boulder	Deb.	11	730	1.51	8.16	46.3	3.72	4.29	442 ± 22	28.0 ±1.4
OP 1092-1 boulder	Deb.	11	730	1.51	7.08	54.7	3.82	3.93	182 ± 8	12.9 ±0.6
OP 1092-2 boulder	Deb.	11	730	1.51	6.85	65.6	3.59	4.19	103 ± 10	8.7 ±0.8
OP 392-10 bedrock	Bed.	12	780	1.57	7.66	49.4	3.33	4.81	550 ± 62	38.8 ±4.6

Note: The age uncertainty includes only the analytical uncertainty of the measured $^{36}Cl/Cl$ ratio.

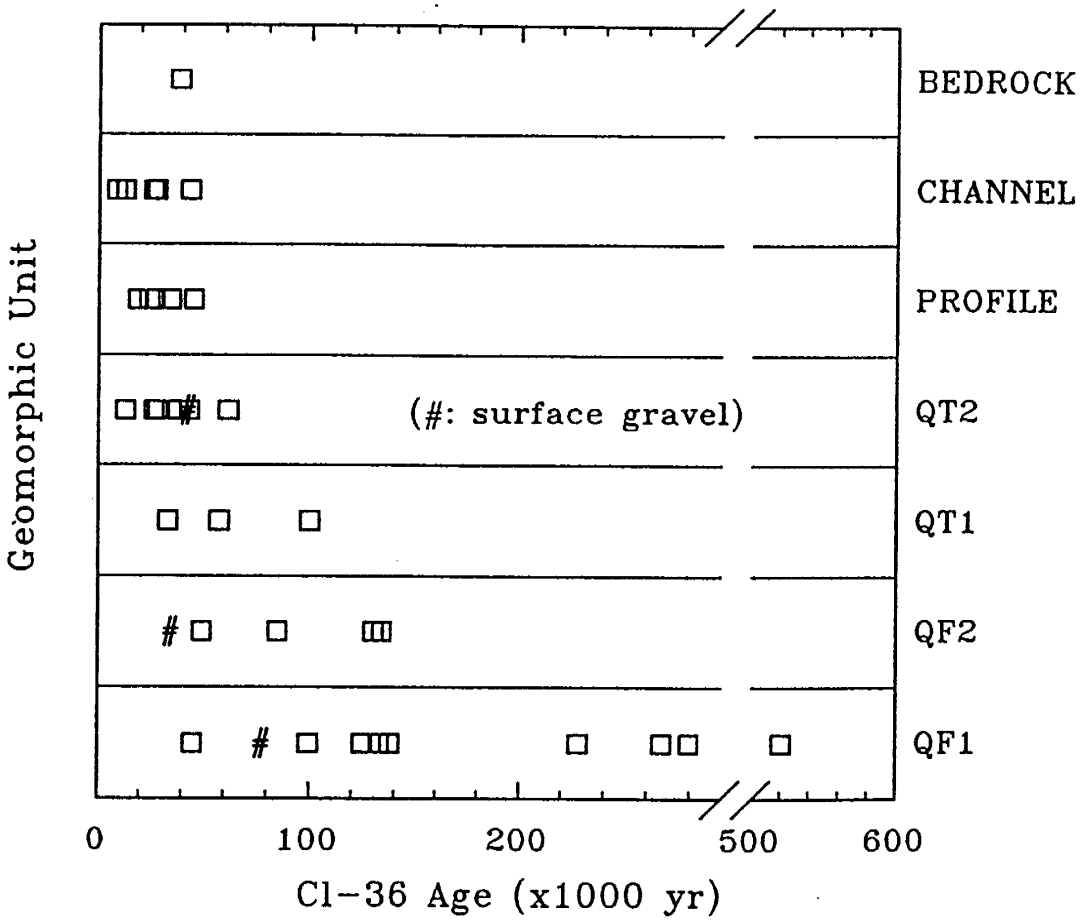

Figure 5.1 Apparent ^{36}Cl age distributions. Each square represents a single sample measurement. Channel represents sampling site #11 where samples were collected from a active stream channel entering the mountain front and from the debris flow levee by the channel. Profile represents a cobble profile collected from a soil pit at sampling site #2 on Qt2.

is 42,800 yr, close to the mean ages of the boulders. Qt1 has ^{36}Cl ages ranging from 33,500 to 100,000 yr with a mean of 63,800 yr. Qf2 has ^{36}Cl ages ranging from 49,800 to 134,000 yr with a mean of 99,700 yr. The ^{36}Cl age for a sample of the surface gravels on Qf2 is 34,800 yr, within the age range for the youngest surface, Qt2. The ^{36}Cl ages for the boulders on the oldest surface, Qf1, vary from 45,600 to 521,000 yr. The sample collected from 0-10 cm soil depth interval on this surface gives an apparent age of 78,100 yr using the depth-dependent ^{36}Cl production equations 3.15 and 3.16. The ^{36}Cl ages for the debris flow levee range from 8,700 yr to 28,100 yr. The apparent age of the cobble sample in the active channel is 43,900 yr, and of the bedrock sample is 38,800 yr. The average age of all the debris flow, channel, and bedrock samples is 26,400 yr. By using equations 3.15 and 3.16 for the ^{36}Cl production rates of the samples in the depth profile on Qt2, with the relevant parameters given in Table 5.4, the apparent ^{36}Cl ages of the cobble samples range from 45,700 to 19,000 yr, with a mean of 30,200 yr. This is in good agreement with that of the boulder samples on this surface. The ages of the cobbles are randomly distributed as a function of depth and show no trend.

In general, the relative distribution of the apparent cosmogenic ^{36}Cl ages for the four surfaces are consistent with Simpson's chronosequence determined by soil correlation. That is, Qt2 is the youngest surface, Qf1 is the oldest surface, and Qt1 and Qf2 are intermediate. However, the apparent ^{36}Cl ages for all the surfaces, except for the oldest surface (Qf1), are much older than the soil correlation-based estimates given by Simpson (1991).

Table 5.4 Parameters for ^{36}Cl Ages from Depth Profile

Sample #	Depth (cm)	$p(E_{th})$	Σ_{th} (cm^2/g)	L (g/cm^2)
BD 6cm	6	0.904	0.00748	20.05
BD 28cm	28	0.943	0.00592	21.31
BD 50cm	50	0.903	0.00475	26.46
BD 86cm	86	0.936	0.00560	22.42
BD 114cm	114	0.919	0.00815	18.43

Λ_f was specified to be 170 g/cm^2, the average atomic weight was assumed to be 24 g/mole, and $P_f(0)$ was assumed to be 732 n/g/yr at sea level and high geomagnetic latitude ($\geq 60°$) based on Liu et al. (1994a).

5.5. Discussions

An ideal and simple case for cosmogenic ^{36}Cl buildup history is one in which the rocks have been on a stable surface after being suddenly exposed to cosmic radiation due to excavation from a deep buried position. In this study area, the transport rate of alluvium is expected to be very low due to the flat, gentle gradient of the piedmont slope. The cosmogenic ^{36}Cl buildup in the rock samples must be affected by this slow transport. Also, as the study area is in a tectonically stable region, and the piedmont slope has been developing for millions of years, it is possible that very young surfaces could coexist with very old surfaces which might have been reworked several times since they formed. Thus, it is not surprising for this area to yield the complicated ^{36}Cl age distribution encountered in this study.

5.5.1. Effects of Weathering and Transport

The late Holocene age assignment of Simpson (1991) for the Qt2 terrace was based on its elevation approximately one meter above the active channel, the well-preserved bar-and-swale microtopography, and the merely incipient degree of soil development. This assignment is clearly in conflict with the average apparent ^{36}Cl exposure age of 35,300 yr ($\pm$15,000 yr) for this surface. We propose three hypotheses that could explain this discrepancy: (1) the soil development in this area is for some reason much slower than in other areas, and the terrace really was deposited approximately 35,000 years ago; (2) erosion from the mountain slopes is

episodic and the 34,000 yr apparent ^{36}Cl age actually represents the time between the most recent (late Holocene) erosion event (and subsequent deposition to form the terrace) and the previous event; (3) the rock surface on the mountain slope has been eroding steadily, and the ^{36}Cl was accumulated during the erosion process.

A comparison of the ^{36}Cl ages between the samples of Qt2 and those of the active channel, the debris flow and the bedrock shows that they share very similar ^{36}Cl age distributions (Figure 5.2). This indicates that the "excess ^{36}Cl" was inherited and not accumulated after deposition of Qt2. In addition, the random age distribution along the depth profile on Qt2 also suggests an inherited origin of ^{36}Cl in the cobble samples, rather than accumulation of ^{36}Cl in the samples after deposition of Qt2, or than accumulation of ^{36}Cl during a successively depositional process. Furthermore, there is no independent evidence to indicate that soil development in this area is slower than elsewhere in the region, nor is there any apparent reason why it should be slower. Finally, our own evaluation of the good preservation of the depositional bar-and-swale topography supports Simpson's (1991) age estimate, although the evaluation of the soil development at site #2 (Figure 4.3) in this study indicates that the age may be slightly older than late Holocene. All of these lines of evidence therefore suggest that the first explanation for the ^{36}Cl age of Qt2 is unlikely.

Samples OP1092-1 and OP1092-2 collected from the top and the bottom of a single 2 m-high boulder in the debris flow levee have a comparable amount of accumulated ^{36}Cl (apparent ages of 12,900 and 8,700 yr, respectively), implying the

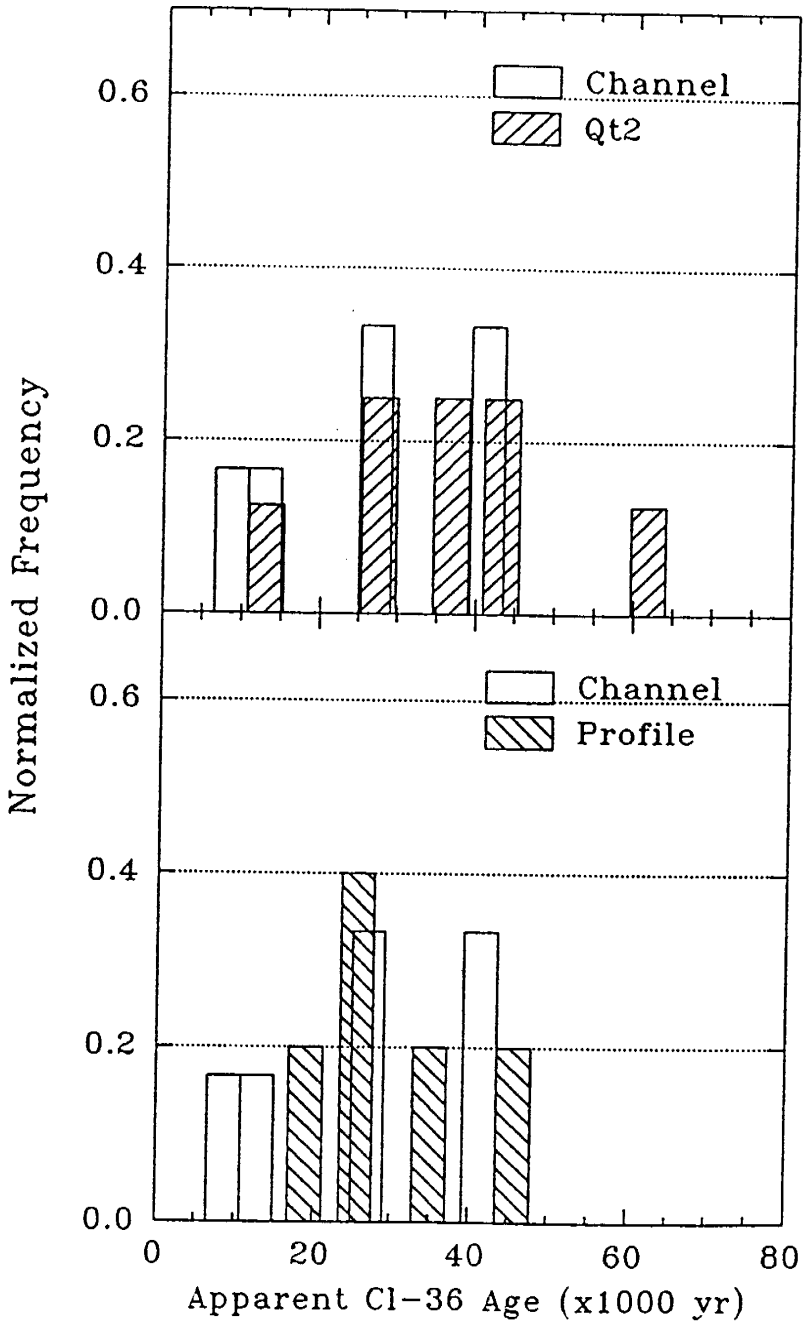

Figure 5.2 Comparison of ^{36}Cl ages. (a) between surface boulder samples on Qt2 (site #2, #5) and the channel (defined in Figure 5.1) and bedrock samples, and (b) between the cobble profile samples on Qt2 (site #2) and the channel and bedrock samples. The age distribution is expressed in normalized frequency.

boulder has rolled repeatedly and is gradually moving downslope. The bedrock sample also has significant ^{36}Cl buildup, probably implying steady weathering at the rock surface rather than episodic spalling of the rock. Application of the steady-state erosion Equation 3.24 to the bedrock sample OP-392-10 ($^{36}Cl/Cl = 550x10^{-15}$) yields an apparent erosion rate of 18 mm/1000 yr, assuming steady erosion for a very long period. The similarity of the apparent age of this sample (38,8000 yr) to the other debris flow and channel samples suggests that the erosion history of this bedrock sample is representative of the mountain front at this location. Combined with the similarity of the age distributions between Qt2 and the mountain front, this result indicates that the anomalous apparent ^{36}Cl age of the Qt2 terrace is best explained by slow steady-state erosion of the mountain front, although the second hypothesis of episodic erosion cannot be completely ruled out.

5.5.2. Implications of the ^{36}Cl Age Distributions

It is notable that ^{36}Cl ages for the fan surfaces overlap the younger surfaces, showing a cluster type of distribution in time. A distinct feature of the pattern is that clusters of ages in the distribution from the older surface are reflected in the younger surfaces. The ^{36}Cl ages for the oldest unit, Qf1 (ranging from 46,000 to 521,000 yr), show five age clusters. The youngest age at about 46,000 yr is matched by similar ages from all of the younger surfaces. Ages close to 100,000 yr are found in Qt1 and Qf2 as well as in Qf1. The 125,000 to 138,000 yr cluster is also found in Qf2. However, the 228,000 to 280,000 yr and 521,000 yr groupings are

unique to Qf1 because these are older than those from any other units. Overlapping of ^{36}Cl ages between the surfaces could be caused by (1) succession of old material from the adjacently dissected old surface, (2) later exposure of the buried material due to erosion, (3) addition of new material to older surface in later events, and (4) bioturbation of the top loose material in the soil profiles. The first case would introduce an older apparent ^{36}Cl age. This may affect the ^{36}Cl age distributions on the two young terraces, because they are situated topographically lower, set into the fan surfaces. The second case could cause an apparent age older or younger than the actual age depending upon the proportion of the spallogenic ^{36}Cl production rate and burial depth of the sample. The third case would cause younger apparent ages, and may be the cause of the age distributions of the two oldest surfaces, Qf1 and Qf2. The last case should give a mean age of the earth material within the effective depth of bioturbation. It is likely that the bioturbation only occurs in approximately top 30 cm of the soil profile, above the petrocalcic horizon on Qf1. The integrated cosmogenic ^{36}Cl accumulation in this depth interval should not differ significant from the ^{36}Cl accumulation in the surface samples because the opposing effect from spallation and thermal neutron activation, as we discussed in Chapter 3. Therefore, bioturbation can not explain the younger gravel ages from Qf1 and Qf2.

I hypothesize that alluvial surfaces may undergo multiple reworking without entirely losing the cosmogenic signature of earlier deposition events. This hypothesis is supported by a comparison of the ^{36}Cl buildup in gravel on the

surfaces with the boulder ages. Surface Qt2 has almost certainly experienced only a single episode of deposition and there the apparent exposure age of the gravel, 42,800 yr, is close to the mean exposure age of the boulders, 35,300 yr. In contrast, surface Qf2 has an apparent gravel age of 34,800 yr, which resembles the age of Qt2 but not the mean of the oldest boulders on Qf2 (132,000 yr). Similarly, the apparent gravel age on Qf1 is 78.100 yr, similar to the younger boulder age cluster on Qf2, but much younger than the oldest boulders on Qf1, which average 258,000 yr (excluding sample OP90-2, a single age of 521,000 yr). This pattern supports a model of repeated cycles of alluviation, reworking of high level surfaces, then incision and deposition of new units. During episodes of reworking the larger boulders will be most resistant to either removal or covering by alluviation (although new boulders may be carried in), whereas the surficial gravel is likely to be either eroded or covered by new alluvium. Thus the exposure age of the gravel will tend to reflect the most recent episode of reworking, but the age distribution of the boulders will be influenced by all of the episodes.

Based on this scenario, I believe that the oldest boulder age from Qf1 (521,000 yr) represents a single survivor from the initial deposition of Qf1. The first reworking episode is evidenced by the apparent ages of samples OP90-11, OP90-13 and OP90-5, which average 258,000 yr. The apparent ages in the next cluster, comprised of samples OP90-1, OP90-3, and OP91-6, average 132,000 yr, identical to the two oldest samples from Qf2. Finally, the two youngest samples from Qf1 average 72,700 yr, close to the apparent gravel age of 78,100 yr and also close to

the average of the two boulders from Qf2, 67,400 yr. The most recent episode of reworking is indicated by the grouping of apparent ages between 62,000 and 13,000 yr on Qt2, as well as similar apparent boulder and gravel ages on Qt1 and Qf2.

5.5.3. Effects of Inherited ^{36}Cl and Erosion

Due to the significant inherited ^{36}Cl in the samples on the young surfaces, it is difficult to assign numerical ages for the two terraces. However, assuming that the weathering and transport processes of the rocks from the mountain to the Qt2 surface discussed above is reasonably representative of the long-term Quaternary processes in the study area, it may be possible to estimate the effect of the inherited ^{36}Cl on the apparent ages of the surfaces. The inherited ^{36}Cl will proportionately have a smaller effect on the older surfaces than on the younger surfaces. On the other hand, the older surfaces might be eroded after the deposition of the surfaces, resulting in a reduced ^{36}Cl accumulation in the boulders once buried in the subsurface but now exposed on the surfaces due to erosion (Zreda et al, 1994). Below I am going to evaluate the effects of both inherited ^{36}Cl and erosion on the apparent ^{36}Cl age distributions.

For the case in which the ^{36}Cl built up due to previous exposure is larger than the analytical uncertainty while erosion is negligible, the minimum ^{36}Cl ages may be considered as the maximum ages of the surfaces. This criteria may be applied to the terraces in this area because they are well preserved, situated only one to two meters higher than the active channels, and the youngest terrace (Qt2) has

apparent ^{36}Cl ages similar to the boulder and gravel samples. Based on this, the maximum ^{36}Cl age of Qt2 may be 13,100 yr (sample OP90-7) and of Qt1 may be 33,500 yr (sample OP1092-5). The effect of the inherited ^{36}Cl may also be corrected by evaluating the apparent ^{36}Cl ages for the samples in the mountain front. To correct for the effect of inherited ^{36}Cl, I assume that the mean ^{36}Cl age of 26,400 yr for the debris flow, channel, and bedrock samples is representative of the average previous exposure time of the samples on the all studied surfaces. By subtracting the pre-exposure time, the corrected ages of the surfaces are obtained and given in Table 5.5. The corrected ages for the "pulses" of reworking and deposition are 9,000 ±10,000 yr (Qt2, Qt1, Qf2 and Qf1), 58,000 ±18,000 yr (Qt1, Qf2 and Qf1), 106,000 yr (Qf2 and Qf1), 232,000 yr (Qf1), and 495,000 yr (Qf1). These corrected mean ages may be considered to be the minimum ages of the surfaces, although the relative uncertainty is considerably larger for the two young terraces because the inherited ^{36}Cl is predominant in the samples from these two surfaces. The youngest boulder ages of 13,100 yr on Qt2 and of 33,500 yr on Qt1 are, respectively, comparable with the first two corrected pulse age ranges.

In order to calculate an upper bound for the effect of erosion on the ^{36}Cl accumulation in boulders that may have been once mantled by sediments on the two old surfaces, I assume that:

(1) There is no inherited ^{36}Cl in the samples. This will give a conservative estimate for the effect of erosion;

(2) The maximum erosion depth was 200 g cm^{-2} (approximately one meter soil

Table 5.5 Corrected ^{36}Cl Ages

Sample#	Unit	t (1)	t (2)	t (3)	Sample#	Unit	t(1)	t(2)
		10^3 yr					10^3 yr	
OP 90-2	Qf1	521	495	441	OP 90-7	Qt2	13.1	-13.3
OP 90-5	Qf1	267	241	339	OP 90-8	Qt2	26.6	0.2
OP 90-11	Qf1	280	254	351	OP 90-9	Qt2	35.3	8.9
OP 90-13	Qf1	228	202	285	OP 90-10	Qt2	43.7	17.3
OP 90-1	Qf1	125	98.6	150	OP 91-3	Qt2	38.2	11.8
OP 90-3	Qf1	138	112	195	OP 91-4	Qt2	28.5	2.1
OP 91-6	Qf1	133	107	180	OP 91-5	Qt2	61.9	35.5
OP 91-7	Qf1	99.8	73.4	151	BD 6cm	Qt2	45.7	19.3
OP 90-12	Qf1	45.6	19.2	55.7	BD 28cm	Qt2	26.9	0.5
CP#2 5cm	Qf1	78.1	51.0		BD 50cm	Qt2	19.0	- 7.4
OP 91-1	Qf2	134	108	196	BD 86cm	Qt2	35.0	8.6
OP 91-2	Qf2	130	104	167	BD 114cm	Qt2	24.4	- 2.0
OP 392-4	Qf2	85.1	58.7	127	S5 #1	Qt2	42.8	16.4
OP 1092-3	Qf2	49.8	23.4	71.2				
S3 #1	Qf2	34.8	8.4					
OP 392-2	Qt1	57.8	31.4					
OP 392-3	Qt1	100	73.6					
OP 1092-5	Qt1	33.5	7.1					

(1) uncorrected ^{36}Cl age

(2) corrected for inherited ^{36}Cl

(3) corrected for erosion

thickness), which is also conservative based on our observations that the top of the petrocalcic horizon occurs approximately 30 cm beneath the surface on Qf1;

(3) The soil erosion rate is 0.001 g cm^{-2} yr^{-1}, which is quite low for soil erosion. From this the burial time was 200,000 yr, obtained by dividing the burial depth by the erosion rate;

(4) There are two stages of cosmogenic ^{36}Cl accumulation history. In the first stage the boulders were mantled by soil until time t_1 (200,000 yr), after which the boulders were exposed on the surface. There has been no erosion of the boulders themselves during the period from t_1 to the present ($t - t_1$). The ^{36}Cl accumulation in the first stage can be estimated using Equation 3.23, and the total cosmogenic ^{36}Cl accumulation can be estimated by:

$$R_t = \frac{P_s(0) + P_n(0)}{\lambda_{36} N}\left[1 - e^{-\lambda_{36}(t-t_1)}\right] + R_1 e^{-\lambda_{36}(t-t_1)} \qquad 5.2$$

where R_t is the ratio of the total ^{36}Cl to stable Cl at time t, and R_1 is the ratio of the ^{36}Cl accumulation at time t_1 to stable Cl.

(5) If the ^{36}Cl accumulation estimated under the given minimum erosion rate and burial depth exceeds that actually measured in the samples, it means that either the erosion rate was too low or the burial depth was too large, resulting in excess ^{36}Cl. In this case, to match the actual ^{36}Cl data, the burial depth was kept at 200 g cm^{-2} while the erosion rate was adjusted so that the ^{36}Cl accumulation only has one stage, the first stage. This will give more conservative estimates due to the fact that the ^{36}Cl accumulation in rocks below the surface is more sensitive to the erosion rate than to the burial depth.

Given all the conditions above, the upper limit of the surface ages for Qf1 and Qf2 was calculated, and the corrected ages are given in Table 5.5. The mean erosion-corrected ages for Qf2 and Qf1 are 178,000 and 325,000 yr, respectively, and the corrected age for the oldest sample on Qf1 is 441,000, compared with the uncorrected apparent ages of 132,000, 258,000 and 521,000 yr.

Figure 5.3 shows the combined result, in which the lower and upper limits of the surface ages for Qf2 and Qf1 are determined by considering inherited ^{36}Cl and erosion, respectively, except for the oldest sample of Qf1. The lower limit of the age for the oldest sample is represented by the one estimated from the erosion correction rather than from the inherited ^{36}Cl correction because the effect of inherited ^{36}Cl is smaller than the effect of erosion for this sample. This sample has very high Cl concentration, thus thermal neutron activation of ^{35}Cl is the dominant contributor to the total ^{36}Cl production. As a result, the average ^{36}Cl production rate between the 200 g cm^{-2} depth and the land surface for this sample is higher than the production on the surface, and therefore the uncorrected age is always older than the corrected age. This was predicted by Liu et al. (1994a) and stated in the previous chapter (Chapter 3) based on the thermal neutron flux distribution in the shallow subsurface.

The actual scenarios could be much more complex than the situations we have discussed. For example, a boulder could experience cosmic-ray exposure while eroding from the mountain front, be transported to a fan surface and subsequently buried, be eroded out of the fan and be redeposited on a terrace where it

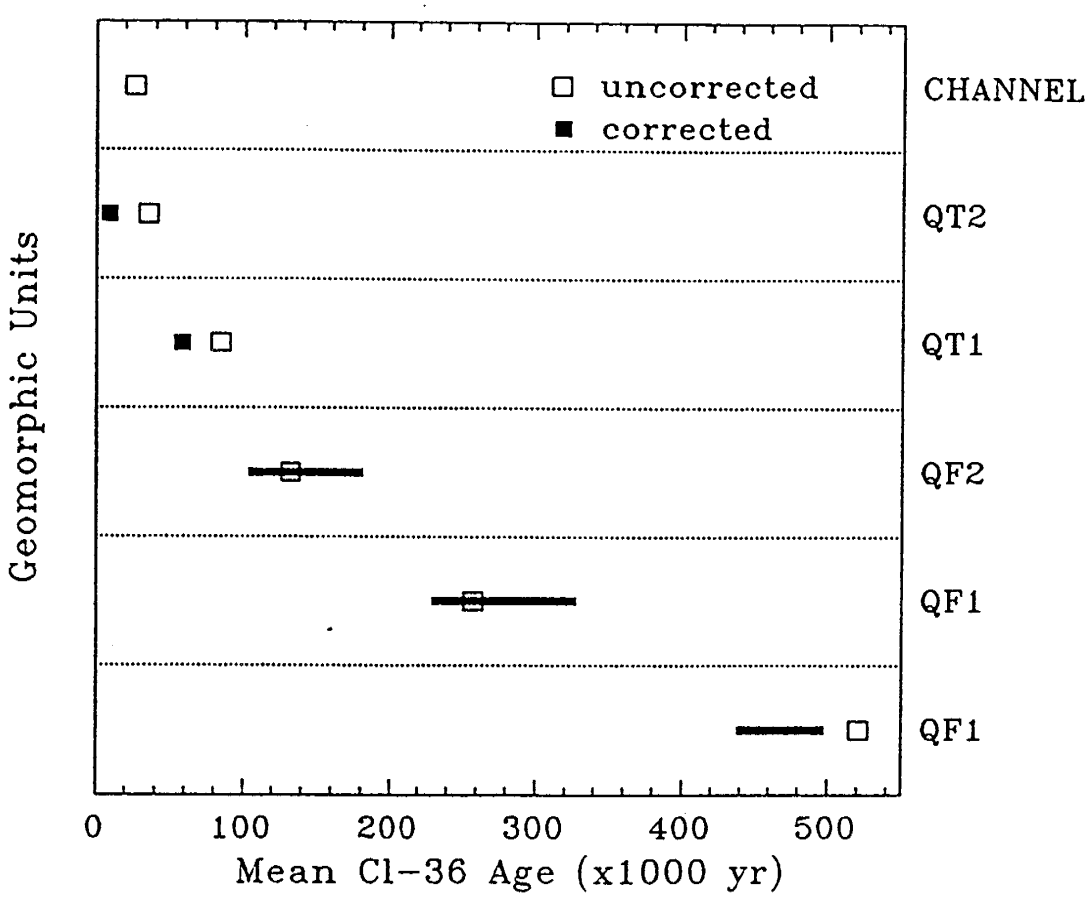

Figure 5.3 Corrected mean ^{36}Cl ages. The hollow squares represent individual mean ages of the five apparent ^{36}Cl age pulses, the filled squares the ages of the terraces corrected for inherited ^{36}Cl alone, and the black bars the age ranges given by correcting for inherited ^{36}Cl and erosion.

undergoes additional cosmic-ray exposure before being sampled. Furthermore, production rates could have varied during such a history due to redeposition at successively lower elevations. However, I believe that these factors will not significantly affect the picture drawn after accounting for the inherited ^{36}Cl and the erosion. The elevation effect on the production rate of ^{36}Cl is less than 7% even if all the ^{36}Cl in the boulders on the surfaces (elevation about 650 m) were accumulated at the position of the debris flow (elevation about 730 m). In spite of the fact that the analysis maximized the effects of inherited ^{36}Cl and/or erosion on the ^{36}Cl ages, the intervals of surface formation or reworking inferred from the corrected ^{36}Cl ages do not overlap. The preservation of age groups that can be correlated between surfaces and the lack of overlap between the groups lends confidence to the surface history inferred from the ^{36}Cl buildup ages.

5.4.4 Correlation between ^{36}Cl Ages and Paleoclimate

Climate change in Quaternary is an important driving force for forming and changing landforms and for geomorphic evolution. Dohrenwend (1987) indicated that geomorphic and sedimentologic processes in the Basin and Range are particularly sensitive to climatic change. Especially in desert areas low precipitation and sparse vegetation combine to produce a variety of climatically sensitive geomorphic and sedimentologic thresholds and a corresponding variety of climatically indicative landforms and sedimentary deposits. Based on vegetation assemblages in ^{14}C dated pack rat middens at 535 to 695 m in the Puerto Blanco

Mountains, approximately 15 km southwest of this study area, and in Alamo Canyon at 915 m elevation right within this study area, Van Devender (1987) has indentified a shift from a juniper-oak woodland to desertscrub at approximately 11,000 yr B.P. that marked the end of the late Wisconsin. He has also indicated that early Holocene climate was transitional between glacial and modern climates in the middle Holocene. Bull (1984) suggested that the change in climate that accurred during the transition from late Pleistocene to Holocene may have produced conditions favorable for debris flows. The ^{36}Cl ages from the surficial material on the four surfaces in this study area could reflect major glacial-interglacial transition and landform instability processes.

5.6. Conclusions

This study shows that cosmogenic ^{36}Cl can be useful for dating of Pleistocene geomorphic surfaces and for evaluating the geomorphic histories in piedmont settings. However, the age uncertainty can be profound for young surfaces if erosion rates are slow or older alluvial units are eroded to form young ones, causing inherited cosmogenic ^{36}Cl to be significant.

The morphostratigraphic sequence determined by the cosmogenic ^{36}Cl ages of the boulders exposed on the surfaces in the study area is consistent with that determined from soil development by Simpson (1991). The oldest preserved alluvial fan surface apparently initially stabilized about 440,000 yr ago. It

experienced major reworking between 232,000 and 325,000 yr ago. Between178,000 and 106,000 yr ago Qf1 was reworked again, and Qf2 was deposited. Both alluvial fan surfaces were reworked again between 33,000 and 59,000 yr ago, followed by incision and deposition of the older terrace (Qt1) as backfill in the incised channels. Finally, Qt1 was reworked, the channels were incised again and the younger terrace (Qt2) was deposited as shallow fill in the channel bottoms between 13,000 yr ago and present, but most probably in the mid to late Holocene. The ^{36}Cl data from bare bedrock on the mountain front and alluvial clasts proximal to the source area indicate slow (considering the steep topography) denudation rates, probably close to 20 mm/1000 yr. This slow rate of mountain-front retreat (only about 30 m over the entire Quaternary), may help to explain the extensive preservation of old alluvial surfaces on the piedmont below the mountains.

6. ^{36}Cl IN PETROCALCIC HORIZON

6.1. Introduction

Pedogenic carbonate commonly accumulates in noncalcareous parent soils in semiarid to arid regions. The morphological features and carbonate content in the carbonate-rich (Bk or K) horizon have been used as an age index for landforms (Gile et al., 1966, Machette, 1985). However, many variables affect the development of pedogenic carbonate, including soil texture, local climate, hydrological conditions, eolian flux (which is believed to be the major source of Ca, e.g., Gile et al., 1981), and production of CO_2 by biomass in the soil profile. Consequently, the surface age estimates based on the degree of pedogenic carbonate development are subject large uncertainties. Although the age of the surficial material is often inferred to be the same as that of the pedogenic carbonate, the ages for the two may be different if the geomorphic surface has been reworked. The ability to measure surface and carbonate ages separately and directly would thus be highly advantageous. In this way, geomorphic histories could be more accurately evaluated through comparing the age estimates for the surficial material and underlying carbonate horizon.

Cosmogenic ^{36}Cl in terrestrial surficial material is primarily produced by spallation of ^{39}K and ^{40}Ca and by neutron capture of ^{35}Cl (Phillips et al., 1986). ^{36}Cl accumulation in surficial rocks is a function of rock exposure time to cosmic

radiation, rock chemical composition, and the intensity of cosmic radiation, which depends on geomagnetic latitude, altitude, and mass shielding depth (Lal and Peters, 1967). The production of spallogenic nuclides in the subsurface decreases exponentially with increasing depth beneath the surface (Kurz., 1986). ^{36}Cl produced by thermal neutron capture increases with depth and reaches a maximum at approximately 20 cm before decreasing exponentially with depth (Yamashita et al., 1966, O'Brien et al., 1978, Liu et al., 1994a). The difficulty in quantifying the depth distribution of cosmogenic ^{36}Cl produced by thermal neutron capture has limited the application of the method to subsurface material. Recently, a simplified analytical solution for the thermal neutron distribution in the subsurface has been developed by Liu et al. (1994a). This model allows quantification of cosmogenic ^{36}Cl in the shallow subsurface and thus should permit direct determination of soil carbonate ages.

This study is the first attempt to directly date soil carbonate by means of cosmogenic ^{36}Cl. I present the measurements of ^{36}Cl accumulated in carbonate, silicate and pore water components from a soil profile and calculate ^{36}Cl ages for the individual components based on the model of Liu et al. (1994a). I also compare the ^{36}Cl ages from these components with the distribution of ^{36}Cl ages from boulders exposed on the surface. Finally, we discuss the geomorphic implication of the ^{36}Cl age distributions.

6.2. Sample Collection and Preparation

Nine samples were collected from an approximately 120 cm depth profile at sampling site #6 on Qf1 in Figure 4.3. The depth profile is shown in Figure 6.1. The samples were separated into bulk, silicate, carbonate and pore water components. The separation procedure was as follows: (1) bulk samples were crushed to small fragments, then weighed before and after drying in an oven to obtain the water content; (2) the crushed sample was thoroughly leached in deionized water to extract the leachable Cl in the pore water; (3) the leached sample was dried in an oven, then dissolved in nitric acid to obtain the Cl in the carbonate component; (4) the silicate component (the nitric-acid insoluble residue) was washed in deionized water until it was neutralized, then dissolved in hydrofluoric acid to extract the Cl from the silicate residual. I processed six silicate, four carbonate and seven pore water samples from the nine bulk samples for ^{36}Cl measurement. Preparation and extraction of Cl from the silicate residual samples for $^{36}Cl/Cl$ ratio analysis followed the procedure described in Zreda (1994). For the other two components, excess $AgNO_3$ was simply added to the solutions to precipitate AgCl for accelerator mass spectrometry analysis. The AgCl was concentrated by evaporation at 50 °C. The stable Cl concentrations were measured for bulk samples, pore water and silicate residual by ion selective electrode. The Cl concentrations in the carbonate fraction were calculated based on mass balance. The detailed procedure is described in Appendix 4.

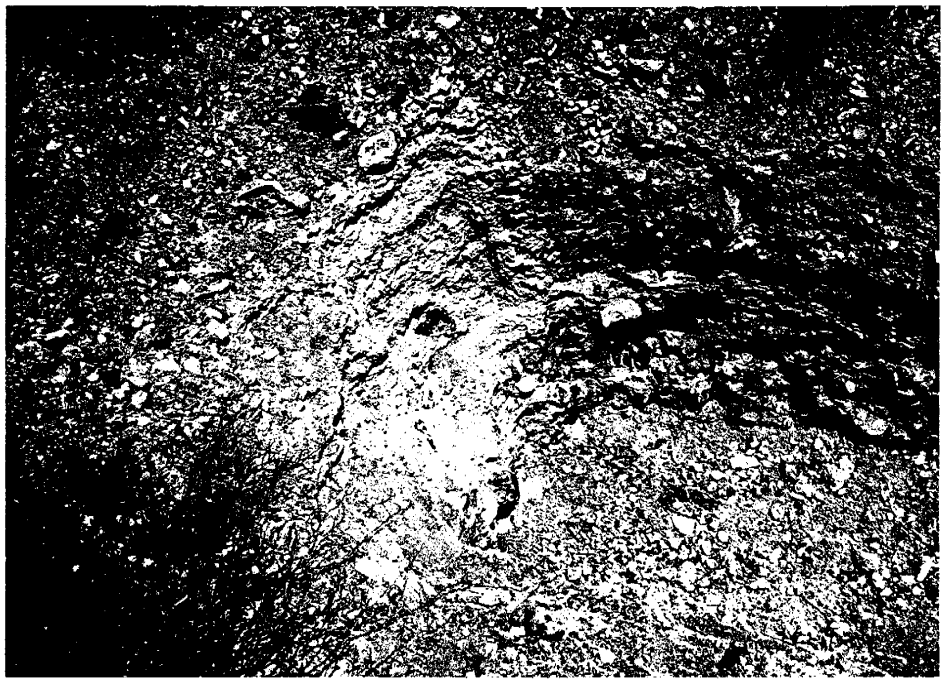

Figure 6.1 Petrocalcic horizon on Qf1. The depth of the soil pit is 1.5 m.

6.3. Results and Discussions

Table 6.1 presents the carbonate content, Cl concentrations and $^{36}Cl/Cl$ ratios in the different components as a function of depth. The $^{36}Cl/Cl$ ratios in the pore water of the calcrete are 30% to 60% lower than that in the modern meteoric water in this area ($400x10^{-15}$), except for the deepest sample, which we believe to have been contaminated by ponding of rain water in the soil pit. The ratios (excluding the bottom one) decrease with increasing depth (Figure 6.2) and indicate two straight-line segments that intersect at a depth of 60 cm. This suggests that the pore water is very old and has not been redistributed during the history of the calcrete horizon.

The residence time of the pore water was calculated based on both ^{36}Cl decay from an initial $^{36}Cl/Cl$ ratio of $400x10^{-15}$ in the soil water and ^{36}Cl production due to thermal neutron capture of ^{35}Cl in the pore water using the following equation:

$$t = -\frac{1}{\lambda_{36}} \ln \left[\frac{\lambda_{36} NR - P_n(Z)}{\lambda_{36} NR_0 - P_n(Z)} \right] \qquad 6.1$$

where R_o is the initial $^{36}Cl/Cl$ ratio in the soil water ($400x10^{-15}$), and $P_n(Z)$ is determined by Equation 3.16 for the ^{36}Cl production rate due to thermal neutron activation of ^{35}Cl in the pore water of the petrocalcic horizon. The ^{36}Cl production due to spallation of ^{39}K and ^{40}Ca was assumed negligible for the pore water.

The ^{36}Cl ages for the carbonate and silicate residual components have also been calculated using depth-dependent equations 3.15 and 3.16 for ^{36}Cl production.

Table 6.1 $CaCO_3$, Cl and $^{36}Cl/Cl$ Ratios in Different Components

Sample	Depth	Water	Carbonate	Cl(B)	Cl(R)	Cl(L)	Cl(C)	$^{36}Cl/Cl(R)$	$^{36}Cl/Cl(L)$	$^{36}Cl/Cl(C)$
	(cm)	(wt%)	(%)	---------- (mg/kg) ----------				---------- (10^{-15}) ----------		
0-4	5	3.0	4	49.3	41.4			1090 ±110		
8-10	23	7.8	8	196	32.9	164		777 ± 81		
12-16	36	2.5	38	660	48.8	546	220	1610 ± 60	265 ±14	1790 ±370
17-19	46	1.3	39	130	38.8	87.3			240 ±24	
21-24	57	1.3	37	547	38.5	461			175 ±15	
25-28	67	1.6	37	1410	57.8	1223	407	1320 ± 50	156 ± 9.4	913 ± 67
31-34	83	2.0	46	640	45.8	590			140 ±12	
35-38	93	1.7	60	941	41.4	829	159	925 ± 44	128 ± 8	1780 ±100
47-51	124	7.0	21	96.9	47.1	47.9	59.4	1150 ± 50	348 ±25	1150 ± 70

(B): Bulk sample; (R): Silicate residual, (L): Pore water, (C): Carbonate. Cl concentration is in mg/(kg dry sample).

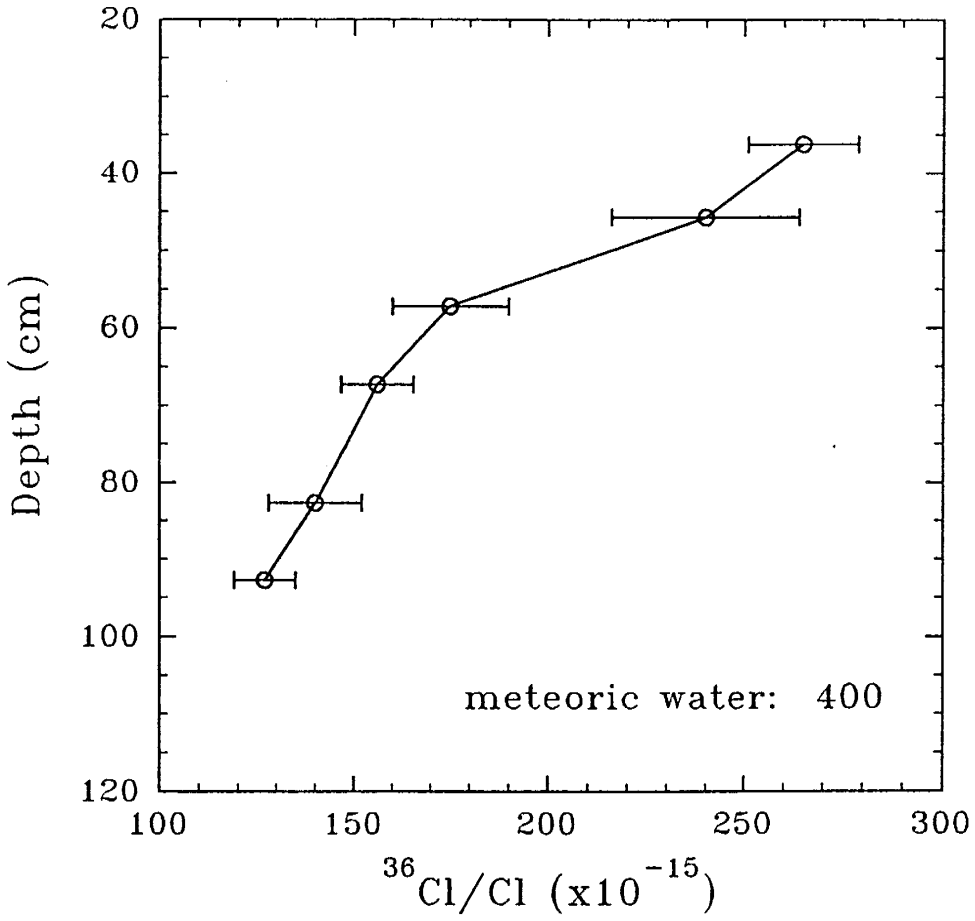

Figure 6.2 ^{36}Cl in pore water of petrocalcic horizon.

The ages for the pore water, carbonate and silicate residual generally increase with increasing depth (see Figure 6.2), ranging from approximately 70 ky for silicate near the surface to 560 ky for carbonate and 540 ky for pore water at 93 cm deep and to 695 ky for silicate at 124 cm deep. The ages of the silicate fraction between 36 and 93 cm appear anomalously young compared to the carbonate ages at the same depths. This may be because the repeated agressive leachings removed Cl from the silicate minerals. The Cl content of sample 0-4 from 5 cm depth, which contains only 4% carbonate, decreased by approximately 20% after the repeated leachings (see Table 6.1). Removal of Cl will cause anomalously young apparent ages.

The ages of all the three components in the calcrete horizon (between 36 and 124 cm) range from 200 to 700 ky. The result is summarized in Table 6.2, while Table 6.3 gives the relevant parameters for the above calculations. The ^{36}Cl age profiles for the different components are also plotted in Figure 6.3.

Since Cl is very mobile, the systematic gradient of pore water ^{36}Cl with depth suggests that the carbonate has not been redistributed by dissolution and reprecipitation. The agreement of the ^{36}Cl ages of the pore water samples in the calcrete horizon with the carbonate and silicate ages imply that the calcrete has been stable and virtually impermeable for the past 200 to 600 ky. The increasing ages of the carbonate and pore water with depth support the model of Gile et al (1966) that the calcrete horizon originates at depth and develops upward. The chemical compositions of the bulk samples and silicate residuals are given in

Table 6.2 ^{36}Cl Ages for Different Components in Petrocalcic Horizon

Sample	Depth (cm)	Density (g/cm^3)	Pore Water[1]	Pore Water[2]	Silicate	Carbonate
			----------	----------	(10^3 yr)	----------
0-4	5	1.8			78.1 +8.7/-8.5	
8-10	23	2.0			67.6 +7.7/-7.6	
12-16	36	2.3	179 +24/-22	209 +29/-27	179 +8/-8	304 +102/-83
17-19	46	2.3	222 +46/-41	240 +51/-46		
21-24	57	2.3	359 +39/-35	386 +44/-40		
25-28	67	2.3	409 +27/-25	445 +31/-29	313 +18/-17	425 + 56/-50
31-34	83	2.3	456 +39/-35	504 +47/-42		
35-38	93	2.3	499 +28/-27	541 +33/-31	288 +20/-19	557 + 69/-59
47-51	124	2.3	61 +32/-30	65 +36/-34	694 +82/-69	188 + 15/-14

1: considered for decay only; 2: considered for both decay and production.

Table 6.3 Relevant Parameters For ^{36}Cl Age Calculation

Sample	$\Sigma\sigma_i N_i$	L	$p(E_{th})$	$\sigma_{35}N_{35}(R)$	$\sigma_{35}N_{35}(L)$	$\sigma_{35}N_{35}(C)$	$K_2O(R)$	$CaO(R)$
	(cm^2/kg)	(g/cm^2)		---------- (cm^2/kg) ----------			-------- (%) --------	
0 -4	7.01	19.0	0.94	0.0220			3.78	1.16
8 -10	8.27	14.3	0.97	0.0168			2.60	0.87
12-16	5.52	21.1	0.95	0.0168	0.3029	0.0464	4.56	1.02
17-19	4.97	23.6	0.92		0.0484			
21-24	5.67	22.3	0.92		0.2557			
25-28	5.63	21.9	0.92	0.0202	0.6784	0.0835	4.01	1.22
31-34	5.33	21.9	0.94		0.3273			
35-38	4.71	23.3	0.94	0.0092	0.4598	0.0529	3.20	1.49
47-51	6.55	16.3	0.97	0.0206	0.0532	0.0069	4.08	1.25

Assuming the average atomic weight (A) to be 24 g/mole.

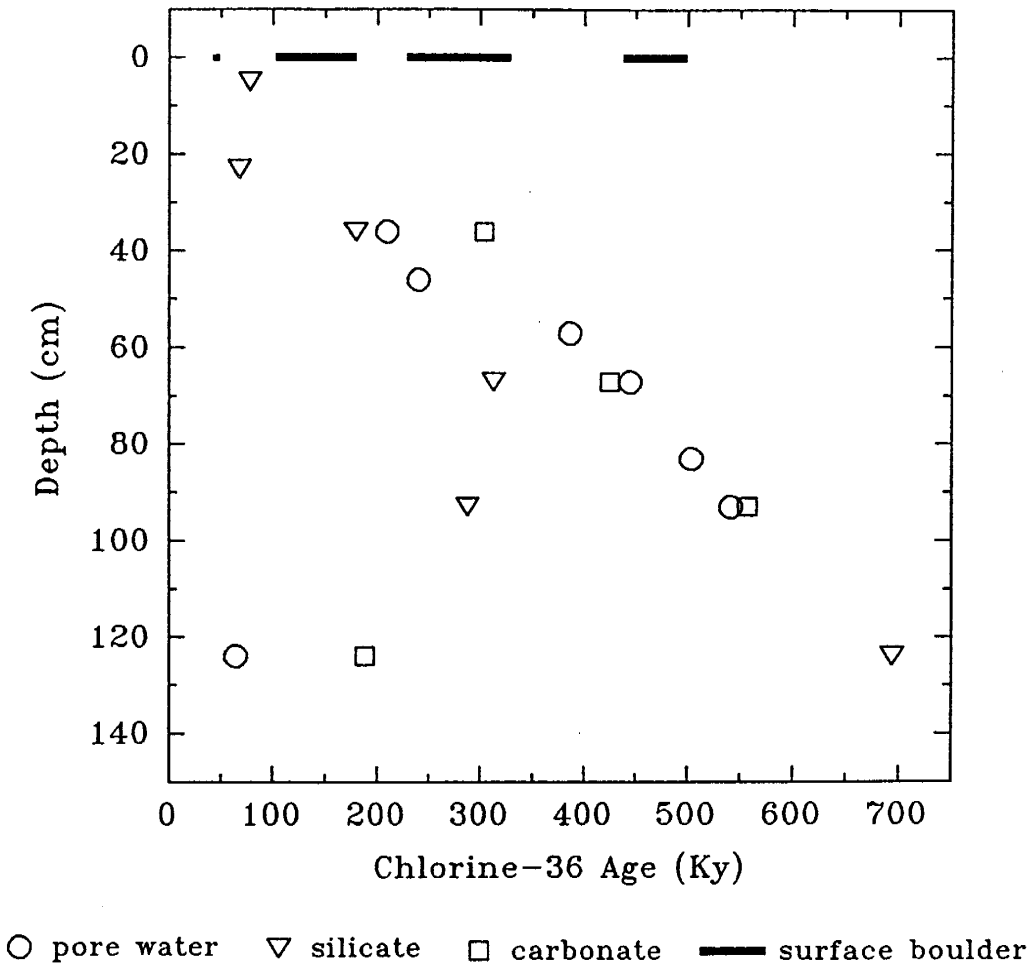

Figure 6.3 ^{36}Cl age distribution in petrocalcic horizon.

Appendix 5.

^{36}Cl ages of boulders from this surface show a clustered type of distribution in time, with age clusters at approximately 500 to 430 ky, 330-230 ky, 175-100 ky, and one sample at approximately 50 ky (see previous chapter, and Liu et al., 1994b). This was interpreted as a result of multiple surface reworking. The age of 550 ky for the calcrete horizon at 93 cm deep, where the carbonate content is about 60%, may indicate the time when accumulation of the calcrete horizon was initiated. This age is close to the oldest surface boulder age. The age of 386 ky for the pore water at 57 cm, the interception of the two straight-line segments in the depth profile of the pore water, may represent the time that an additional calcrete layer was added to the previous horizon. The ages ranging from 300 ky to 200 ky at the top of the calcrete horizon (36 cm), may date the termination of the carbonate accumulation that formed the main body of the calcrete horizon. This age is correlative with the second oldest age cluster of the surface boulder ages on this surface. The ^{36}Cl ages from the silicate samples above the calcrete horizon are close to the youngest surface boulder age but much younger than the ages from the calcrete horizon. It seems likely that the top soil above the calcrete horizon was deposited during the last episode of surface reworking and that the calcrete horizon was little modified by this event. The age of 694 ky for the silicate residual at the bottom of the calcrete horizon (124 cm), which only has about 20% carbonate content compared with 37% or higher carbonate content for the other calcrete samples, is older than the oldest age obtained from the surface boulders. This

probably reflects the timing of the initial deposition of the alluvial fan. We believe that the much younger ^{36}Cl ages for the pore water and carbonate for this sample are caused by contamination from rain water ponded in the bottom of the soil pit.

When combined with evidence from the surface boulder ^{36}Cl age distribution, the increasing age with depth through the calcrete horizon is best explained by long-term carbonate accumulation and aggregation alternating with episodic reworking. An average accumulation rate of 1.6 mm/ky was obtained from the slope of depth versus ^{36}Cl age in Figure 6.3, excluding the silicate age for the sample from 93 cm and the ages of the pore water and carbonate for the sample from 124 cm. The consistency between the age distributions for the surface boulders and for the calcrete horizon indicates that soil carbonate can successfully be dated using cosmogenic ^{36}Cl.

In general, the ^{36}Cl ages for the three components: pore water, carbonate and silicate residual, show similar trends although there are some discrepancies among them. Uncertainty in the bulk density of the calcrete horizon may be the main contributor to the discrepancy. The ^{36}Cl age calculations for the carbonate and silicate fractions are much more sensitive to the bulk density of porous medium than is that for the pore water, and the sensitivity increases with increasing depth. This is because ^{36}Cl in the carbonate and silicate are almost entirely derived from cosmogenic production, which depends strongly on mass shielding, while ^{36}Cl in the pore water is predominantly derived from initial meteoric water for which the ^{36}Cl concentration is depth-independent. A secondary contributor to the age

discrepancies is the assumption that the initial $^{36}Cl/Cl$ ratio in the pore water was $400x10^{-15}$, the same as that for the modern meteoric water. This value could have varied over time due to changes in geomagnetic field. Variation of geomagnetic field would have much less effect on the estimated ^{36}Cl ages for the silicate and carbonate fractions because their ^{36}Cl production rate has integrated the effect of geomagnetic variation over time. Finally, variation in the burial depth of the calcrete horizon over time may also introduce additional errors in the age estimates.

6.4. Conclusions

Cosmogenic ^{36}Cl ages from pore water, carbonate and silicate clasts in the top soil and calcrete horizon of a mid-Pleistocene soil from southern Arizona are consistent with both the degree of soil development and ^{36}Cl age distribution for boulder samples from the same surface. The ^{36}Cl ages obtained from the surface boulders and the calcrete horizon suggest that the surface initially stabilized 700 to 500 ky ago, followed by a long period of carbonate accumulation between 600 and 400 ky ago. Subsequently, the surface has been reworked several times and at least one additional carbonate layer added between 400 and 200 ky ago. The original loose soil above the calcrete horizon was stripped off during surface reworking, and the present top soil was probably deposited during the last episode of reworking. The results of this study indicate that cosmogenic ^{36}Cl holds promise for the dating

of soil carbonate in desert areas. Cosmogenic ^{36}Cl in the pore water of calcrete horizon can provide an independent check on the mobility of soluble constituents within the calcrete.

7. SOIL WATER MOVEMENT

7.1. Introduction

In desert areas the top meter of the soil profile is the hydrologically most active region. Soil water and solutes are strongly influenced by environmental changes such as temperature and precipitation. This region is also the critical zone for soil formation processes, such as secondary carbonate accumulation, translocation of clays through the soil, and chemical weathering reactions. With development of the soil profile, the soil structure will change (Birkeland, 1984) and the movement of soil water and solute movement will hence be altered (Gile et al., 1981). Low precipitation and high evapotranspiration in the desert areas may result in cyclic movement of the soil water in both liquid and vapor phases, in the top meter of the soil in response to the seasonal variations. That is, liquid soil water moves downward in the rainy season and upward in the dry season while water vapor moves downward below the evaporation front in response to the downward thermal gradient in the summer (Knowlton, 1990). Understanding the influence of soil development on soil water movement is important for water resource management and for analyzing pollutant transport in the vadose zone. The impact of seasonal variations in the top meter of soil on the deep soil profile is poorly understood, and few studies have evaluated the effect of soil development on soil water movement in desert environments.

Chemically-based natural tracers can provide powerful tools to examine in detail water and solute movement in the desert soils. Chloride is hydrologically very mobile and chemically inert, and is a nearly ideal natural tracer for the study of soil water movement in the liquid phase and for estimation of long-term average infiltration rates (e.g., Stone, 1984; Sharma and Hughes, 1985; Cook et al., 1992). One isotope of chlorine, ^{36}Cl ($t_{1/2}$ $3.01x10^5$), was anthropogenically injected into the atmosphere by atmospheric nuclear weapon tests of the early 1950s to early 1960s. This produced a useful isotopic pulse for investigating water movement and long-term average infiltration rates in the vadose zone simply by identifying the bomb-^{36}Cl peak (e.g., Phillips et al., 1988; Scanlon, 1992). Stable ^{18}O and ^{2}H as part of the water molecule can also be used to estimate recharge and evaporation (Saxena and Dressie, 1984; Allison and Barnes, 1983) and as a tracer of water vapor transport soils (Barnes et al., 1989; Knowlton, 1990). In addition, the oxygen and hydrogen isotopic composition of soil water partially reflects the isotopic composition of precipitation, which is correlated with the mean annual temperature (Dansgaard, 1964). Thus, ^{18}O and ^{2}H patterns stored in the vadose zone may provide paleoclimate information (Cook et al., 1992).

One of objectives in this study was to apply the environmental tracers ^{2}H, ^{18}O, Cl, and bomb-^{36}Cl to investigate infiltration and evaporation in the top meter of desert soils through the seasonal cycle and on age surfaces. Based on this I have attempted to evaluate the influence of the seasonal variations and soil development in the top meter soil profile on the deeper vadose zone.

7.2. Material and Methods

7.2.1. Sample Collection

Six soil profiles were collected from the top meter of soil on the youngest surface, Qt2 (site #5, #9), in January and May of 1991, and March, May, August and October of 1992. Ten to twelve samples were taken from each soil profile at equal depth intervals or at shorter depth intervals above 10 cm and larger depth intervals below that. Additionally, one soil profile on Qt1 (site #2) and one soil profile on Qf2 (site #10) were also collected from the top meter in October and March of 1992, respectively. Figure 7.1 shows the photographs of the sampled soil profiles.

The soil textures at the sampling locations on Qt2 and Qt1 generally are gravelly to very gravelly sandy loam. The soil development on Qt2 is very weak with Stage I carbonate morphology of Gile et al. (1966). Carbonate accumulation is found from approximately 30 cm below the surface until about 100 cm. Qt1 has more advanced soil development than Qt2. The soil profile at the sampling location on Qf2 contains a strong argillic horizon between 40 and 70 cm depth overlain by an approximately 20 cm thick Bk horizon with Stage I carbonate morphology of Gile et al. (1966). The soil texture at this site is gravelly to very gravelly clay loam. To minimize effects of water suction or Cl uptake by plant roots, the sampling locations were chosen within areas relatively bare of vegetation. The soil samples were stored in glass jars and sealed with silicon grease

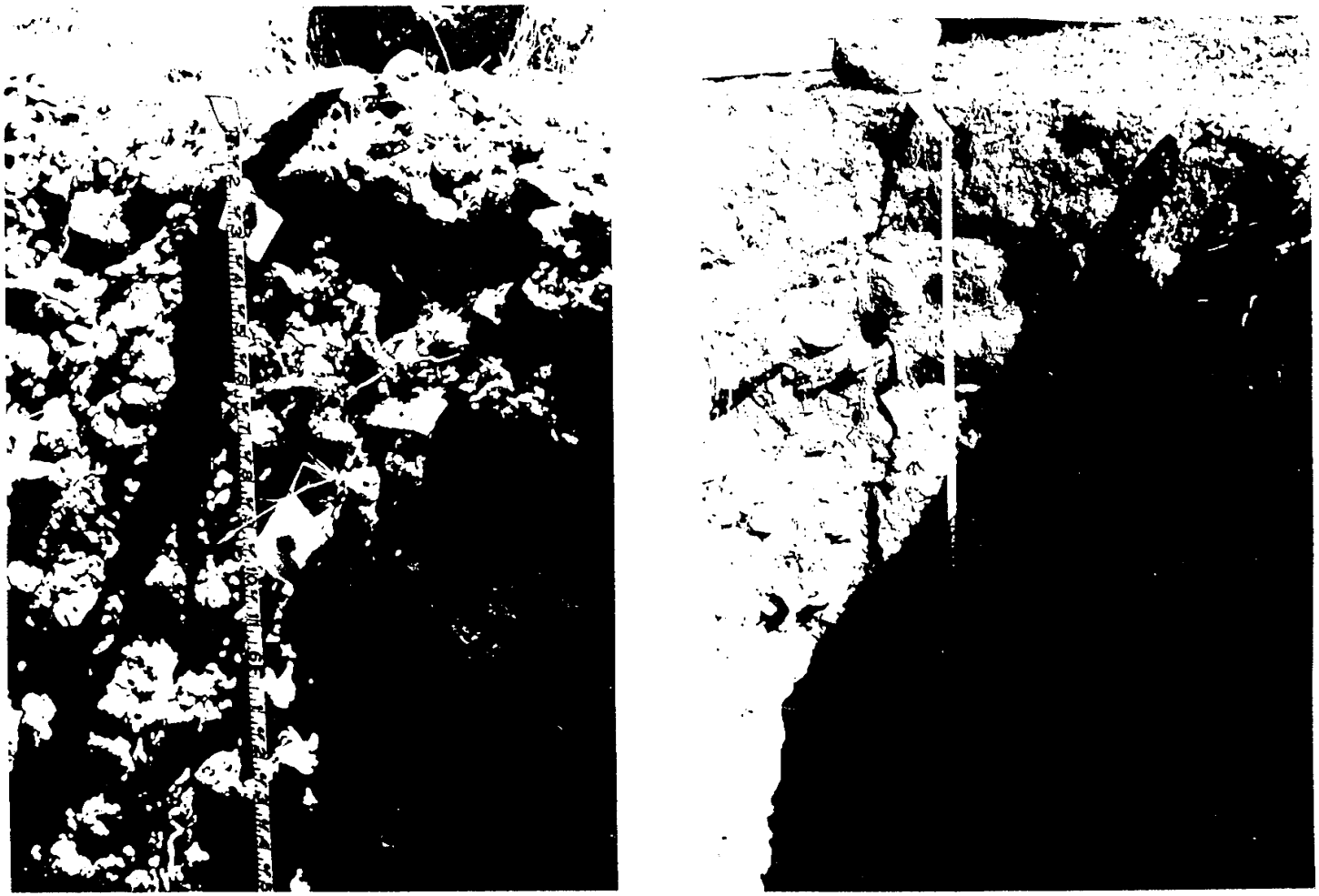

Figure 7.1 Photographs for sampled soil profiles. The left photo is for a soil pit on Qt2 and the right one is for a soil pit on Qf2.

immediately after sampling to prevent isotopic fractionation by evaporation or atmospheric contamination.

7.2.2. Sample Preparation and Analysis

Soil water for ^{18}O and ^{2}H analyses was extracted from the sampled soils using a vacuum distillation method developed and tested by Knowlton et al. (1989). The bulk gravimetric water content of the soil samples was determined by weighing soils before and after the distillation. CO_2-H_2O equilibration (Socki et al., 1993) and Zn reduction (Coleman et al., 1982; Kendall and Coplen, 1985) methods were used to produce CO_2 and H_2 gaseous phases for mass spectrometric analyses of the oxygen and hydrogen isotopic compositions, respectively. The stable isotopic compositions were measured on a Finnigan-Mat (Delta-E) gas source mass spectrometer and are expressed as δ-values in parts per mil relative to the international standard, V-SMOW. All the stable isotope measurements were conducted in the Stable Isotope Laboratory of the Geoscience Department, New Mexico Tech. Stable chloride concentrations in the soil water were measured by ion chromatography and ion selective electrode. One ^{36}Cl profile was measured for the soil profile from Qt2 sampled in January of 1991 (site #5). The procedure for the soil ^{36}Cl sample preparation was similar to that described in Mattick et al. (1987). The water content for the soil matrix (less than 2 mm) was measured by gravimetric analysis before and after oven drying.

7.2.3. Method for Estimation of Evaporation Rate

Evaporation from a bare soil surface proceeds in two stages. During the first stage, from wet soil which meets the evaporative demand, the evaporation rate is constant under isothermal conditions (Hillel, 1971). After the first stage, as the soil surface begins to dry, the evaporation rate falls quickly to reach a quasi steady-state (Barnes and Allison, 1988), the second evaporation stage. For the second evaporation stage, at steady-state, the evaporation rate (E) from the evaporation front may be estimated using Fick's law (e.g., Allison and Barnes, 1983, Knowlton, 1990):

$$E = D_{v*} \frac{\partial (h N_s)}{\partial Z} = D_v \tau (n - \theta) N_s \frac{h_{ef} - h_a}{\rho Z_{ef}} \qquad 7.1$$

where D_{v*} and D_v are the diffusivities of water vapor in the porous medium and air, respectively, τ is tortuosity, n is soil porosity, θ is volumetric soil water content, h is relative humidity, N_s is saturated water vapor density as a function of temperature, ρ is the density of water, Z is depth, and subscripts, ef and a, represent the evaporation front and the free air, respectively.

7.2.4. Methods for Estimation of Downward Water Flux

A mass balance on chloride is a simple and useful testing for estimation of long-term average downward water flux in desert areas (e.g., Stone, 1984;, Sharma and Hughes, 1985; Mattick et al., 1987). If it can be assumed that water and Cl move by piston flow, that the Cl deposition from the atmosphere has been

relatively constant, that atmospheric fallout (in precipitation and dry deposition) is the sole source of chloride, and that Cl uptake by plants is negligible, an average downward water flux (I) can be calculated:

$$PC_o = IC_s \qquad 7.2$$

where P is mean annual precipitation, and C_o and C_s are the mean chloride concentrations in precipitation and soil water, respectively.

A plot of cumulative Cl against cumulative water may show several straight-line segments with different slopes, each of which represents the Cl concentration in the soil water in the corresponding depth interval of the segment (Stone, 1984). By evaluating individual straight-line segments separately, one may estimates infiltration rates in the different sections of a soil profile.

The chloride mass balance method also can be used for estimating soil Cl accumulation age at a given depth of a soil profile (e.g., Stone, 1984):

$$t(z) = \frac{\Sigma Cl(z)}{PC_o} = \frac{\sum_i \rho_i Cl_i z_i}{PC_o} \qquad 7.3$$

where t(z) is the Cl accumulation time at depth z, ΣCl(z) the cumulative soil Cl at depth z, Cl_i the Cl concentration of the dry soil in depth interval z_i, and ρ_i the dry soil bulk density for depth interval z_i.

If the bomb ^{36}Cl peak can be located in the soil profile its position can be used together with water content data for estimating the average infiltration rate (e.g., Phillips et al., 1988), assuming piston flow of the soil water and solutes.

7.3. Results

The soil water content for the six soil profiles collected during different seasons on Qt2 is shown in Figure 7.2, in which the monthly precipitation during the sampling period is also presented. The soil water content varies from 15 wt% down to 1 wt%, showing a strong correlation with antecedent precipitation. The Cl concentrations in the soil water for all the profiles from Qt2, except for May of 1991, are plotted with depth in Figure 7.3. The Cl concentrations range from 5 to 224 ppm, but most of them fall in the range 5 to 50 ppm. The Cl profiles for different seasons generally show a similar trend of increasing Cl concentration of soil water with increasing depth (see Figure 7.3). Figure 7.4 shows the seasonal δ^2H and $\delta^{18}O$ profiles in Qt2. All of the soil water, Cl concentration and stable isotope data display cyclic changes through the seasons. I will discuss them on a seasonal basis.

Figure 7.5a and 7.5b show, respectively, the soil water content and Cl concentration depth profiles for the older surfaces of Qt1 and Qf2. The soil water content of Qf2 in March 1992 varies from 5 to 15 wt%, and of Qt1 in October 1992 ranges between 1 and 5 wt%. The Cl concentrations in the soil water range from 170 to 7300 mg/l for Qt1, and 25 to 8800 mg/l for Qf2, much higher than those from the youngest surface, Qt2. The general trend of the Cl depth profiles is similar to those for Qt2, namely, the Cl concentration almost monotonously increases with increasing depth. Figure 7.6 shows the H and O isotope profiles for

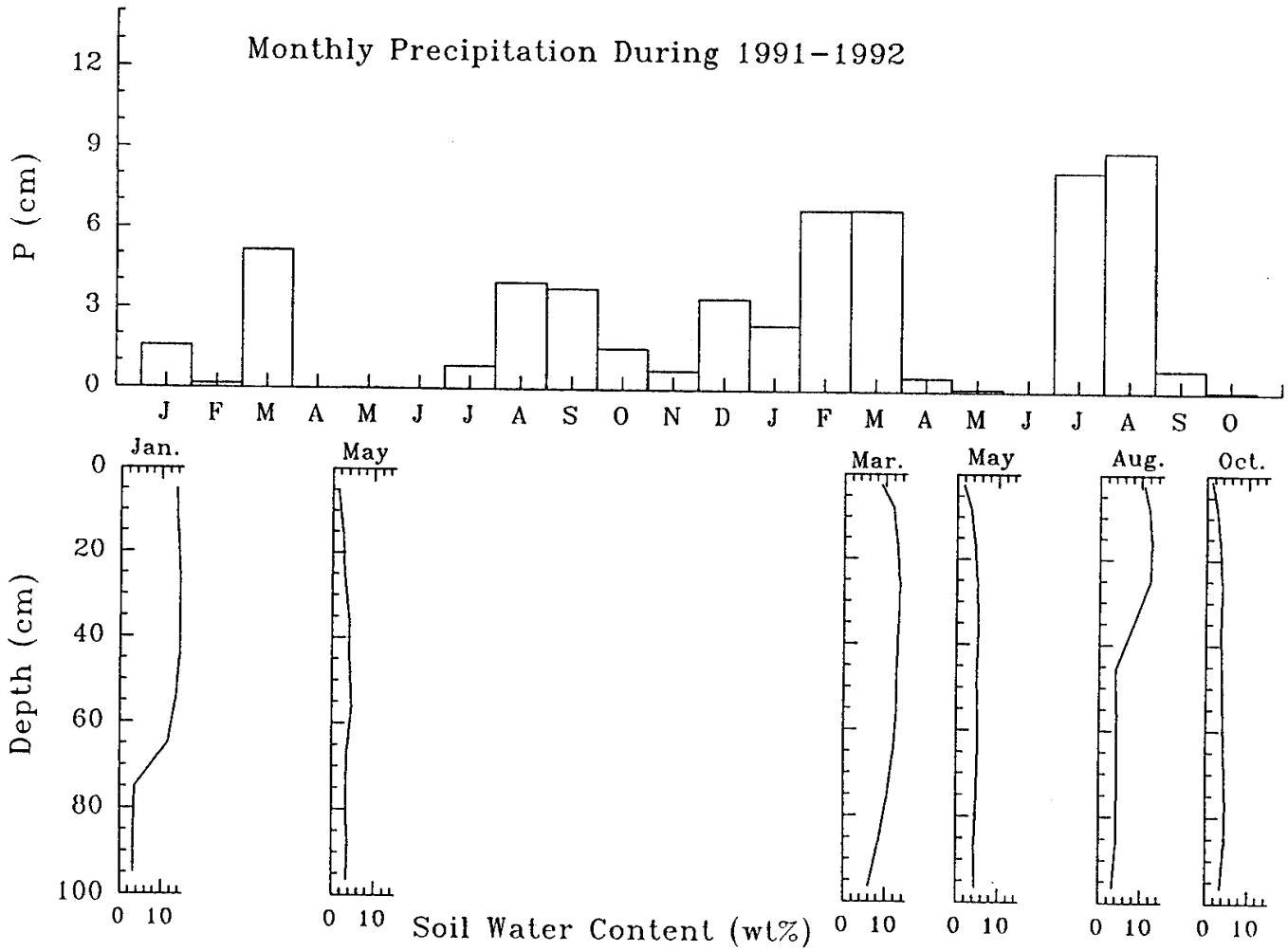

Figure 7.2 Soil water contents from Qt2. The monthly precipitation during the corresponding period (1991-1992) is also plotted for comparison.

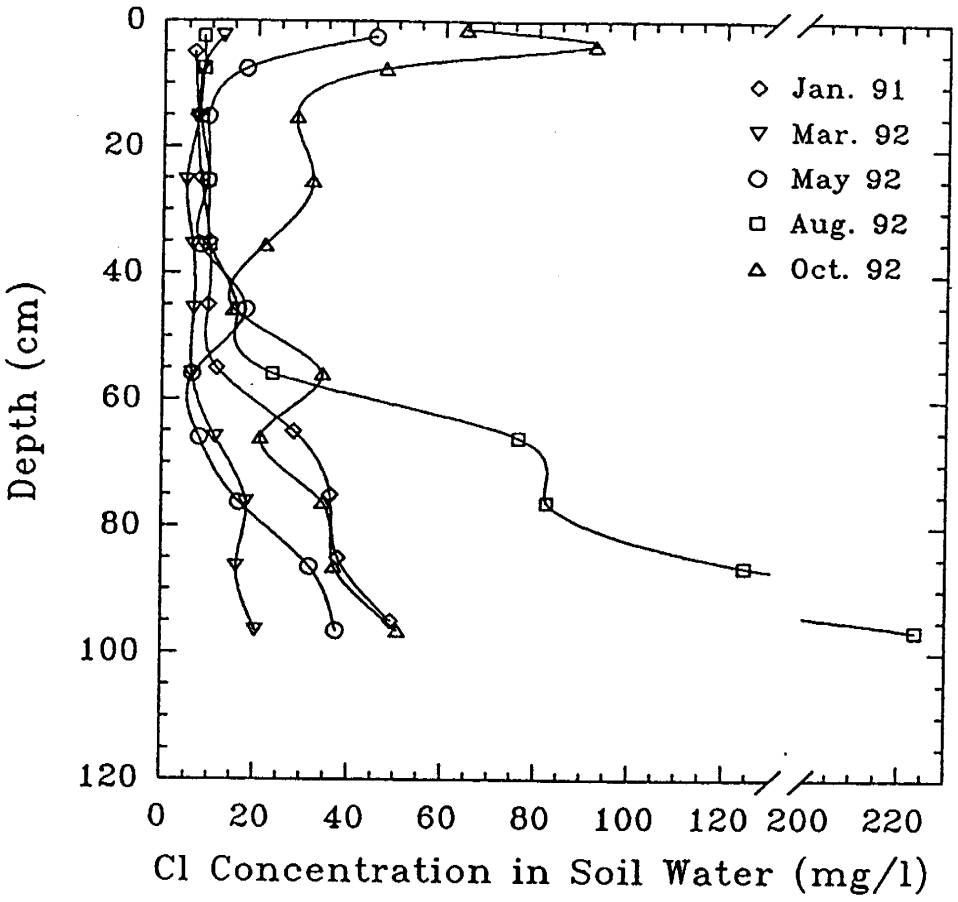

Figure 7.3 Cl depth profiles from Qt2.

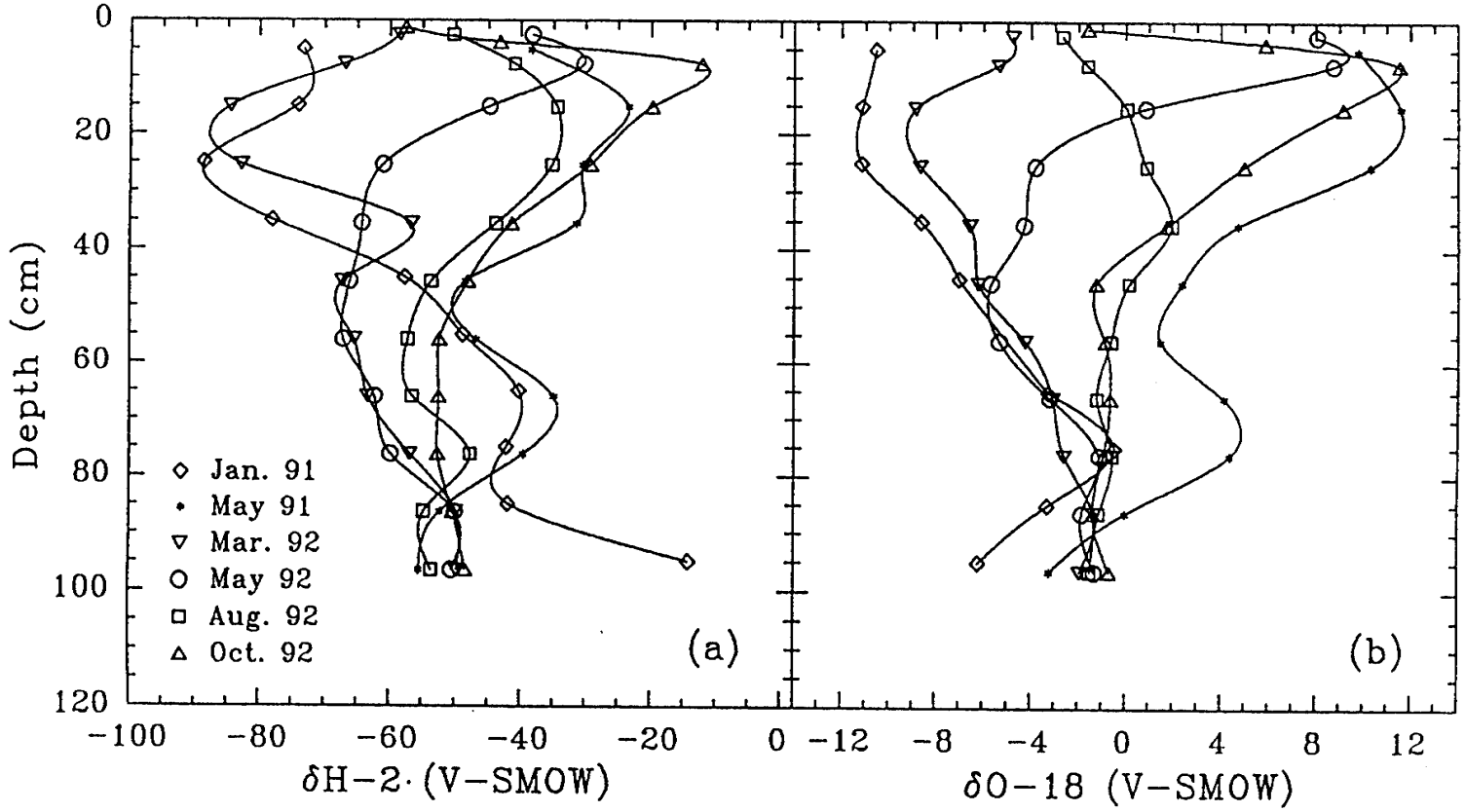

Figure 7.4 δ^2H and $\delta^{18}O$ depth profiles from Qt2. Six δ^2H depth profiles in (a), and six $\delta^{18}O$ depth profiles in (b) were sampled during 1991 to 1992. The significance of the symbols in (b) is same in (a).

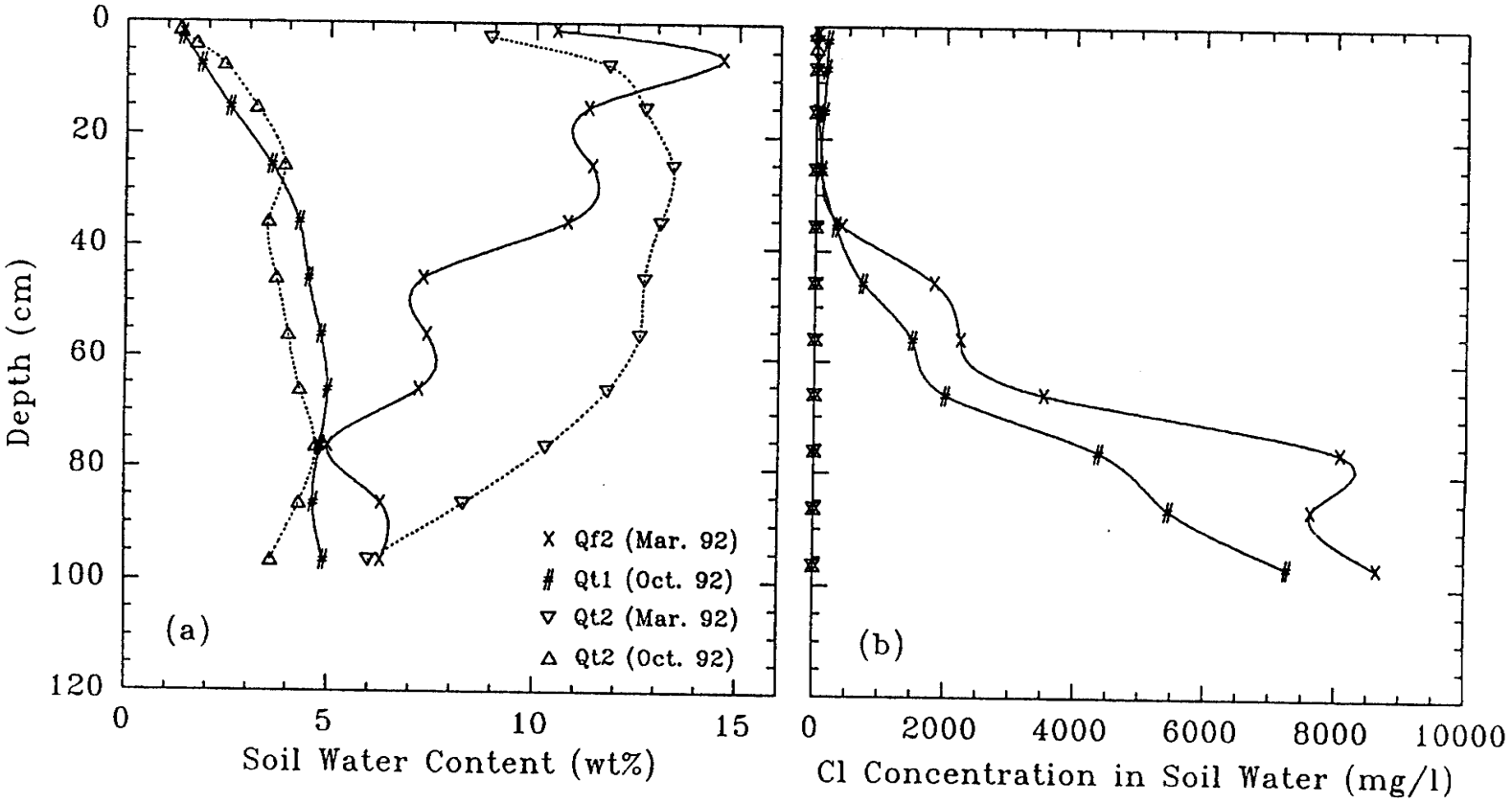

Figure 7.5 Soil water and Cl profiles from Qt1 and Qf2. Soil water contents in (a) and Cl depth profiles in (b) were sampled in October 1992 for Qt1 and in March 1992 for Qf2. The dotted lines in (a) represent the soil water contents from Qt2 sampled at the same time.

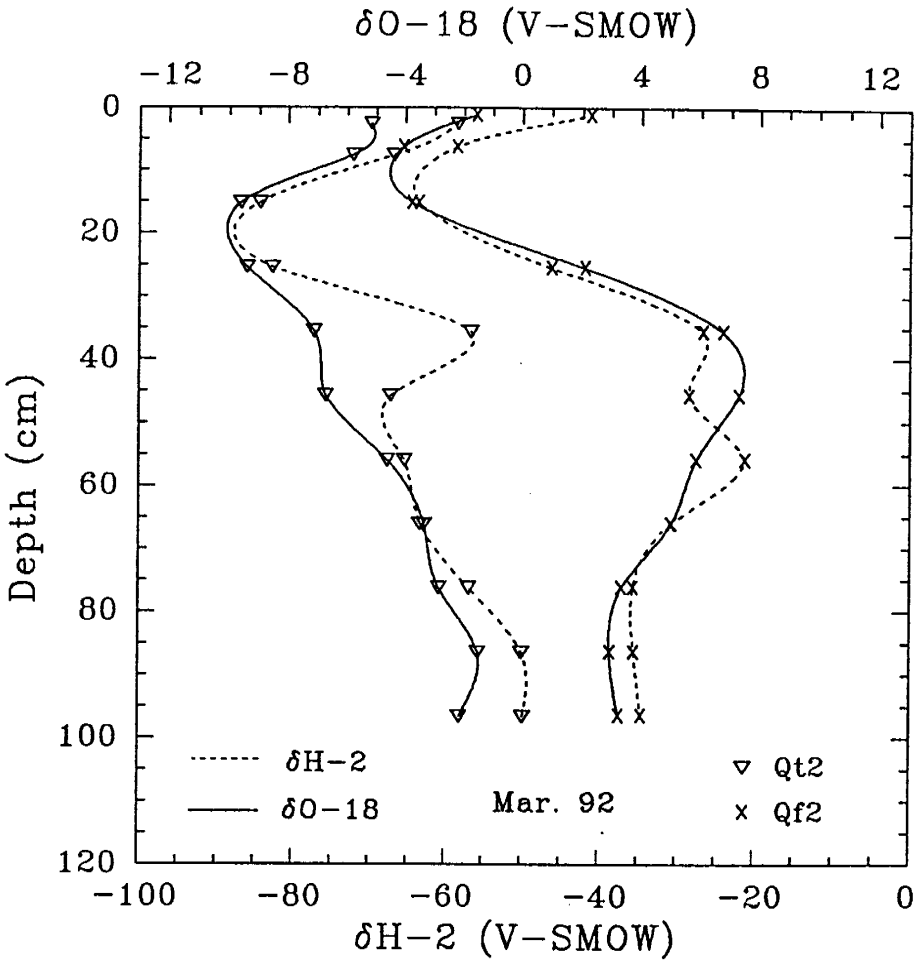

Figure 7.6 δ^2H and $\delta^{18}O$ profiles from Qf2. The H and O isotope profiles from Qt2 sampled at the same time (March 1992) is also plotted for comparison.

Qt1 and Qf2.

All the measured soil water contents and Cl concentrations, and H and O isotope compositions are listed in Appendix 6 and 7, respectively.

7.4. Discussions

7.4.1. Cool Wet Season

The rainfall in the study area is almost evenly distributed in the winter (December to February) and summer (July to September) seasons (Hendricks, 1985). The soil profiles collected in winter and early spring (January and March) have the highest soil water content in the top 60 to 80 cm of the profiles (see Figure 7.2). This is a response to the relatively high precipitation and low evapotranspirative demand in the winter rainy season. However, below 60 to 80 cm, the soil water content can be as low as 4 wt%, indicating that the effect of precipitation rarely extended below 80 cm for the period of this study. The ^{18}O and ^{2}H profiles show generally decreasing values with increasing depth until a minimum is reached at 20 to 30 cm depth of the profiles, then increase with depth, and finally tend to be constant at the bottom of the profiles. These profiles are similar to the typical profile from wet soils without a dry layer at the surface (Allison et al., 1983).

7.4.2. Summer Monsoon Season

The summer monsoon is the other major rainy season in the study area, but because of high evapotranspiration due to high temperature, the soil response to the rainfall in this season differs from that in the winter rainfall season. Although one soil profile (SP#4) was collected only one day after a thunderstorm in August of 1992, soil water content higher than 10 wt% existed only in the top 30 cm of the profile. Below 40 cm the soil water content was only about 5 wt%, implying that water input had not yet reached this depth. Apparently, downward water flux is considerably less in the summer than in the winter, although the precipitation is almost same in these two seasons. This suggests that the soil is maintained in a serious water deficit condition due to high evapotranspirative demand in the hot season, in spite of frequent inputs from the thunder storms. The ^{18}O and ^{2}H profiles for this season, in contrast to those for the cool wet season, have a maximum bulge occurring approximately 10 to 20 cm below the surface, followed by decreasing ^{18}O and ^{2}H with increasing depth, and finally converge with the profiles measured during the winter. This type of profile with a $\delta^{2}H$ or $\delta^{18}O$ maximum below the surface is typical of dry soils (e.g., Barnes and Allison, 1982; Knowlton et al., 1989). The soil water movement in the dry soils is controlled by both vapor-dominant transport near the surface and liquid-dominant transport below the evaporation front indicated by the $\delta^{2}H$ or $\delta^{18}O$ maximum bulge.

7.4.3. Dry Season

There are two dry seasons between the winter and the summer monsoon season. May and June are usually the driest months, during which the day temperature can be higher than 40 °C while there is almost no rainfall. October and November are the other dry months during which rainfall is significantly less than the two wet seasons. The high evapotranspirative demand and low precipitation cause water loss from the top part of the soil profile where soil water was stored during the wet season. Consequently, the whole top meter soil profile has low soil water contents ($\leq$ 5 wt%) in the dry season (see Figure 7.2). Similarly, the ^{18}O and ^{2}H profiles develop maximum bulges below the surface, indicating that vapor transport dominates the soil water movement in the zone near the surface.

To summarize the characteristics of the soil profiles in the different seasons, the profiles may be considered to be composed of two zones with different behaviors responsive to the seasonally environmental changes. The top 60 to 80 cm of the soil is an "active zone", where the soil water contents and the shapes of the $\delta^{2}H$ and $\delta^{18}O$ are strongly influenced by the amount of precipitation and evapotranspiration. In this soil zone, the soil water content and the transport phase change cyclically. The stable isotope profiles clearly show this behavior, developing $\delta^{2}H$ and $\delta^{18}O$ bulges starting at the surface and then moving progressively deeper. The stable isotope profiles formed during evaporation from a bare soil surface reflect the two stages of evaporation that discussed above. During the first stage, from a wet soil which meets the evaporative demand, the isotopic enrichment

resembles that for a saturated soil, with an exponentially-shaped isotope profile, similar to our profiles of January and March of 1992. After the first stage, the soil surface begin to dry and the evaporation rate falls to reach a quasi steady-state (Barnes and Allison, 1988) during the second evaporation stage. During the transition time from the first evaporation stage to the second stage, the evaporation front gradually moves downward from the surface and vapor transport is dominant above the evaporation front. In response to this change, the maximum of δ^2H or $\delta^{18}O$ (the location of evaporation front) in the isotope profile, initially at the surface, starts to gradually move downward from the surface and a minimum is developed at the surface (see the profiles for the hot seasons in Figure 7.4) as predicted by Barnes and Allison (1983). In contrast, below the "active zone" of approximately 80 cm deep, the soil water contents and the stable isotope values show little change for all the seasonal profiles regardless of the variations of the environment. For example, the isotope profiles in the bottom part have fairly constant $\delta^{18}O$ and δ^2H values at approximately -2‰ and -50‰, respectively, while the shape of the isotope profiles in the top "active zone" in the winter and early spring is opposite to that in the summer and fall.

This cyclic phenomenon can also be seen from the changes in the slope of δ^2H vs. $\delta^{18}O$. A linear relationship between δ^2H and $\delta^{18}O$ for Qt2 is shown in Figure 7.7a, in which the individual profile slopes vary between a low of about 2 for the driest season in May and a high of about 4 for the wettest season in January and March, with an overall slope of 2.5 for all the data from different seasons for Qt2.

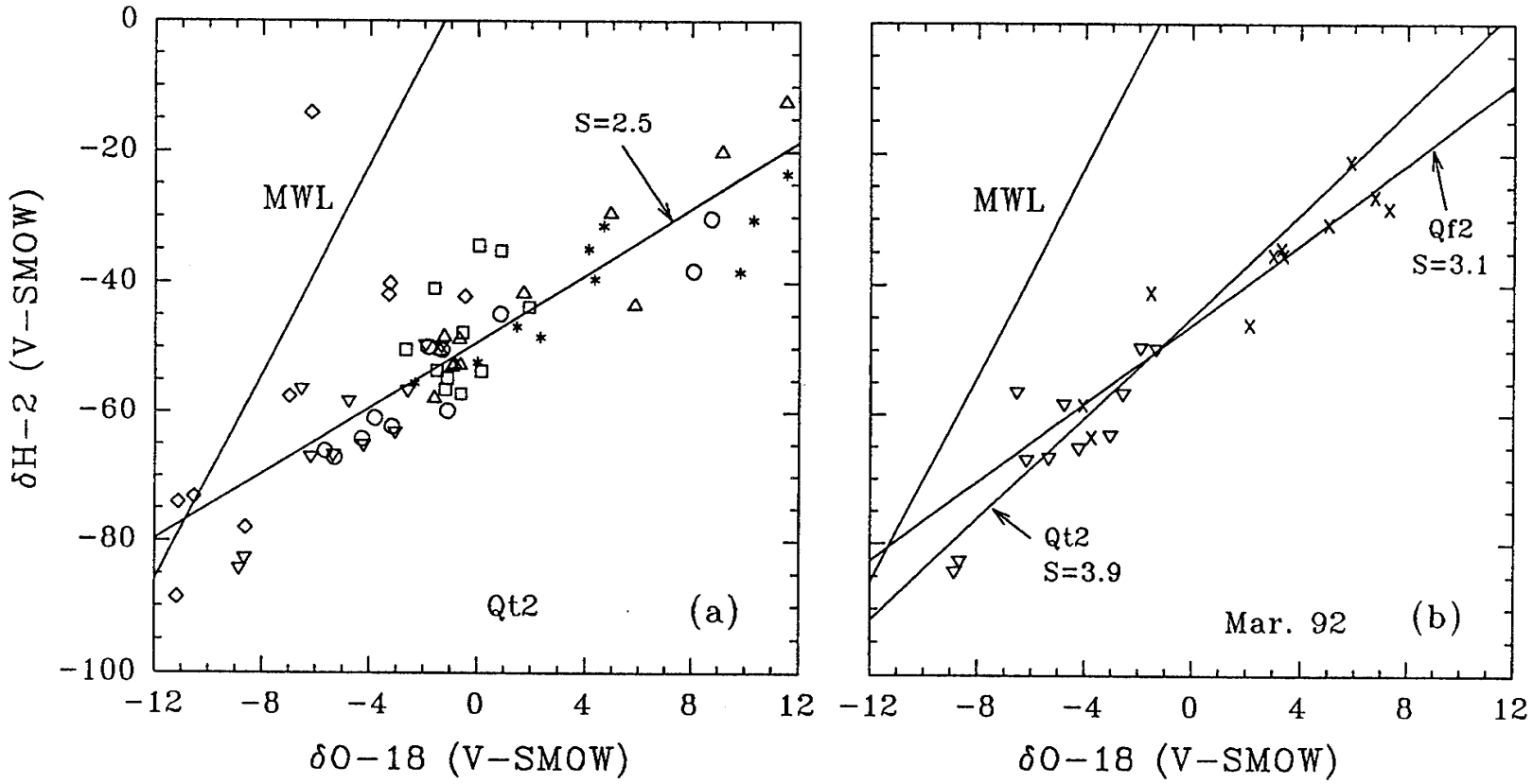

Figure 7.7 Relationship between δ^2H and $\delta^{18}O$. (a) All the H and O isotope data from the six Qt2 soil profiles, except for the one at the left top region, yield a best fitting slope of 2.5. (b) The best fitting slope for the H and O isotopes of Qf2 (March 1992) is 3.1, lower than of the Qt2 (3.9) sampled at the same time.

All the slopes are markedly lower than that for the meteoric water line (MWL) of Craig (1961), which is a slope of 8. This low slope is characteristic of soil water subject to evaporation through a dry surface layer (Barnes and Allison, 1983; 1988). In Figure 7.7a the samples collected in the winter of 1991 and in the early spring of 1992 are distributed closer to the MWL at the lower end of the overall regression line, while the samples collected in the dry seasons (May of 1991, May and October of 1992) are located farther from the MWL at the upper end of the regression line, and the samples collected in the summer of 1992, a monsoon season, are distributed in the intermediate range. This may be explained by a mixing process combined with a cyclic buildup and decrease of soil moisture (Barnes and Allison, 1982). In the study area the conditions for soil that has experienced gentle and steady precipitation through a whole winter season can be close to that for saturated soils for which the slope of δ^2H vs. $\delta^{18}O$ is about 5 (Allison, 1982). At the end of the wet season, the soil begins to dry without further rainfall input, while the ^2H and ^{18}O of the soil water become more enriched due to isotope fractionation by evaporation. The vapor-dominant transport layer near the surface develops gradually, so that the slope of δ^2H to $\delta^{18}O$ is reduced and the depth of the evaporation front increases from the winter to the summer. In the summer monsoon season, the residual soil water from the last winter season is not simply displaced by the infiltrating summer precipitation but also mixes with it. As a result, the δ^2H and $\delta^{18}O$ in the soil water for this season fall between those from the wet and dry seasons, reflecting the mixing process. Modeling of unsaturated

zone solute and isotope profiles by Cook et al. (1992) indicates that only when the recharge rate is much more than 100 mm/yr are the seasonal variations in stable isotopic compositions preserved over period of several years. In desert areas the soil water at depth is generally well mixed by the seasonal cyclic process before it is displaced to depth. Diffusion also tends to homogenize the seasonal variations in isotopic composition when the recharge rate is low (Cook et al., 1992). Thus, the H and O isotopic compositions of the soil water below the "active zone" represent averages of the soil water infiltrating throughout the annual precipitation cycle. The H and O isotopic composition of the recharge water in this area can then be correlated with that of the average annual precipitation, rather than the lighter H and O isotopic composition that may be characteristic of individual heavy rainfall events.

7.4.4. Profiles on Qf2 and Qt1

The Cl concentrations in the soil water of Qt1 and Qf2 are much higher than those of Qt2, implying that the soil water on the Qt1 and Qf2 is quite old in terms of Cl mass accumulation. This is consistent with the surface ages estimated by the cosmogenic ^{36}Cl in the surface boulders and by the degree of soil development. The shapes of the ^{18}O and ^{2}H profiles for Qf2 sampled in March of 1992 are similar to those for Qt2 (SP#3) sampled at the same time, however, the Qf2 profiles shift in the direction of more enrichment in heavy isotopes (see Figure 7.6). The slope of ^{2}H against ^{18}O for the profile on Qf2 is 3.1 (see Figure 7.7b) which is slightly

lower than that for the profile sampled at the same time on Qt2, suggesting more evaporation on Qf2 than on Qt2. It is notable that the soil water infiltrated deeper on the youngest surface (Qt2) than on the older surface (Qf2) in the winter season (see Figure 7.5a). In the hot season, on the other hand, the older surface (Qt1) seems to retain more water below approximately 30 cm deep of the soil profile than the youngest surface does in the hot dry season (see Figure 7.5a). In other words, the soil depth affected by the environmental change is thinner on the older surfaces. It is also notable that the Cl concentrations of the soil water for these two older surfaces show a sharp increase below approximately 30 cm depth in the profiles. This sharp change in Cl concentration is correlated with the Bk and Bt horizons on Qt1 and Qf2, respectively. Thus, the bottom of the "active zone" for these two older surfaces may be constrained by the top of their more advanced Bk or Bt horizon. Compared with the active zone of approximately 80 cm thick on Qt2, the older surfaces apparently have much thinner active zone that terminates at approximately 30 to 40 cm below the surface.

7.5. Water Flux Estimation

7.5.1. Steady-State Evaporation on Qt2

Since the potential evapotranspiration is much higher than the precipitation in the study area (Hendricks, 1985), the soil water can not meet the evaporative demand at most times, except for a very short period after significant rainfalls in

the winter as the isotope profiles of January 1991 and March 1992 have suggested. It is likely that the evaporation process at most times is in the second stage characterized by vapor transport through a dry soil layer into the atmosphere. The evaporation rate at this stage may be estimated by using the vapor diffusion Equation 7.1, which gives an evaporation rate at steady-state condition after some (probably a major part) of the soil moisture has been lost by the first stage evaporation. The evaporation rates were estimated for the soil profiles in May of 1991 and May, August and October of 1992, for which the stable isotope profiles clearly show vapor transport features. The parameters used in the calculation are 0.67 for τ, 0.5 for n, 1 for h_{ef}, and 1 g/cm^3 for ρ. Z_{ef} is determined from the depth of the δ^2H maximum bulge in the δ^2H profile of the same time, θ is a weighted mean for the volumetric soil water content above Z_{ef} (assuming a bulk density of 1.8), N_s was obtained from the Smithsonian Meteorological Tables (List, 1963), D_v was calculated by the empirical function of Kimball et al (1976), and the air temperature and h_a are adopted from the monthly average values in Phoenix (Conway and Liston, 1990).

The result is presented in Table 7.1, in which the estimated evaporation rates for these four profiles range from 20 to 56 mm/yr. It can be seen that the major controlling factor for the estimated evaporation rates is the depth of the evaporation front, Z_{ef}. The error in this calculation may be quite large primarily because of uncertainty in the position of the evaporation front. A relative standard deviation of about 25% was estimated by Allison and Barnes (1983) in their study,

Table 7.1 Evaporation rates and relevant parameters calculated from Equation 7.1 for different sampling dates on surface Qt2

Profile No.	Time	T (°C)	N_s (10^{-6})	D_v (cm^2/s)	D_v (v/v)	θ	h_a	Z_{ef} (cm)	E (mm/yr)
SP#1-2	May 91	25	23.05	0.2669		0.03	0.25	15	31
SP#3-2	May 92	25	23.05	0.2669		0.04	0.25	8	56
SP#4	Aug. 92	32	33.83	0.2780		0.18	0.37	20	20
SP#4-2	Oct. 92	23	20.58	0.2638		0.04	0.37	10	33

Note: $D_v = 0.229(1+T/273.16)^{1.75}$, where T is in °C (Kimball et al., 1976).

but additional considerable error may be introduced due to uncertainties in the air temperature and humidity and due to ignoring the temperature gradient in the top soil profile (Barnes et al., 1989). The application of Equation 7.1 requires a steady-state or quasi steady-state condition that is usually applicable only if the desert soils that have not received rainfall for a long period. Assuming that the estimated evaporation rates approximately represent the second stage evaporation rates in summer and fall, the average rate for the two seasons is approximately 35 mm/yr, which is much lower than the regional evapotranspiration rate of 175 - 250 mm/yr given by Hendricks (1985). A higher evaporation rate is expected for the first stage evaporation because the evaporative demand is satisfied in this stage. The evaporation rate declines with the loss of the soil water until a steady-state is reached (Hillel, 1971). Not accounting for the contribution of the first stage evaporation nor transpiration may be important reasons for underestimating the evaporation rate compared with the regional rate.

7.5.2. Downward Water Flux - Cl Mass Balance

A plot of cumulative Cl against cumulative water for Qt2 shows that all the profiles (except for the profile of October 1992) in different seasons have two straight-line segments with different slopes (Figure 7.8a). A plot for Qt1 and Qf2 shows a sharp increase in the slopes at approximately 30 cm depth (Figure 7.8b). The soil water flux for the each segment may be calculated based on Equation 7.2. In the calculation, a mean annual precipitation (P) of 250 mm was used, while 0.52

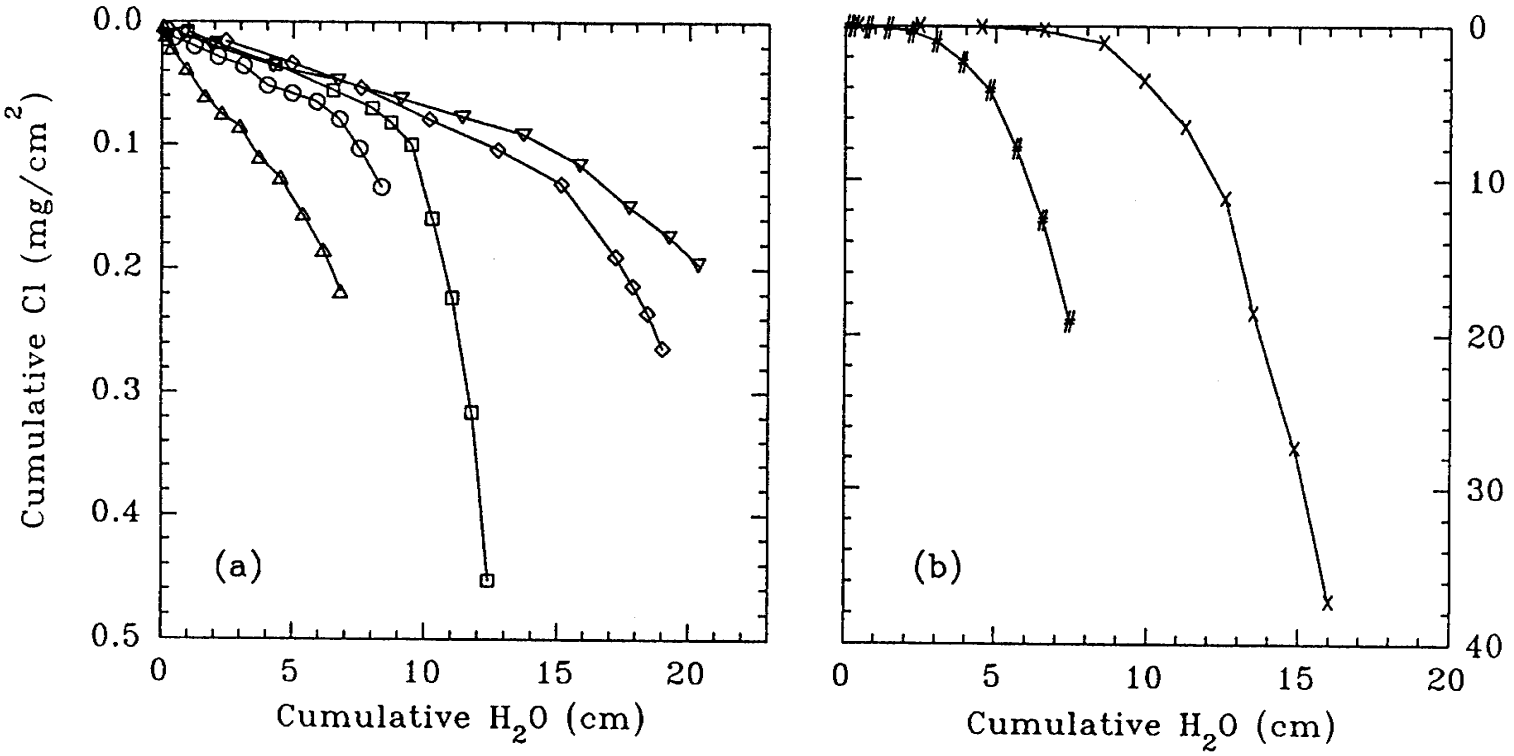

Figure 7.8 Cumulative Cl va. cumulative H_2O. (a) is for the profiles from Qt2, and (b) is for the profiles from Qt1 and Qf2. The significance of symbols in (a) for Qt2 and in (b) for Qt1 and Qf2 is same in Figure 7.3 and 7.5, respectively.

mg/l for the mean Cl concentration of fallout (C_o) was estimated by using the meteoric ^{36}Cl flux of 28 atoms/m^2.sec from the distribution of the meteoric ^{36}Cl fallout (Bentley et al., 1986) (Figure 7.9), and the pre-bomb $^{36}Cl/Cl$ fallout ratio of $400x10^{-15}$ (Figure 7.10). The assigned pre-bomb $^{36}Cl/Cl$ fallout ratio is consistent with our lowest measurement in the soil profile.

The estimated downward water fluxes are given in Table 7.2. The water fluxes for the top straight-line fragment of the Qt2 profiles in Figure 7.10a range from 4.7 mm/yr in October of 1992 to 21.0 mm/yr in March of 1992 with a mean of 13.1 mm/yr (±5.8 mm/yr), and for the bottom straight-line fragment range from 1.0 mm/yr to 7.3 mm/yr with a mean of 3.9 mm/yr (±2.2 mm/yr). The apparent water fluxes for Qt1 and Qf2 decrease markedly with increasing depth, varying from 1.3 mm/yr in the top 30 cm interval to 0.023 mm/yr for the bottom 30 cm interval in the profile of Qt1, and from 6 mm/yr for the top 20 cm interval to 0.017 mm/yr in the bottom 30 cm interval in the profile of Qf2 (Figure 7.10b). The low fluxes on Qt1 and Qf2 indicate a long residence time of water in the soil. Therefore, the soil water of Qt1 and Qf2 should be much older than that at the same depth on the youngest surface, Qt2.

Based on Cl mass balance, the Cl accumulation time calculated for the Qt2 profiles at one meter depth ranges between 10 and 35 yr (see Table 7.2), with a mean of 20 yr. The Cl accumulation time is 1500 yr at one meter depth of the Qt1 profile and 2900 yr at the same depth of the Qf2 profile. The increasing Cl accumulation times for these three surfaces are consistent with the surface

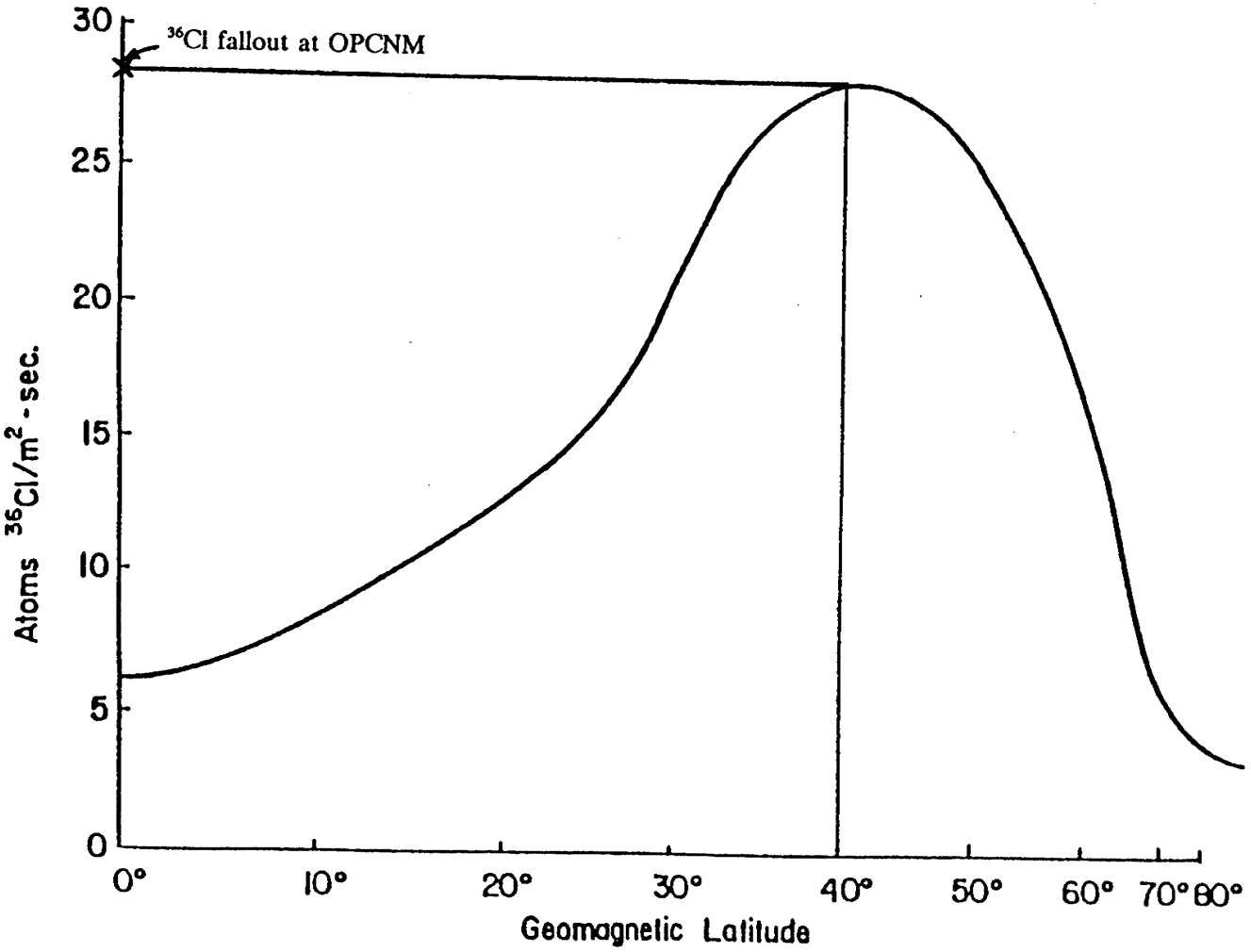

Figure 7.9 Meteoric ^{36}Cl fallout as a function of latitude. From Bentley et al. (1986).

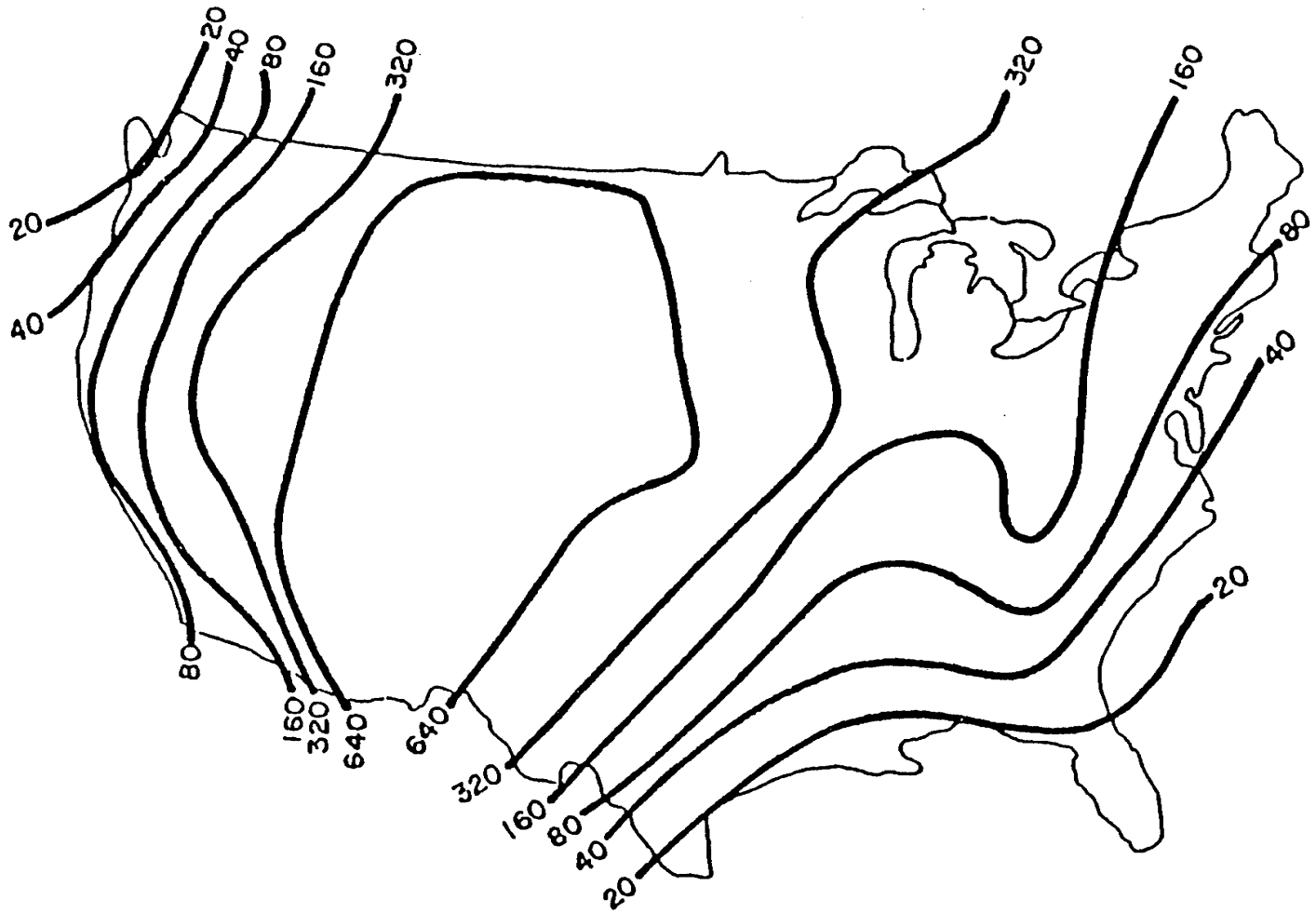

Figure 7.10 Pre-bomb $^{36}Cl/Cl$ fallout ratios. The pattern is calculated by Bentley and Davis (1982) based on box model.

Table 7.2 Comparison of calculated infiltration rates and Cl accumulation times for different sampling times and soils

Profile No.	Sampling Time	Surface Unit	Infiltration Rate (mm/yr) Cl Mass Balance		Bomb-^{36}Cl	Cl Age (yr)
SP#1	Jan. 1991	Qt2	14.2	3.9	3.4	20
SP#3	Mar. 1992	Qt2	21.0	7.3		15
SP#3-2	May 1992	Qt2	12.7	3.7		10
SP#4	Aug. 1992	Qt2	12.9	1.0		35
SP#4-2	Oct. 1992	Qt2	4.7	3.8		17
SP#2	Mar. 1992	Qf2	6.0	0.017		2900
SP#5	Oct. 1992	Qt1	1.3	0.023		1500

Note: The infiltration rates of the first column by Cl mass balance method represent the values for the top straight-line segments, those of the second column represent the values for the bottom straight-line segments.

chronosequence determined using cosmogenic ^{36}Cl (see Chapter 5, and Liu et al., 1994b) and with the relative age sequence based on the degree of soil development (Simpson, 1991). However, the Cl accumulation times are substantially younger than the actual surface ages estimated from cosmogenic ^{36}Cl and soil correlation. This suggests that significant Cl has been flushed to deeper in the profiles and that much deeper soil sampling is needed in order to account for the total inventory of Cl since the surfaces were formed.

In all the Cl profiles there are no obvious Cl bulges that are characteristic of the effect of water suction by plant roots. This is probably because either the major root zone is located deeper, or the effect of the root suction is not significant at the specific sampling locations due to the sparse distribution of the plants in this area. Since there is no significant effect of root suction found in the Cl profiles, it is likely that the water movement in the active zone is primarily driven by the suction gradient. Water and solutes may move downward in the wet seasons and upward in the dry seasons in response to changes in the direction of suction gradient. This is probably the major cause of the significant seasonal variations of the water fluxes for Qt2 estimated by Cl mass balance method (see Table 7.2). Therefore, the water fluxes for the upper straight-line segments of Qt2 probably do not result from the net downward movement of the soil water but rather the cyclic movement of the water and solute downward or upward in the different seasons. The water fluxes for the bottom straight-line segments of Qt2 may represent the average downward movement of the soil water on this surface, considering smaller

effect of the seasonal variations in this soil at this depth. Furthermore, since steady-state is required for Equation 7.2, the infiltration rates of 3.7 and 3.8 mm/yr estimated from the dry season profiles of May and October of 1992 should be more reliable.

7.5.3. Downward Water Flux - Bomb-^{36}Cl

One bomb-^{36}Cl profile was measured for the Qt2 soil profile collected in January, 1991 (Appendix 8), and the depth profile is presented in Figure 7.11. A highest bomb ^{36}Cl concentration occurs in the bottom 90-100 cm interval of the profile, and a smaller concentration peak, but the highest ^{36}Cl/Cl ratio, was measured in the top 20 cm. If the deeper peak is correlated with the bomb-^{36}Cl input around 1955 induced by nuclear weapons testing, and if piston flow is assumed, an average infiltration rate of 3.4 mm/yr is obtained by using an average volumetric soil water content of 0.15 for the top 70 cm interval and 0.06 for the bottom 30 cm interval (assuming a density of 1.8 g/cm^3). A larger infiltration rate of 5.3 mm/yr is calculated by using the soil water content of this soil profile in January of 1991. If the top peak is correlated with the 1950's bomb-^{36}Cl input, the minimum infiltration rates will be 0.8 and 1.3 mm/yr, respectively, for the two different soil water contents. The limiting infiltration rate estimated by the deeper bomb-^{36}Cl peak is comparable with the mean infiltration rate for the bottom part of the soil profiles by the chloride mass balance method.

Preferential flow through macropores may be significant for solute transport

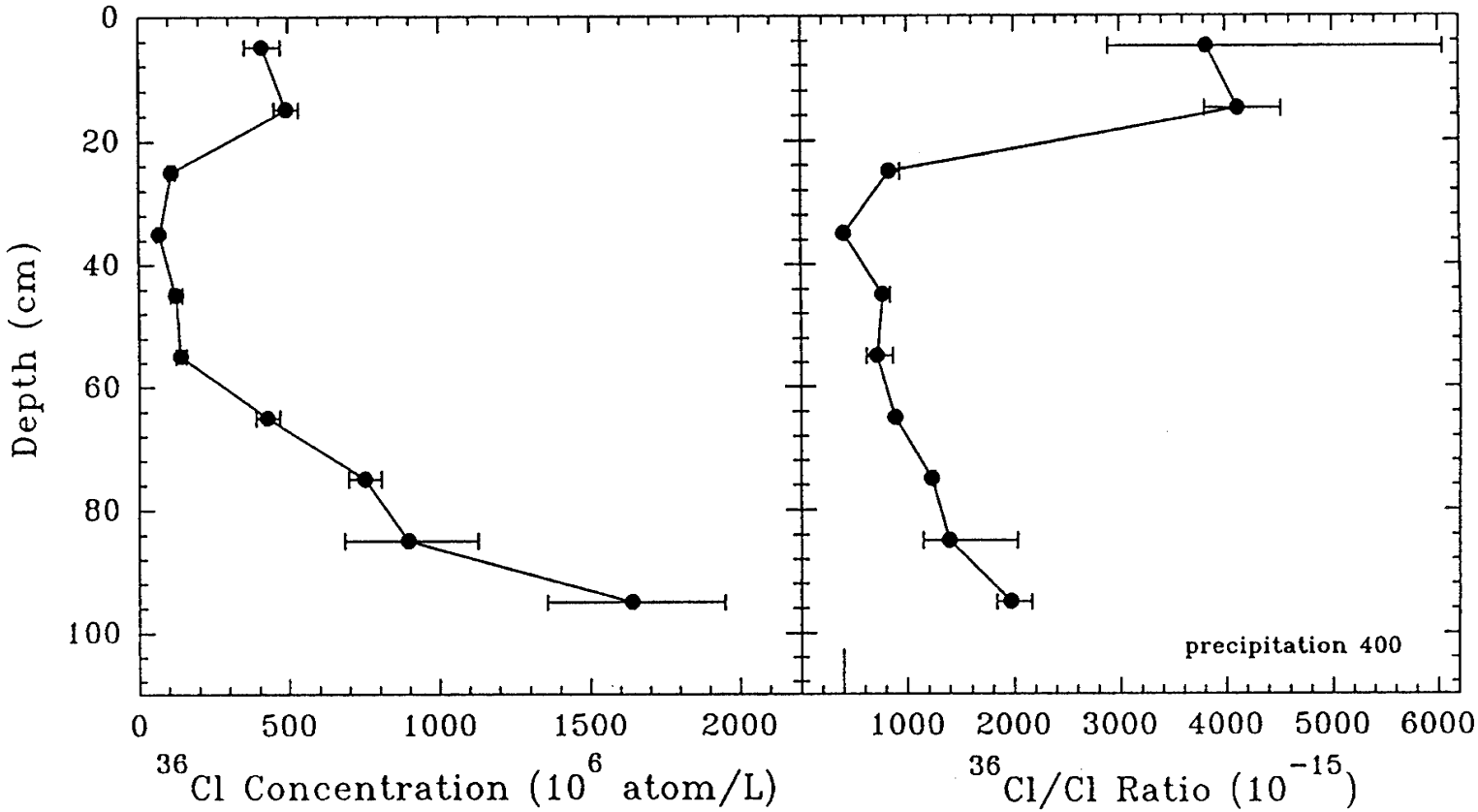

Figure 7.11 Bomb ^{36}Cl profile from Qt2. ^{36}Cl is expressed in atoms per liter of soil water. The error bar is for one standard deviation, accounted for the analytical uncertainties of both stable Cl and $^{36}Cl/Cl$ ratio.

in the vadose zone (e.g., Sharma and Hughes, 1985). Preferential flow through macropores could flush bomb-^{36}Cl deeper than would piston flow. If macropore flow is significant for the soil profiles studied, the deeper ^{36}Cl maximum could be caused by this mechanism, while the top peak could be caused by piston-flow matrix percolation. However, this phenomenon should generate Cl mass balance ages older than the residence time suggested by the deeper bomb-^{36}Cl concentration maximum. In contrast, the Cl mass balance residence times for the Qt2 profiles either are in good agreement with or are younger than the bomb-^{36}Cl residence time.

The water movement in the top active zone in our study area is characterized by cyclic movement, as discussed above. This cyclic movement and molecular diffusion will tend to homogenize the solute tracer concentrations before the water is displaced down to the deeper profile, resulting in an effective piston flow below the active zone. Some studies also suggest that piston flow is often a valid model for inert tracers in the unsaturated zone because the distance between large and small pores is usually so small that diffusion will rapidly cause the concentration of a tracer to become equal in all pores quickly (Zimmermann et al., 1967; Allison, 1988). As a consequence, all molecules of a tracer will move downward with the same apparent velocity.

Chlorine-36 profiles with double peaks in the top meter of the soil are also found in the desert soils of New Mexico (Phillips et al., 1988). Knowlton et al. (1989) evaluated this phenomenon and believed that the deeper peak is caused by

downward liquid flux while the top peak is attributed to upward liquid flux toward the dry surface layer in response to capillary pressure gradient in the dry season. We think their interpretation best explains the ^{36}Cl profile in our study area. Thus, we believe that the infiltration rates obtained from the deeper bomb-^{36}Cl peak and from the Cl mass balance in the bottom segment of the soil profiles closely represent the average net infiltration rate in this depth interval.

7.6. Significance of Soil Development in Water Regime

The inferred water fluxes decrease significantly on Qt1 and Qf2, suggesting that the development of the Bk and Bt horizons has decreased the soil permeability and increased the water retention. As a result, the thickness of the active zone of the soil water on the older surfaces is reduced due to the confinement of the low permeability and high water retention layer of Bk or Bt horizon. Compared with the youngest surface (Qt2), the much lower downward infiltration rates on the older surfaces retain more water available for evaporation above the Bk or Bt horizon, as indicated by the soil water distribution and by the greater ^{2}H and ^{18}O enrichment in the top soil profile on Qf2. In the study area the alluvial fan surfaces of Qf2 and Qf1 are major geomorphic units which have more developed soil profiles than Qt2. Especially, the oldest surface, Qf1, has an indurated petrocalcic horizon which acts as an impermeable layer at approximately 30 cm depth below the surface. The water in the matrix of the fracture-free petrocalcic

horizon is apparently immobile as indicated by the ^{36}Cl profile of the pore water in the horizon (see the discussion in the previous chapter). In this case, rain water cannot penetrate into the petrocalcic horizon, and much more water thus is available for evaporation and surface runoff. Consequently, this may change the local hydrologic condition and hence affect the geomorphic evolution.

7.7. Conclusions

Cyclic movement of the soil water in the top active zone of the vadose zone is an important phenomenon in the study area. This cyclic downward and upward movement of the soil water in the active zone has homogenized H and O isotopic compositions of the soil water in the lower part of the soil profiles, regardless of the seasonal variations at the shallower depths. Thus, the H and O isotopic compositions of the soil water below the seasonal variation zone can be related to the average isotopic compositions of the annual precipitation in this area rather than to individual heavy rainfall events. This implies that to achieve a significantly change in the isotopic composition of the water below the active zone requires a change in the composition of the average annual precipitation for a sufficient period of time for the soil water inventory in the top cyclic region to be replaced by the water with the new isotopic composition.

Based on the Cl mass balance method, the average infiltration rate below the active zone on the youngest surface of Qt2 is 3.8 mm/yr, which is in good

agreement with 3.4 mm/yr estimated based on the bomb-^{36}Cl maximum. The infiltration rates on the older surfaces Qt1 and Qf2 are apparently much lower due to lower permeability and higher water retention in the more advanced Bk and Bt soil horizons. The average steady-state evaporation rate of 35 mm/yr estimated by the δ^2H profiles of the youngest surface (Qt2) is only about 20% of the total evapotranspiration rate in this region. This may be caused by underestimating the higher evaporation rate during the first evaporation stage and because transpiration is not included.

This study indicates that as a result of soil development, the soil moisture regime has changed with time and the thickness of the active zone on the older surfaces is significant reduced due to thickening of B horizons. The change in the soil moisture regime due to soil development may have profound effect on geomorphic evolution by decreasing infiltration along with increasing evaporation and surface runoff.

8. C AND O ISOTOPES IN SOIL CARBONATE

8.1. Introduction

In semiarid and arid areas pedogenic carbonate commonly develops in soils composed of noncalcareous parent material. The C and O stable isotopes in secondary carbonate provide useful natural tracers for evaluating changes in climate and ecosystem (Quade et al., 1989; Cerling et al., 1991a; Smith et al., 1993) and the origin of secondary carbonate (Rabenhorst et al. 1984; Quade and Cerling, 1990; Marion et al., 1991). Basically, the stable C isotopic composition of the pedogenic carbonate below the penetration depth of the atmospheric CO_2 is directly related to that of the soil CO_2 which is mainly controlled by the proportion of C_4 to C_3 biomass (Cerling, 1984; Quade et al., 1989), i.e., by the density and type of the local vegetation cover. C_4 and C_3 plants favor different environmental conditions, although usually they are present both in varying proportions depending on variety of factors such as temperature, soil moisture, and seasonality (Teeri and Stowe, 1976). The character of a local vegetation cover may be indicated by the C isotopic composition of pedogenic carbonate due to significant systematic difference in the mean $\delta^{13}C$ values for C_4 plants (about -12) and for C_3 plants (about -27). Cerling (1984) and Quade et al. (1989) found that there is a good correlation between the O isotopic composition of the local meteoric water and that of modern soil carbonate, while it has been recognized that the O isotopic composition of the local

meteoric water is well correlated with the mean annual temperature (Dansgaard, 1964). Extrapolating this to the past, stable C and O of pedogenic carbonate have been increasingly used as indicators of paleo-climate and -environment (Cerling et al., 1991a; Smith et al., 1993).

However, as indicated by Teeri and Stowe (1976), the population of C_4 plants depends on a variety of factors, among which high July minimum daily temperature is the most favorable factor for growing C_4 plants. Thus, there is not necessarily a strong correlation between high mean annual temperature, (such as in hot deserts), and high proportions of C_4 plants, because some places can have very high minimum temperatures in July even though the winters are cold. The O isotopic composition of soil water controls that of pedogenic carbonate, which often develops in the top meter of soil profiles (McFadden and Tinsley, 1985). In desert areas $\delta^{18}O$ of soil water in the top meter is controlled by both liquid and vapor fluxes (Barnes and Allison, 1983; Phillips et al., 1988). Especially near the surface vapor transport is dominant, resulting in an ^{18}O maximum at the evaporation front. This typical $\delta^{18}O$ profile in the desert soils should affect the distribution of ^{18}O in the pedogenic carbonate. However, the $\delta^{18}O$ profile of soil water in the active zone of the soil profile shows seasonal variations in our study area. This may have profound effect on the O isotopic composition of the soil carbonate if carbonate preferentially precipitates in a certain season. Therefore, it is critical to correctly interpret the seasonal effects on the C and O isotope compositions of the pedogenic carbonate in order to use them as paleoclimate indicators. Furthermore,

Gardner (1984) believes that homogeneous C and O isotopic compositions in soil carbonate are attributed to carbonate dissolution/reprecipitation during the formation process. This argument can be tested by evaluating the isotope profiles on different age surfaces within a small area.

In this study the C and O isotopes of pedogenic carbonates have been investigated on four geomorphic surfaces: Qt2, Qt1, Qf2 and Qf1, with ages varying from mid-Pleistocene to Holocene. Based on the chronosequence results, correlations with paleo-climatic and -environmental conditions will be discussed.

8.2. Carbonate Precipitation

In CO_2-H_2O-$CaCO_3$ system, the precipitation and dissolution of calcite carbonate can be expressed in the following equations:

$$CO_2 + H_2O \rightleftharpoons HCO_3^- + H^+$$

$$HCO_3^- \rightleftharpoons CO_3^{2-} + H^+$$

$$CaCO_3 \rightleftharpoons Ca^{2+} + CO_3^{2-}$$

These can be summarized by a single equation:

$$CO_2 + H_2O + CaCO_3 \rightleftharpoons Ca^{2+} + 2HCO_3^-$$

In an open system in which CO_2 partial pressure is close to constant, the CO_2-H_2O-$CaCO_3$ system can be completely defined at specified temperature and total pressure under equilibrium conditions. The relationship between $CaCO_3$ solid phase and CO_2 gaseous phase is easily linked by the equilibrium constants and the

partial pressure of CO_2 in an open system (Stumm and Morgan, 1981). Since for pedogenic carbonate the rate of new soil carbonate accumulation is small (10^{-7} to 10^{-6} mole cm^{-2} yr^{-1}) compared to the CO_2 respiration flux (10^{-3} to 10^{-5} mole cm^{-2} yr^{-1}) (Quade et al., 1989), the partial pressure of soil CO_2 can be considered to be constant. Thus, the pedogenic calcium carbonate is likely to form in an open system. This has also been tested by McFadden et al. (1991)

In the CO_2-H_2O-$CaCO_3$ system, isotopic fractionation exists between each pair of phases, resulting in a systematic difference in the isotopic compositions of C and O between the precipitated carbonate and the soil CO_2 gas and soil water. The ^{18}O isotope enrichment from the H_2O liquid phase to the $CaCO_3$ solid phase at is approximately 30‰, and the ^{13}C isotope enrichment from the CO_2 gaseous phase to the $CaCO_3$ solid phase is approximately 10‰ (Friedman and O'Neil, 1977). It is generally accepted that the C isotopic composition of pedogenic carbonate is primarily determined by that of soil CO_2 which is a mixture of two components: atmospheric and plant-respired CO_2 (Cerling et al., 1991b). The O isotopic composition of pedogenic carbonate is mainly determined by that of soil water which is correlated with the local mean annual precipitation (Cerling, 1984; Quade et al., 1989).

There is another type of isotope fractionation, kinetic fractionation, involved during an irreversible chemical reaction such as the photosynthetic process (Craig, 1953). This is related to the dissociation energy barrier which causes a discrimination against the heavy isotopes of C in the products of the reaction

(Broecker and Oversby, 1971). This causes plants with different metabolic pathways to have different C isotopic compositions. Therefore, the C isotopic composition of respired CO_2 is determined by the local plant assemblage.

Appendix 9 gives the basic equations and parameters for C and O isotope systems used in the relevant calculations of this study.

8.3. Sample Collection and Analyses

Four carbonate depth profiles were collected from soils on Qt2, Qt1, Qf2 and Qf1 at sampling sites #5, #9, #10 and #6, respectively (Figure 4.3). At sampling site #10 on Qf2, carbonate accumulation is weak and coexists with clays between 20 to 40 cm depth, while an argillic horizon is well developed under the carbonate layer. Therefore, only three carbonate samples could be collected to that depth. In contrast, Qf1 at site #6 has a well developed petrocalcic horizon (see Figure 6.1) about 1.5 m thick with Stage V of Machette (1985) beginning approximately 30 cm below the surface. The carbonate profile collected on this surface is thus much deeper, with thirteen samples. Five and six samples were collected from Qt2 and Qt1, respectively, on which the Bk horizons at site #5 and #9 exist approximately between 30 and 100 cm depth interval. The carbonate samples from Qt2, Qt1 and Qf2 were collected by abrading carbonate coatings of cobbles or gravels, while from Qf1 they were collected from the indurated cement or laminar layers in the calcrete horizon. In addition, one carbonate sample was collected from an active arroyo

channel floor (site #14). Carbonate of a probably nonpedogenic origin is often found on the bed or in the walls of deep arroyos in the study area.

The carbonate samples were oven dried before loaded into the reaction vessels, and then pumped in the vacuum system for at least two hours. 100% phosphoric acid was used to react with the carbonate to liberate CO_2 gas for the mass spectrometric analyses of the C and O isotopic compositions. The stable isotope compositions were measured by Finnigan-MAT (Delta-E) gas source isotope mass spectrometry and are expressed as δ-values in parts per mil relative to the PDB standard. The analyses were conducted in the Stable Isotope Laboratory of Geoscience Department, New Mexico Tech.

8.4. Results

The result of the C and O isotopic analyses of soil carbonate for the four surfaces are given in Appendix 10. The C and O isotope depth profiles are shown in Figure 8.1a and 8.1b. The C isotope profiles for the four surfaces (see Figure 8.1a) show following features: (1) The $\delta^{13}C$ values increase with decreasing depth in the top part of the profiles and tend to converge near the surface; (2) Below the top interval, the $\delta^{13}C$ values tend to be constant with increasing depth, except for the Qf2 profile, for which the sampling depth only reaches 40 cm because the carbonate-rich horizon is very thin; (3) The younger the surface, the more depleted is the $\delta^{13}C$ of the carbonate at depth, and (4) The $\delta^{13}C$ value of the carbonate on

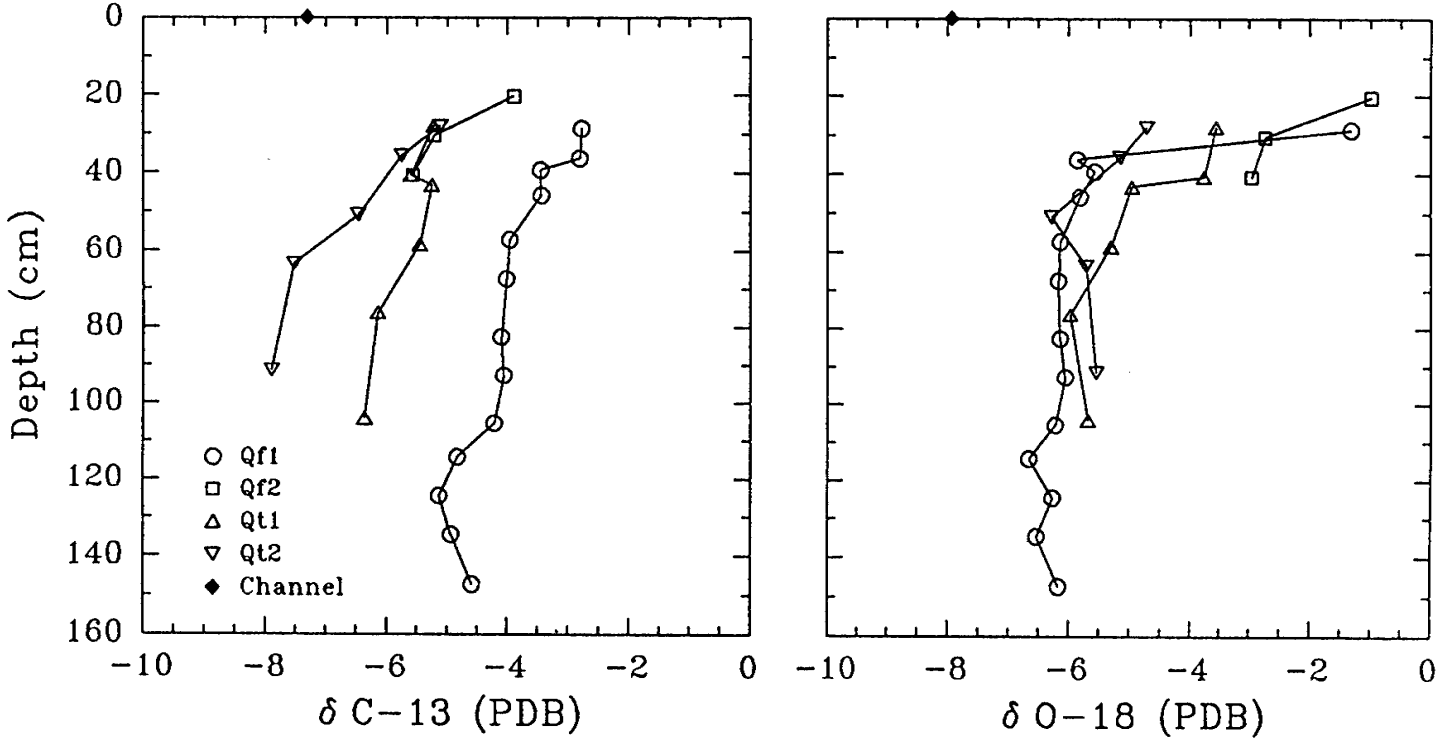

Figure 8.1 $\delta^{13}C$ and $\delta^{18}O$ depth profiles. The $\delta^{13}C$ in (a) and $\delta^{18}O$ in (b) are measured for the soil carbonate of the four surfaces.

the active channel floor is similar to that at depth in Qt2, the youngest surface. The O isotope profiles (see Figure 8.1b), however, show only small differences among the three surfaces Qf1, Qt1 and Qt2, which span the time interval between the middle Pleistocene and Holocene. All the profiles show a relatively constant $\delta^{18}O$ value of approximately -6‰ below 40 cm depth, above which $\delta^{18}O$ increases sharply. In contrast, the $\delta^{18}O$ of the carbonate from the channel floor is depleted to almost -8‰.

8.5. Discussion

8.5.1. O Isotope Compositions

O isotopic composition of pedogenic carbonate is mainly controlled by that of soil water (Cerling, 1984), because O mass in soil CO_2 is insignificant compared with soil water. $\delta^{2}H$ and $\delta^{18}O$ isotope profiles typical of the desert soils have a maximum just below the surface, such as the isotope profiles for the dry and monsoon seasons in this study area (see Figure 7.4). The overall shapes of the $\delta^{18}O$ profiles for the carbonate samples from the four surfaces resemble each other and are also similar to the typical soil-water isotope profile below the $\delta^{18}O$ maximum. The distinct increase in $\delta^{18}O$ in the top part of the carbonate profile is a response to the ^{18}O enrichment in the soil water near the evaporation front. A general trend for the four carbonate profiles is that the older the surface, the more ^{18}O enrichment in the top part of the profiles. This is consistent with the viewpoint

discussed in the previous chapter that there is more evaporation from the older surfaces due to greater water availability, because the infiltration rate is attenuated and water retention enhanced by the advanced Bk, Bt, or K soil horizons. Calculations in Figure 8.2 indicated that the measured O isotopic composition from the Qt2 carbonate profile can be produced from the mean O isotopic composition of the measured soil water at temperatures of 30 °C, which is similar to the mean July air temperature of this region (about 30 °C from Hendricks, 1985). This suggests that the soil carbonate is being precipitated during the summer season.

The O and H isotopes of the soil water on Qt2 indicate that in spite of significant seasonal changes in the soil water isotopic composition near the surface, the isotopic composition in the deeper soil water profile is relatively constant and probably controlled by the local mean annual precipitation due to cyclic movement of the soil water above. The very low infiltration rates on the older surfaces of Qt1, Qf2, and especially on Qf1, suggest that the soil water takes thousands of years, or even longer, to reach the middle of the Bk or Bt horizon. Thus, on the older surfaces the carbonate isotopic composition at depth should not be severely modified by the modern water. This is especially true for the Qf1 petrocalcic horizon, in which the ^{36}Cl distribution in the pore water indicates that the carbonate has probably not been altered since it precipitated. Thus, the relatively constant $\delta^{18}O$ values in the bottom part of the carbonate profiles may indicate the local mean annual temperature change during the time that the carbonate formed.

Quaternary climatic fluctuations in the southwestern United States have been

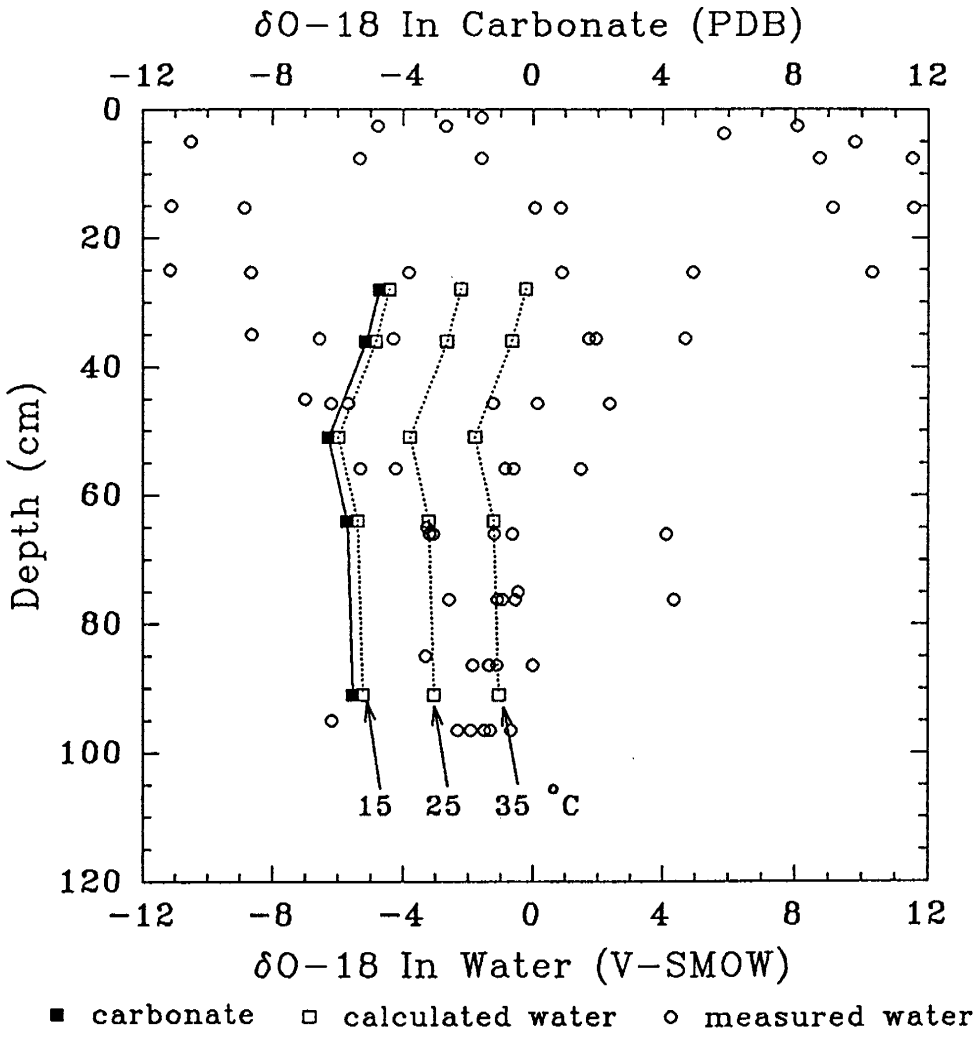

Figure 8.2 Comparison of O isotopes from carbonate and soil water. The filled squares and open circles are measured $\delta^{18}O$ values for the Qt2 soil carbonate and soil water, respectively, the open squares are $\delta^{18}O$ values calculated for soil water in equilibrium with the carbonate at 15, 25, and 35 °C. $\delta^{18}O$ for soil water is expressed relative to V-SMOW, and for carbonate relative to PDB.

found to be generally consistent with the global climatic changes (e.g., Jannik, 1989, Phillips et al, 1990, Morrison, 1991b). In our study area a climate shift from glacial to interglacial occurred approximately 11,000 yr ago (Van Devender, 1987). The signals of the climatic fluctuations should be preserved in the soil carbonate at depth if it has not been modified, as indicated above. The $\delta^{18}O$ values below 60 cm depth in the profiles from Qt2, Qt1 and Qf1 increase with deceasing surface age (Figure 8.3), suggesting that the long-term mean air temperature in this area has increased from the middle Pleistocene to the Holocene. This is consistent with the general trend of the global climate changes.

However, it is notable that the $\delta^{18}O$ values from the Qt2 and Qt1 carbonate samples in the depth only show a small difference (see Figure 8.3). As Qt2 is of Holocene age, when temperatures were presumably highest, and Qt1 is latest Pleistocene, probably from the Wisconsin glacial period, one would expect significant differences in $\delta^{18}O$ values between the soil carbonate samples from these two surfaces. I propose two hypotheses that could explain the small $\delta^{18}O$ difference in the soil carbonate between Qt1 and Qt2. First, the combined isotopic fractionation during soil water evaporation and carbonate precipitation tends to minimize the difference of the O isotopic composition in the carbonate precipitated at different temperature conditions, as suggested by Gardner (1984). For example, in a higher temperature environment, soil water would be more enriched in heavy isotopes due to increased evaporation, but ^{18}O enrichment between the soil water and the carbonate would be less due to smaller isotopic fractionation factor at

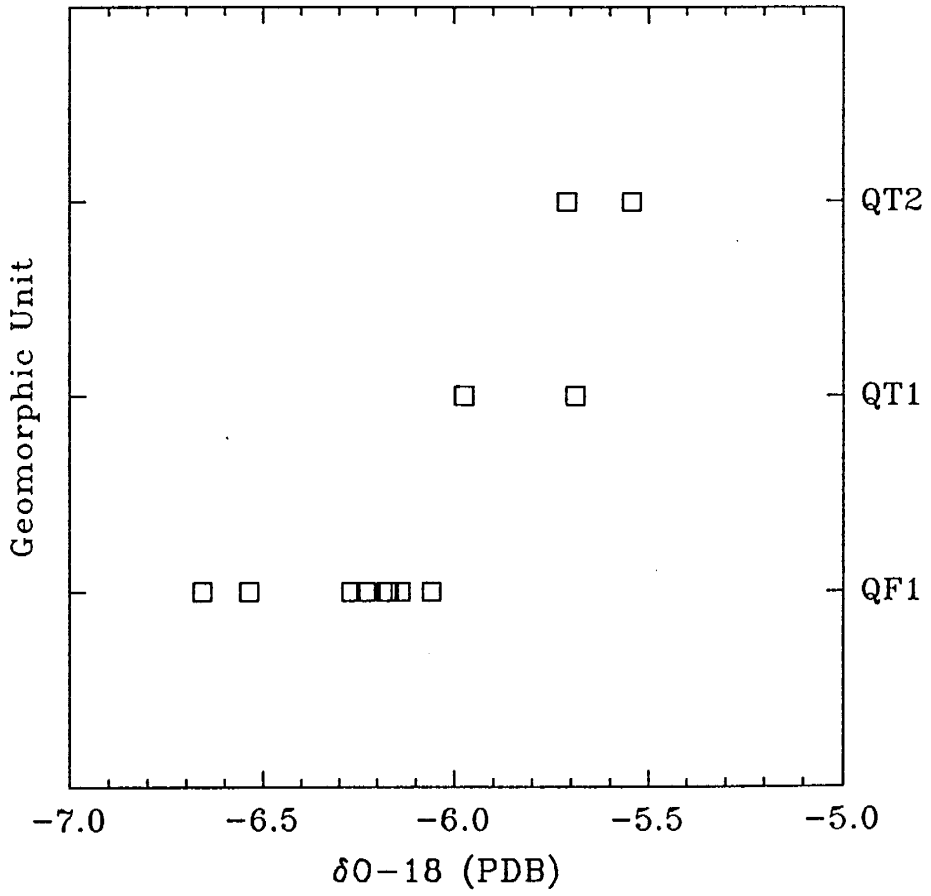

Figure 8.3 $\delta^{18}O$ distribution in time. The general trend is that ^{18}O concentration increased from the oldest surface (Qf1) to the youngest surface (Qt2).

higher temperature. A reverse process would happen in a lower temperature condition. Consequently, the sum of the isotope fractionation for the two processes of soil water evaporation and soil carbonate deposition might tend to be similar. On the other hand, soil carbonate precipitates when soil water reaches saturation of $CaCO_3$. Presumably, more evaporation is needed for precipitating soil carbonate in glacial than in interglacial although ^{18}O in precipitation is more depleted at a cool climate condition than at a warm climate condition. The combined effect of temperature and isotopic fractionation is illustrated in Figure 8.4a, and the effect of evaporation in Figure 8.4b, in which the kinetic isotopic fractionation factor is assumed to be the same as that at 80% relative humidity. Second, the Qt2 soil carbonate may be formed with combination of in situ pedogenic carbonate and recycled calcrete from the active channel. The carbonate sample collected from the active channel floor is very depleted in ^{18}O, compared with any carbonate samples from the soil profiles. It is likely that the calcrete on the channel floor is precipitated from groundwater and surface runoff. The O isotopic composition of runoff is largely controlled by the rainfall, which is isotopically much lighter than the soil water due to less evaporation.

8.5.2. C Isotope Compositions

Figure 8.1a shows the $\delta^{13}C$ values at the bottom of the profiles from Qt2, Qt1 and Qf1 have significant differences. This does not seem to support the hypothesis that dissolution/reprecipitation during carbonate formation will tend to homogenize

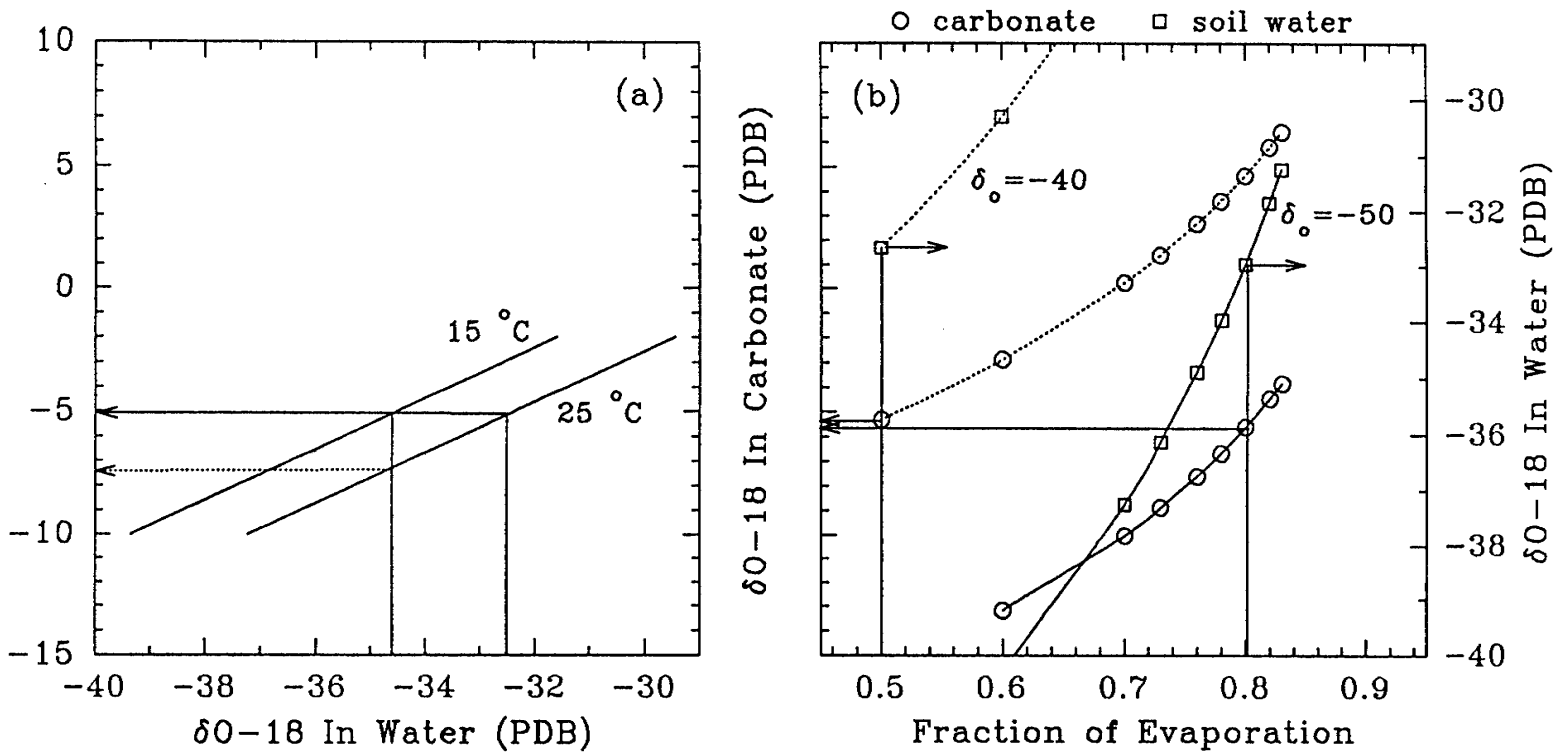

Figure 8.4 Temperature and evaporation effects on $\delta^{18}O$ in carbonate. (a) illustrates that two soil waters with ~ 2‰ difference in O isotopic composition can produce similar O isotopic composition in carbonate under temperature difference of 10 °C. (b) illustrates that two soil waters with 10‰ difference in initial O isotopic composition can precipitate similar O isotopic composition in carbonate under 30% difference in evaporation degree.

the isotopic compositions of pedogenic carbonate through time as suggested by Gardner (1984). Rather, the carbonate from each individual surface with different age exhibits a distinct profile as predicted by Cerling's diffusion model of 1984. Based on Cerling's model, the C isotopic composition of pedogenic carbonate is controlled by two components, atmospheric CO_2 and soil CO_2. The $\delta^{13}C$ value of the atmosphere (about -7‰) is much higher than that of the soil CO_2, and it is relatively constant, with only approximately 1 per mil change between glacial and interglacial (Marino et al., 1992). This explains the tendency of the $\delta^{13}C$ values of all the profiles to increase towards the surface and to tend to converge.

Plants with different metabolic pathways have different C isotopic compositions. $\delta^{13}C$ in C_3 plants ranges between -22 and -35‰ with a mean of about -26‰ (Farquhar et al., 1982, Vogel, 1978), in C_4 plants it ranges between -9 and -16 with a mean of about -12, and in plants with the crassulacean acid metabolic (CAM) pathway it ranges between -9 and -19 with a mean of -17 (Robenhorst et al., 1984). The significant differences in $\delta^{13}C$ among the carbonate profiles are probably caused by different C isotopic compositions in the soil CO_2 which in turn is controlled by the local vegetation cover (e.g., Cerling, 1984, Quade et al, 1989). In general, C_3 plants are abundant in temperate environments while C_4 plants favor high temperature and high water stress conditions, although both often occur in mixtures. The $\delta^{13}C$ values for the Qt2, Qt1 and Qf1 carbonate samples below 60 cm depth show a clear trend that, as the surfaces become younger, they become more depleted in ^{13}C (Figure 8.5), suggesting that C_3 plants

have become more abundant and the fraction of C_4 to C_3 plants has decreased from the middle Pleistocene to the Holocene. This implies that the temperature might decrease or precipitation might increase since middle Pleistocene, which is opposing the O isotope result. Van Devender suggested (1987) that the present climate is hotter and drier than that of the terminal glacial period, based on his examination of vegetation assemblages in the pack rat middens of the past 14,000 yr from the Puerto Blanco Mountains, approximately 15 km southwest of our study area, and from the Ajo Mountains right in our study area. Apparently, the stable C isotopic composition from the Qt2 and Qt1 carbonate samples are not consistent with Van Devender' conclusion. In addition, an inverse relationship exists between the C and O isotopes in the soil carbonate (Figure 8.6), which is contrary to the relationship found by Cerling (1984) and Quade et al. (1989).

Based on previous studies of relationship between vegetation and stable C isotope of soils, most C_4 plants are grasses (e.g., Cerling et al., 1991), while most shrubs and scrubs are C_3 plants (e.g., Amundson et al., 1988, Parada et al., 1983). After examining vegetation cover in the study area, it has been found that this area has an admixture of C_3 and CAM plants, dominated by C_3 plants at the sampling sites such as creosote bush, triangle-leaf bursage, with few C_4 grasses. To be consistent with the O isotope result, an alternative explanation would be that the temperature increased while vegetation community changed from more grass to less grass. Since the Qf1 petrocalcic horizon is very old, formed during a long period approximately between 200,000 and 500,000 yr ago (^{36}Cl ages for the petrocalcic

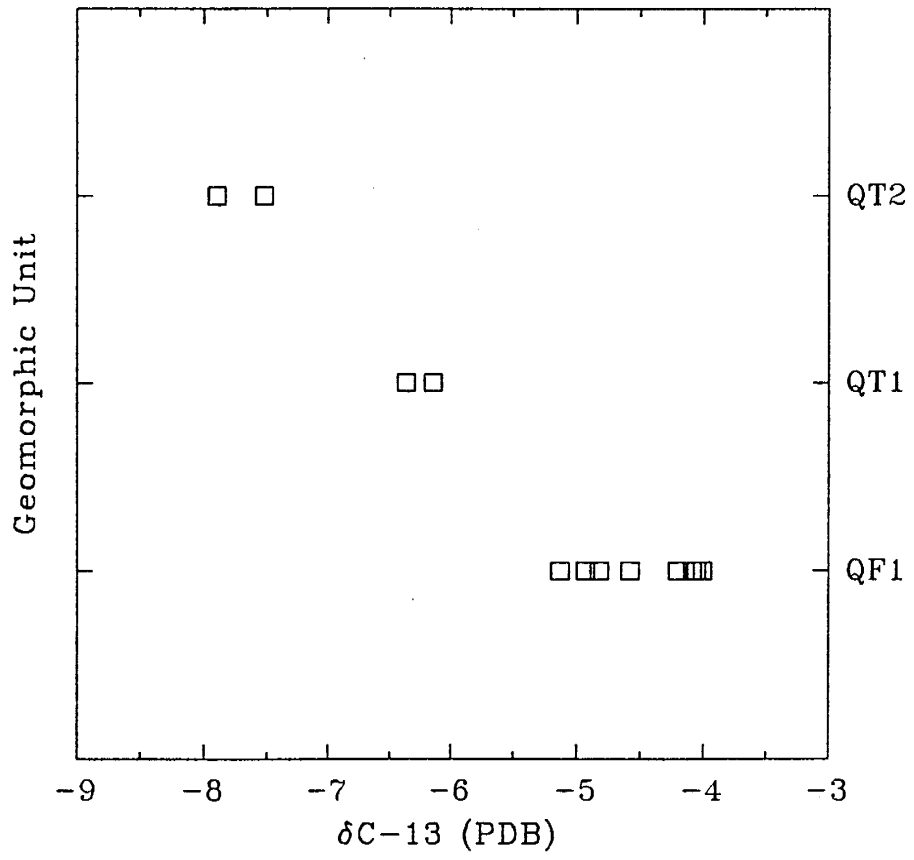

Figure 8.5 $\delta^{13}C$ distribution in time. The general trend is that $\delta^{13}C$ decreased from the oldest surface (Qf1) to the youngest surface (Qt2).

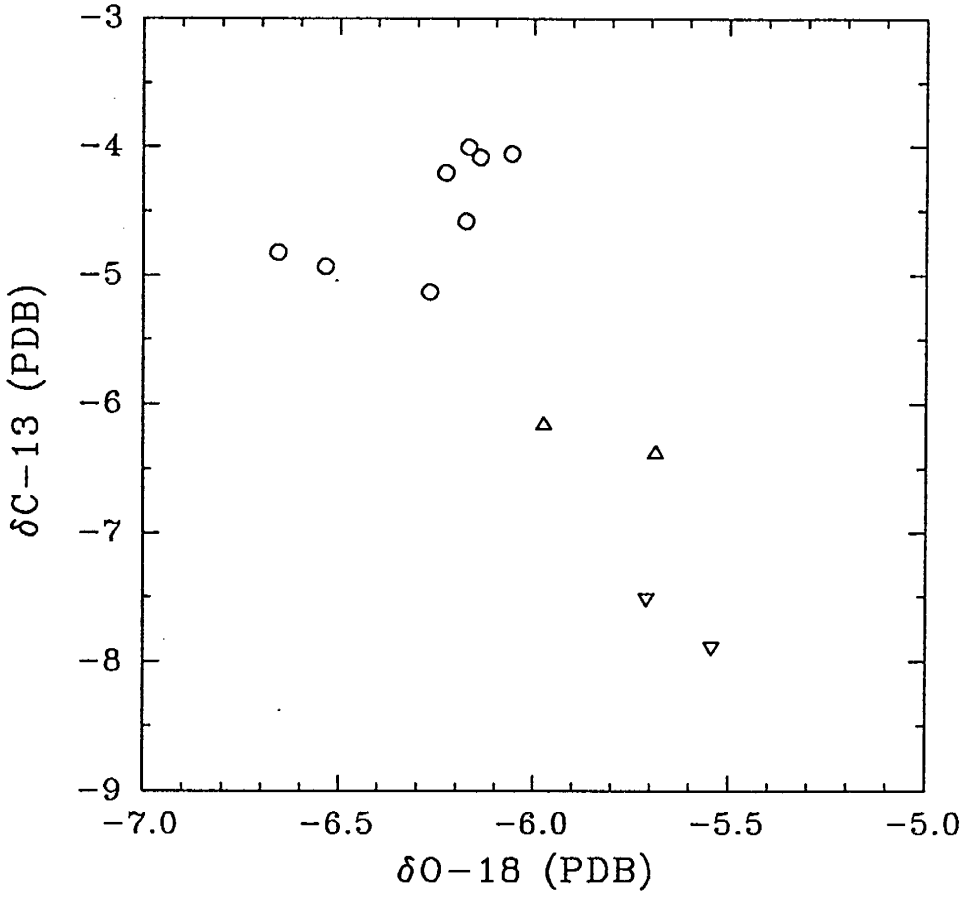

Figure 8.6 Relationship between $\delta^{18}O$ and $\delta^{13}C$ in carbonate.

horizon), there is only weak evidence regarding the climatic condition during that time. It seems possible that the high ^{13}C and low ^{18}O concentrations in the carbonate in the petrocalcic horizon could be produced in a grass-dominated environment but with a mild climate favorable for C_4 plants. In contrast, there is better information regarding the climatic transition from the latest Pleistocene to the Holocene (Van Devender, 1987). The stable C isotope of the soil carbonate from Qt1 and Qt2 does not clearly indicate this change. Rather, it suggests that the present environment is more favored by C_3 plants. A study of $\delta^{13}C$ of the most common plants and of soil CO_2 in the Tucson basin by Parada et al. (1983), about 150 km east of this study area, also indicates that the dominant plants are C_3 type and that C_4 plants are less than 10%. They also found that the soil CO_2 has an average $\delta^{13}C$ value of -18‰ at their long-term monitoring site and of -20‰ at a discharge location. The latter is close to the $\delta^{13}C$ value of CO_2 required in equilibrium with carbonate having a $\delta^{13}C$ value of -7 to -8‰, similar to that of the Qt2 carbonate at depth. This suggests that even under the Holocene climate, it is possible to form pedogenic carbonate with quite depleted ^{13}C. Based on the record of atmospheric CO_2 concentration from a ice core, Cole and Monger (1994) attributed the decline of C_4 plants during the last deglaciation in south-central New Mexico to a result of a significant increase in atmospheric CO_2 concentration since the last glacial maximum. This could be the reason that the vegetation cover in my study area shifted from a C_4-plants-dominated to a C_3-plants-dominated land since mid-Pleistocene.

There are some other possible explanations for the stable C isotopes from the Qt1 and Qt2 soil carbonate. The youngest surface, Qt2, is located on the topographically lowest terrace by arroyos, and the older terrace, Qt1, is situated above it. Water stress in the Qt2 soil may be lower than that in the Qt1 soil because more water can be caught on the topographically lowest surface, Qt2. As a result, the microenvironment on Qt2 is more favored by C_3 plants. In the active stream channels the most common plants are palo verde, which are C_3 plants. Consequently, the stable C isotopic composition of the calcrete on the channel floor is very depleted in ^{13}C. The similar C isotopic compositions of the channel floor carbonate and of the soil carbonate in the soil depth of the youngest surface, Qt2, may suggest that part of the carbonate in the Qt2 soil is actually recycled channel calcrete, as discussed for the O isotope. However, it is difficult to interpret the consistent trend from the mid-Pleistocene to the Holocene solely by recycling the channel calcrete.

8.6. Conclusions

C and O isotope profiles for the four surfaces in the study area suggest that dissolution/reprecipitation of the soil carbonate has not homogenized the carbonate composition during the development of the soil profiles. The individual carbonate profile for each surface has preserved its own signals related to the climate and micro-ecosystem at the sampling location when the soil carbonate precipitated.

This supports Cerling's gas diffusion model (1984) for C isotope distribution in soil CO_2. This study shows that Cerling's model can be used for surfaces older than Holocene. The O isotopic composition in the soil carbonate below the active zone can be related to that of the local mean annual precipitation.

C and O isotope in the soil carbonate suggests that the temperature increased from the mid-Pleistocene through the latest glacial to Holocene while the environmental conditions in the study area have apparently become more favorable for C_3 plants from the middle Pleistocene to the Holocene. The C isotopic composition in soil carbonate may largely reflect vegetation cover in micro-environments that are determined by comprehensive factors, including regional climate, atmospheric CO_2 concentration, micro-topographic, and hydrological features.

SUMMARY OF STUDY

9.1. Surface Chronology And Geomorphic History

An analytical model of cosmogenic ^{36}Cl accumulation in unstable landforms has been developed and applied in the study of alluvial chronology and in the dating of petrocalcic horizon in the western piedmont slope of Ajo Mountains, south-central Arizona. Based on the cosmogenic ^{36}Cl chronology in this study, combined with the previous geomorphic study in this area by Simpson (1991) and with the tectonic feature in this region, the geomorphic evolution of the western piedmont slope of Ajo Mountains may be described in ten stages since the tectonic activity ceased in late Tertiary. The each of the stages is illustrated in a sketch (Figure 9.1), which shows a possible change in landscape during the geomorphic history of the piedmont at that time.

Stage 1. After tectonic movement ceased, rock pediments developed and extended towards the range. The sketch is in basin-range direction. This stage might take approximately several million years.

Stage 2. New rock pediment continued to develop towards the mountain while the old pediment was gradually mantled by alluvium derived from the mountains.

Stage 3. The pedogenic carbonate started to accumulated slowly, and the oldest surface (Qf1) was finally stabilized approximately 500,000 ago. Meanwhile, the petrocalcic horizon gradually developed upward. The sketch is in the range-parallel

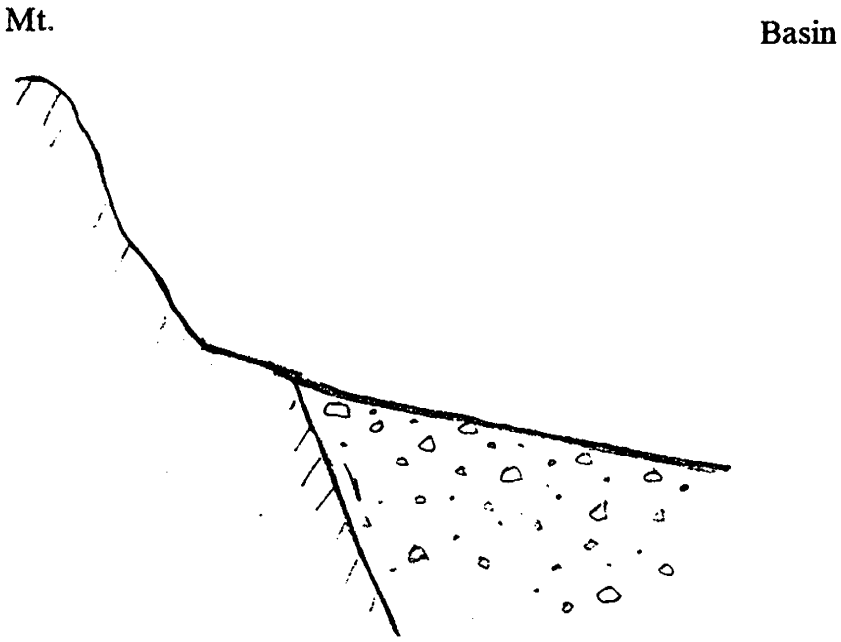

Figure 9.1 Sketches of geomorphic history.

(1) Tectonic movement was ceased and rock pediment developed towards the mountains.

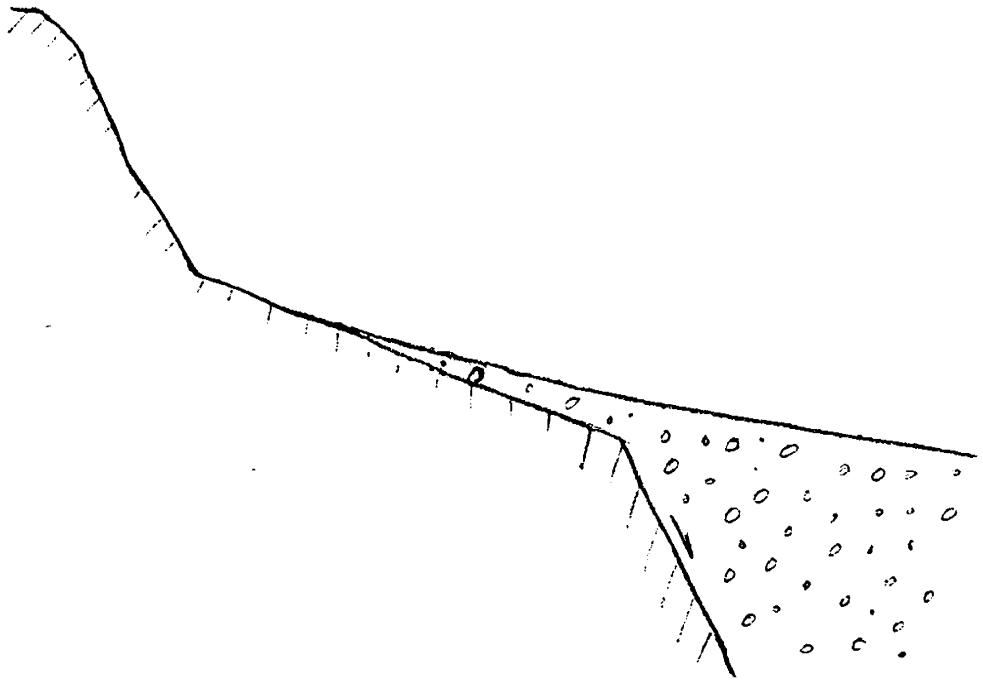

(2) New rock pediment was continuing to develop range-ward, while the old pediment was mantled by alluvium. Soil profile was developed in the alluvial sediments, and soil carbonate started to accumulate.

Parallel to the Mountains

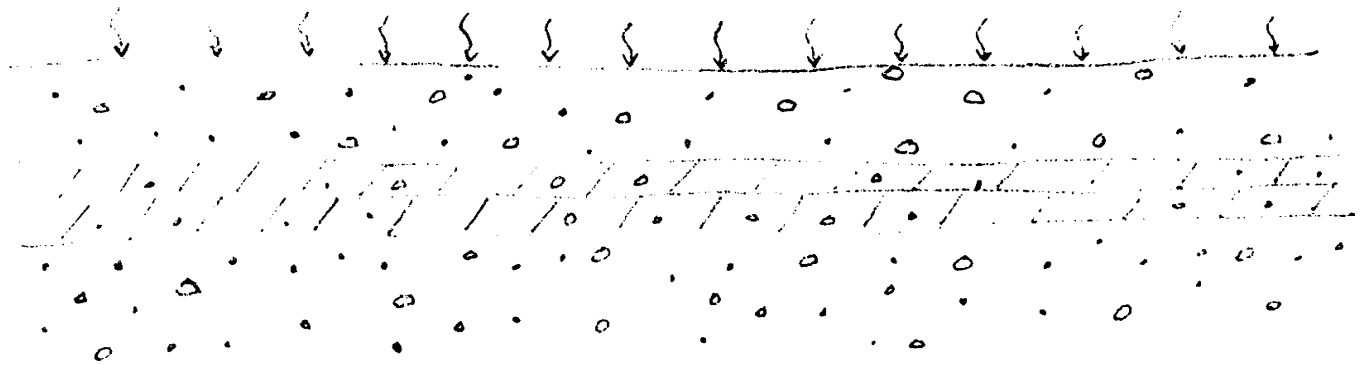

(3) The surface Qf1 was stabilized and petrocalcic horizon was developed to the stage such that the formation of the horizon was almost completed. The direction of this sketch (and thereafter) is parallel to the mountains.

direction. Thereafter the sketches will be drawn in this direction.

Stage 4. A major surface reworking for this oldest surface occurred approximately between 230,000 and 330,000 yr ago. Most of the top loose material was stripped off the surface such that only occasional large boulders survived. In contrast, the petrocalcic horizon was largely preserved due to its high resistance to degradation.

Stage 5. Following the reworking at Stage 4, the incisions were filled and the petrocalcic horizon was mantled by new deposits which provide a strong signal for this event. A new petrocalcic layer was added to the older petrocalcic horizon.

Stage 6. The oldest surface (Qf1) was extensively reworked again. Deep trenching might be a characteristic of this event.

Stage 7. Backfill of the trenches and basin-ward deposition between 200,000 and 100,000 yr ago resulted in the formation of a new and broad surface (Qf2).

Stage 8. Both Qf1 and Qf2 were worked again between 32,000 and 55,000 yr ago. Meanwhile the older terrace (Qt1) was formed either by stripping the older surface or by depositing new material, or by both.

Stage 9. The older terrace (Qt1) started to take shape by incision of the old channel deposits (Qt1) about 15,000 ago, while the younger terrace (Qt2) began to deposit.

Stage 10. Finally, the younger terrace (Qt2) was incised by the modern active channels.

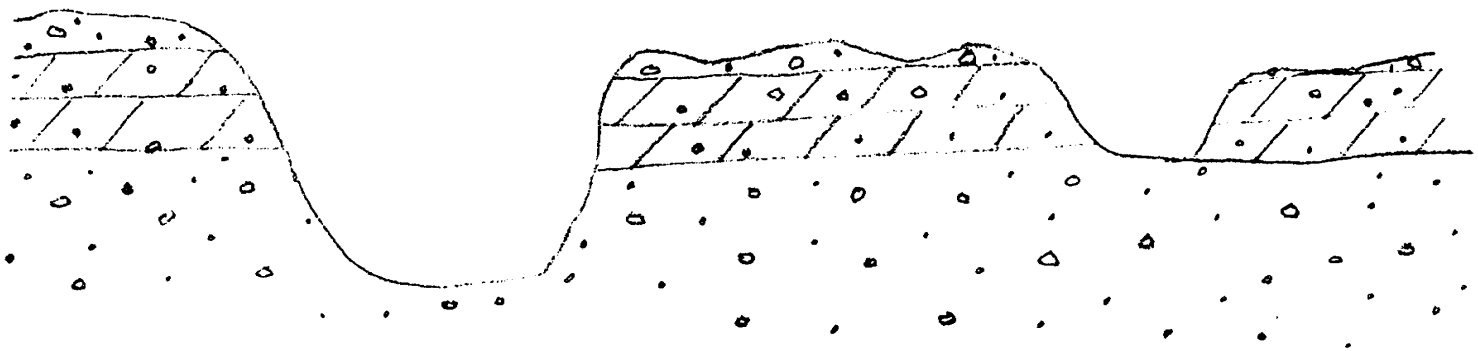

(4) Qf1 was reworked first time. Top loose soil was almost completely stripped off so that only big boulders were survived.

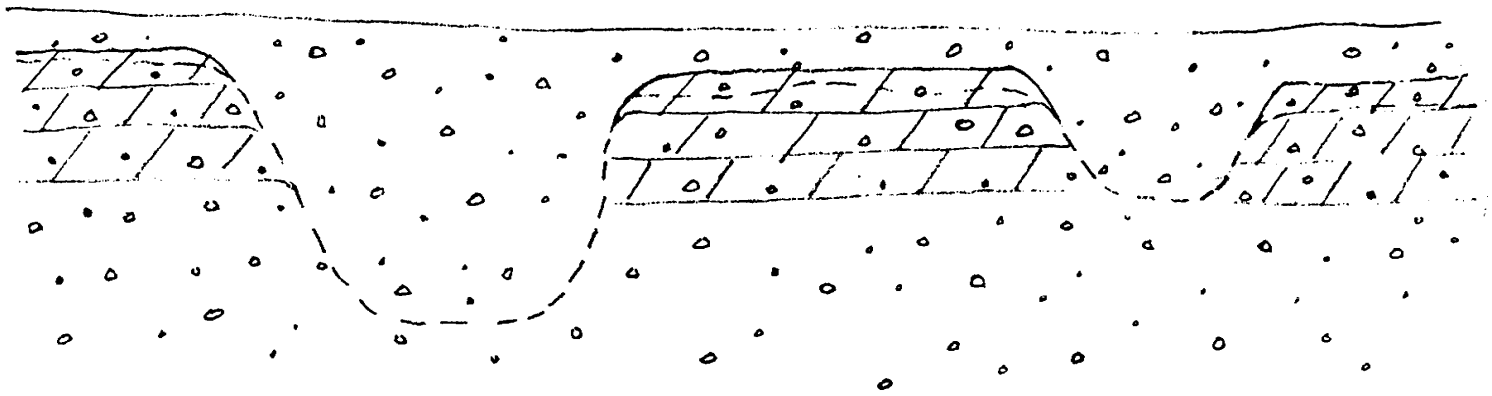

(5) New alluvial material filled the trenches and mantled the petrocalcic horizon.

A new top-loose soil layer was formed on Qf1.

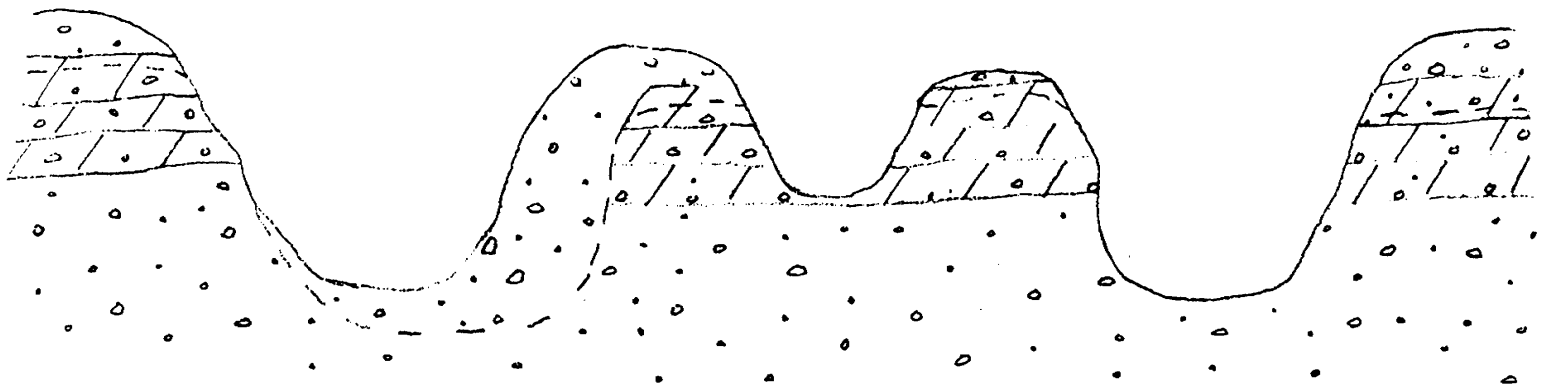

(6) Qf1 was deeply trenched, but in contrast to the first reworking event, the top loose soil was only partially eroded.

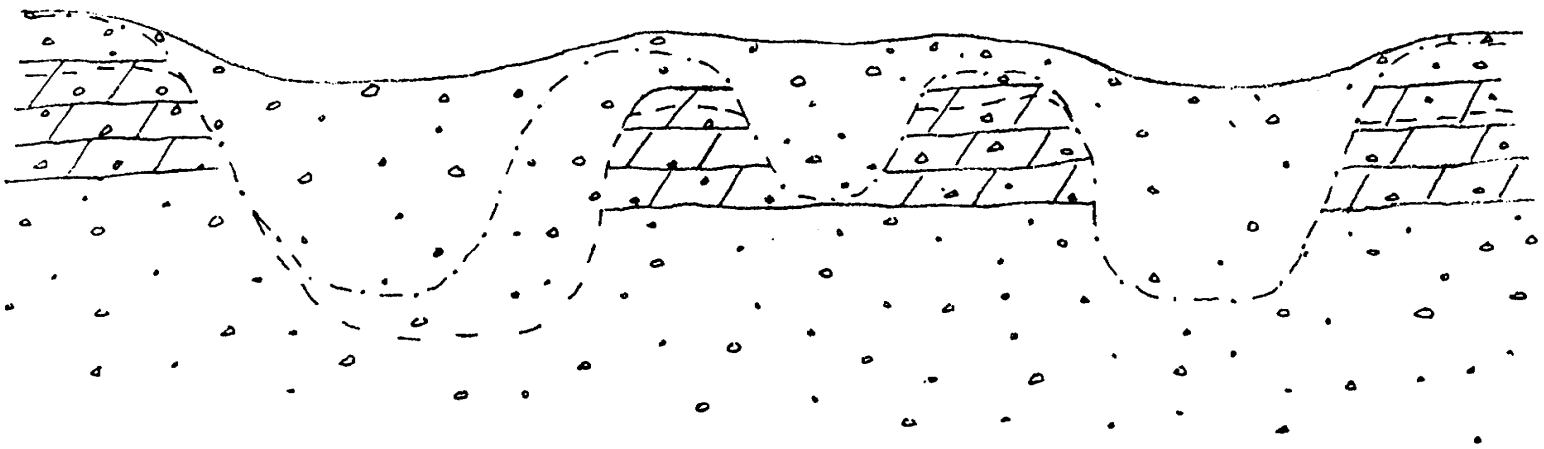

(7) Alluvial material backfilled the trenches to form a topographically lower, stratigraphically younger surface, Qf2.

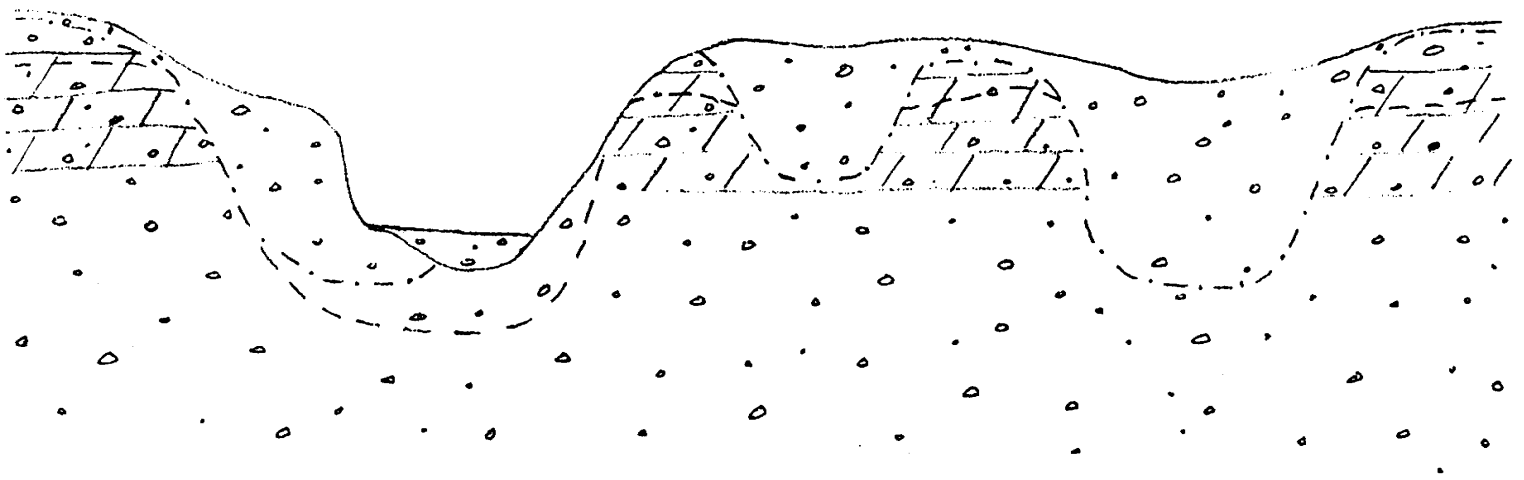

(8) Both Qf1 and Qf2 were reworked, followed by incision and deposition of the older terrace (Qt1) as backfill in the incised channels.

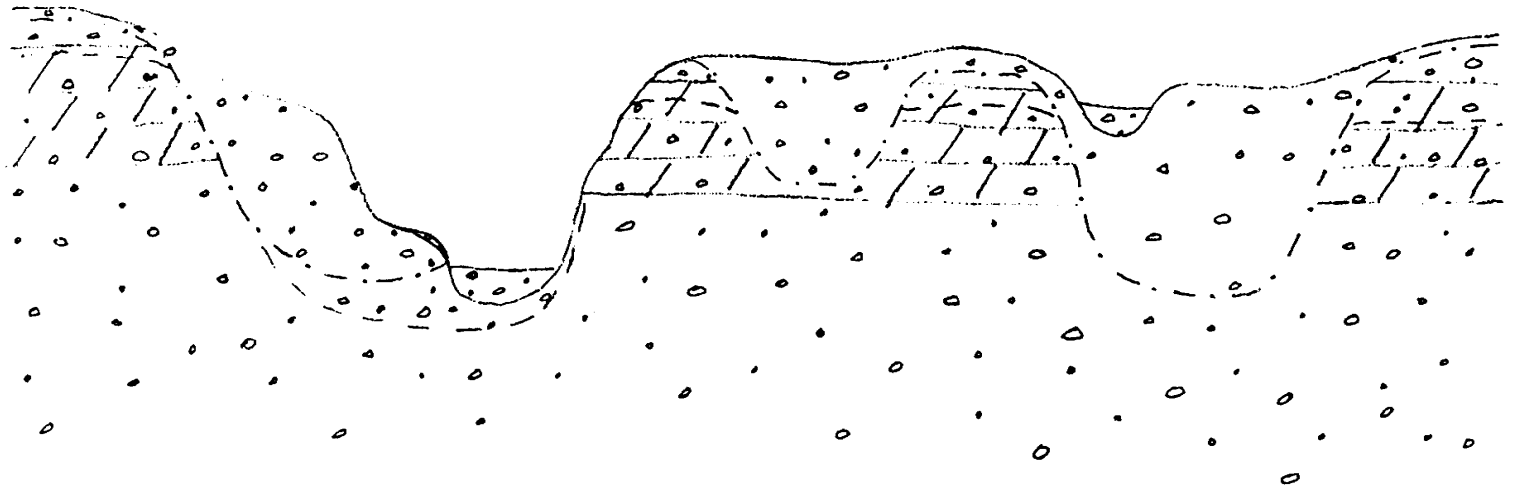

(9) Qt1 was reworked by incision of the channels, and the younger terrace (Qt2) was deposited as the channel deposits.

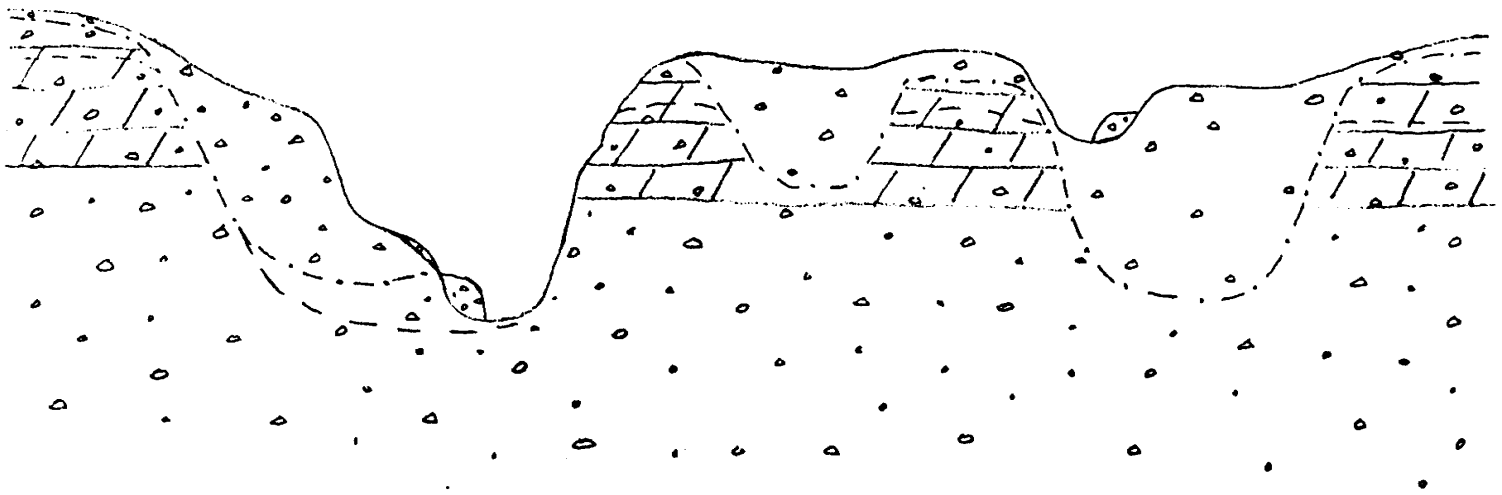

(10) Modern stream channels incise Qt2, and the formation of today's landform feature has been completed.

One thing should be pointed out for these sketches is that since there is neither subsurface information nor deep exposure of the deposits, it is difficult to indicate the structural detail for the study area. In other words, it is not clear whether or not the study area is located on the basinward of the basin-bounding normal faults. However, considering the very slow mountain front retreat rate obtained in this study (18 mm/1000 yr) and the relatively short distance of the study area from the mountain front (approximately 500 to 2000 m), it was therefore assumed in the sketches that the study area is located near the basin-range structural divide.

9.2. Soil Water Flux And Evolution Of Soil Moisture Regime

According to environmental Cl mass balance and bomb-^{36}Cl in the soil profiles, the infiltration rate below top soil active zone on the youngest surface (Qt2) is about 3-4 mm/yr. In contrast, the infiltration rates on the older terrace (Qt1) and the young fan surface (Qf2) are as low as 0.02 mm/yr based on Cl mass balance method. On the oldest fan surface (Qf1), the infiltration rate is essentially zero in the fracture-free petrocalcic horizon. The average steady-state evaporation rate on the youngest surface Qt2 (35 mm/yr), estimated by δ^2H profiles, is only about 20% of the regional evapotranspiration rate given by Hendricks (1985). Not accounting for transpiration or higher evaporation rate during the first stage evaporation is considered to be the major grounds responsible for this discrepancy.

Based on the investigation of the seasonal variations in soil water movement

by stable O and H isotopes and environmental C and bomb-^{36}Cl, it has been found that cyclic movement of soil water in the active zone, which is approximately 60 to 80 cm thick on the youngest surface (Qt2), tends to homogenize the isotopic compositions of the soil water. The thickness of the active zone or soil moisture regime is not only determined by the local climatic condition but also by the soil texture and structure. The soil texture and structure are primarily controlled by the surface age in the study area, namely, the older the surface age, the thinner the active zone of the soil profiles. The results in this study indicate that the change in the soil moisture regime due to soil development has caused a decrease in water infiltration rate and increase in evaporation rate. This may have profound effect on geomorphic evolution.

9.3. Paleoclimatic and Paleoenvironmental Change

In this study, the stable O and C isotopes in the soil carbonate from the different surfaces, aging from middle Pleistocene to Holocene, showed distinct profiles that are consistent with Cerling's gas diffusion model of 1984. This suggests that soil carbonate from different age surfaces within a small area can be used for paleoclimate study. The O isotopic composition in the soil carbonate profiles from the two fan surfaces (Qf1 and Qf2) and two terraces (Qt1 and Qt2) indicates a general trend that the O isotopic composition has become more enriched in ^{18}O since middle Pleistocene. This may suggest that the air

temperature in the study area has increased since the mid-Pleistocene. Stable C isotopic composition, however, suggests that the environmental condition became more favorable for C_3 plants from middle Pleistocene to Holocene. The vegetation cover possibly shifted from grass-dominated community to a shrub-dominated one. However, recycled carbonate from the active channel floor, with much lighter O isotopic composition, may play a role in the formation of Qt2 soil carbonate. The inverse correlation between the C and O isotopes suggests that vegetation cover could have more complex response to the climatic change rather than has been postulated by other investigators (e.g., Cerling, 1994, Quade et al., 1989).

9.4. Future Work and Suggestions

The cosmogenic ^{36}Cl investigation in this study has indicated that significant inherited ^{36}Cl in the alluvial material caused difficulties of obtaining accurate surface ages for the two terraces. Other dating methods, such as varnish ^{14}C and ^{14}C for organic matter in the soils, are suggested to use for age determination in the future work. The initial test of applying cosmogenic ^{36}Cl to dating petrocalcic carbonate suggested that this method is potentially useful for soil dating. However, evaluating this technique is still difficult due to lacking of independently reliable age constraints. I suggest that the future tests should be conducted in a site where the surface and soil ages have been well constrained by multiple dating methods.

This study emphasized using natural tracers to estimate water flux. Piston flow

was the major assumption for estimating the downward water flux, and quasi steady-state is an assumption for estimating the upward water flux. It would be preferable to combine both chemical and physical approaches for this kind of study in order to check assumptions and results. In addition, the study of seasonal variations in the soil profiles only reached one meter deep. It would be valuable to investigate deeper profiles on a seasonal basis.

In this study, the stable O and C isotopes from different age surfaces within a small area yielded very good paleoclimatic signals from middle Pleistocene to Holocene. The results suggested that stable O and C isotopes in soil carbonate can be used for evaluating paleoclimatic fluctuations back to Pleistocene in a given area. However, soils form over long time periods, so I do not think that tight time constraints are possible. This causes difficulties in temporal comparison between the paleoclimatic signals obtained from the soil carbonate and the paleoclimatic cycles previously established for Quaternary.

REFERENCES

Allison, G. B. (1982). The relationship between ^{18}O and deuterium in water in sand columns undergoing evaporation. *Journal of Hydrology.* 55, 163-169.

Allison, G. B. (1988). A review of some of the physical, chemical and isotopic techniques available for estimating groundwater recharge. *In* "Estimation of Natural Groundwater Recharge." (I. Simmers, Ed.), pp. 49-72, Reidel, Dordrecht.

Allison, G. B., and Barnes, C. J. (1983). Estimation of evaporation from non-vegetated surfaces using natural deuterium. *Nature*, 301(13), 143-145.

Allison, G. B., Barnes, C. J., and Hughes, M. W. (1983). The distribution of deuterium and ^{18}O in dry soils 2. Experimental. *Journal of Hydrology* 64, 377-397.

Amundson, R. D., Chadwick, O. A., Sowers, J. M., and Doner, H. E. (1988). Relationship between climate and vegetation and the stable carbon isotope chemistry of soils in the Eastern Mojave Desert, Nevada. *Quaternary Research* 29, 245-254.

Barnes, C. J., and Allison, G. B. (1982). Interpretation of stable isotope profiles in arid zone dunes. *Hydrology and Water Resource Symposium*, IEA, Melbourne, 98-101.

Barnes, C. J., and Allison, G. B. (1983). The distribution of deuterium and ^{18}O in dry soils 1. Theory. *Journal of Hydrology* 60, 141-156.

Barnes, C. J., and Allison, G. B. (1988). Tracing of water movement in the unsaturated zone using stable isotopes of hydrogen and oxygen. *Journal of Hydrology* 100, 143-176.

Barnes, C. J., Allison, G. B., and Hughes, M. W. (1989). Temperature gradient effects on stable isotope and chloride profiles in dry soils. *Journal of Hydrology* 112, 69-87.

Bentley, H. W., and Davis, S. N. (1982). Application of AMS to hydrology, *In* "2nd Annual Symposium on Acceleration Mass Spectrometry." (M. Kutchera, Ed.), Argonne National Laboratories.

Bentley, H. W., Phillips, F. M., and Davis, S. N. (1986). Chlorine-36 in the terrestrial environment, *In* "Handbook of Environmental Isotope Geochemistry, Volume 2, The Terrestrial Environment, B." (P. Fritz, and J. Ch. Fontes, Eds.), pp. 427-480, Elsevier, Amsterdam.

Birkeland, P. W. (1984). "Soils and Geomorphology." Oxford University Press, New York.

Briot, P. (1968). "The cycle of erosion in different climates." Translated by C. I. Jackson and K. M. Clayton, from *Le Cycle d'erosion sous les differents climatats*, University of California Press, Berkeley.

Broecker, W. S., and Oversby, V. W.. (1979). Chemical equilibria in the earth. *In* "Distribution of trace isotopes between coexisting phases." pp 150-170, McGraw Hill Co., New york.

Brown, L. (1984). Applications of accelerator mass spectrometry. *Annual Review*

of Earth and Planetary Sciences 12, 39-59.

Brown, E. T., Brook, E. J., Raisbeck, G. M., Yiou, F., and Kurz., M. D. (1992). Effective attenuation lengths of cosmic rays producing ^{10}Be and ^{26}Al in Quartz: implications for exposure age dating. *Geophysical Research Letters* 19, 369-372.

Bryan, K. (1922). Erosion and sedimentation in the Papago Country, Arizona, with a sketch of the geology. *U.S. Geological Survey Bulletins* 730, 19-90.

Bull, W. B. (1984). Alluvial fans and pediments of southern Arizona. *In* "landscapes of Arizona, the Geological Story." (T. L. Smiley, J. D. Nations, T. L. Pewe, and J. P. Schafer, Eds.), 229-252, University press of America, Lanham.

Cerling, T. E. (1984). The stable isotopic composition of modern soil carbonate and its relationship to climate. *Earth and Planetary Science Letters* 71, 229-240.

Cerling, T. E. (1990). Dating geomorphic surfaces using cosmogenic He-3. *Quaternary Research* 33, 148-156.

Cerling, T. E., Quade, J., Ambrose, S. H., and Sikes, N. E. (1991a). Fossil soils, grasses, and carbon isotopes from Fort Ternan, Kenya: grassland or woodland?. *Journal of Human Evolution.* 21, 295-306.

Cerling, T. E., Solomon, D. K., Quade, J., and Bowman, J. R. (1991b). On the isotopic composition of carbon in soil carbon dioxide. *Geochimica et Cosmochimica Acta* 55, 3403-3405.

Cole, D. R., and Monger, H. C. (1994). Inflence of atmospheric CO_2 on the decline of C_4 plants during the last deglaciation. *Nature* 368, 533-536.

Coleman, M. L., Shepherd, T. J., Durham, J. J., Rouse, J. E., and Moore, G. R.

(1982). Reduction of water with zinc for hydrogen isotope analysis. *Analytical Chemistry*, 54, 993-995.

Conway, M., and Liston, L. L. (Eds.) (1990), "The Weather Handbook". pp 78-79, Conway Data Inc., Norcross.

Cook, P. G., Edmunds, W. M., and Gaye, C. B. (1992). Estimating paleorecharge and paleo-climate from unsaturated zone profiles. *Water Resources Research* 28(10), 2721-2731.

Cooke, R. U., and Warren, A. (1973). "Geomorphology in Deserts." University of California Press, Berkeley and Los Angeles.

Craig, H. (1953). The geochemistry of the stable carbon isotopes. *Geochimica et Cosmochimica Acta* 3, 53-92

Craig, H. (1961). Isotopic variations in meteoric water. *Science*, 133, 1702-1703.

Craig, H., and Gordon, L. (1965). Deuterium and oxygen-18 variations in the ocean and marine atmosphere. *In* "Stable Isotopes in Oceanographic Studies and Paleotemperatures." (E. Tongiorgi, Ed.), Lab. Geol. Nucl. Pasa, pp 9-130.

Dansgaard, W. (1964). Stable isotopes in precipitation. *Tellus*, XVI, 436-468.

Deines, P., Langmuir, D., and Harmon, R. S. (1974). Stable carbon isotope ratios and the existence of a gas phase in the evolution of carbonate ground water. *Geochimica et Cosmochimica Acta* 38, 1147-1164.

Denny, C. S. (1967). Fans and pediments. *American Journal of Science* 265, 81-105.

Dodge, N. N. (1964). "Organ Pipe Cactus National Monument, Arizona." History handbook Series, No. 6, p8, Department of Interior, 91.

Dohrenwend, J. C. (1987). Basin and Range. *In* "Geomorphic Systems of North America, Centennial Special Volume 2." (G. L. William, Ed.), pp. 303-342. The Geological Society of America, Inc., Boulder.

Dunbier, R. (1970). "The Sonoran Desert." The University of Arizona Press, Tucson.

Edge, R. D. (1959). The altitude dependence of atmospheric cosmic-ray neutrons and the slow neutron density below a water surface. *Nuclear Physics* 12, 182-189.

Elmore, D., and Phillips, F. M. (1987). Accelerator mass spectrometry for measurements of long-lived radioisotopes. *Science* 236, 543-550.

Fabryka-Martin, J. (1988). "Production of Radionuclides in the Earth and Their Hydrologic Significant, With Emphasis on Chlorine-36 and Iodine-129." the Unpublished Ph.D. Dissertation, The University of Arizona, Tucson.

Fairbridge, R. W. (1968). Terraces, fluvial-environmental controls. *In* "Encyclopedia of Geomorphology." (R. W. Fairbridge, Ed.), pp 1124-1138. Reinhold Brook Corporation, New York.

Farquhar, F. D., O'Leary, M. H., and Berry, J. A. (1982) On the relationship between carbon isotope discrimination and intercellular carbon dioxide concentration in leaves. *Australian Journal of Plant Physiology* 9, 121-137.

Friedman, I., and O'Neil, J. R. (1977). Compilation of stable isotope fractionation factors of geochemical interest. *In* "Data of Geochemistry." (M. Fleischer, Ed.), U. S. Geological Survey Professional Paper, 440-kk (6th ed.).

Gardner, L. R. (1984). Carbon and oxygen isotope composition of pedogenic $CaCO_3$ from soil profiles in Nevada and New Mexico, U.S.A.. *Isotope Geoscience* 2, 55-73.

Gile, L. H., Peterson, F. F., and Grossman, R. B. (1966). Morphological and genetic sequences of carbonate accumulation in desert soils. *Soil Science* 101, 347-360.

Gile, L. H., Hawley, J. W., and Grossman, R. B (1981). "Soils and Geomorphology in the Basin and Range Area of Southern New Mexico - Guidebook to the Desert Project." Memoir 39, New Mexico Bureau of Mines and Mineral Resources, Socorro.

Glasstone, S. (1955). "Principles of Nuclear Reactor Engineering." D. Van Nostrand, New York.

Harden, D. R., Biggar, N. E., and Gillam, M. L. (1985). Quaternary deposits and soils in and around Spanish Valley, Utah. *In* "Soils and Quaternary Geology of the Southwestern United States, Special Paper 203" (D. L. Weide, Ed.), pp 43-64. The Geological Society of America, Boulder.

Harris, D. V., and Kiver, E. P. (1985). "The Geological Story of the National Parks and Monuments." John Wiley, New York.

Hendricks, D. M. (1985). "Arizona Soils." The University of Arizona, Tucson.

Hillel, D. (1971). "Soil and Water: Physical Principles and Processes." Academic Press, New York.

Hooke, R. LeB. (1968). Steady-state relationships on arid-region alluvial fans in

closed basins. *American Journal of Science* 266, 609-629.

Jannik, N. O. (1989). "Lake History in the Paleo-Owens River System, CA for the Past 2.0 myr Based on ^{36}Cl Dating of Evaporites From Searles Lake." the Unpublished Ph.D. Dissertation, New Mexico Institute of Mining and Technology, Socorro.

Jenny, H. (1941). "Factors of Soil Formation." McGraw-Hill, New York.

Jull, A. J. T., Donahue, D. J., and Linick, T. W. (1989). Spallogenic C-14 in high-altitude rocks and in Antarctic meteorites. *Radiocarbon* 31, 719-724.

Kendall, C., and Coplen, T. B. (1985). Multisample conversion of water to hydrogen by zinc for stable isotope determination, *Analytical Chemistry* 57, 1437-1440.

Kimball, B. A., Jackson, R. D., Reginato, R. J., Nakayama, F. S., and Idso, S. B. (1976). Comparison of field-measured and calculated soil-heat fluxes. *Soil Science Society of America Journal*, 40(1), 18-25.

Klein, J., Giegengack, R., Middleton, R., Sharma, P., Underwood, J. R., J., and Weeks, R. A. (1986). Revealing histories of exposure using in situ produced Al-26 and Be-10 in Libyan Desert Glass. *Radiocarbon* 28(2A), 547-555.

Knowlton, R. G. Jr. (1990). "A Stable Isotope Study of Water and Chloride Movement in Natural Desert Soils." the Unpublished Ph.D. Dissertation, New Mexico Institute of Mining and Technology, Socorro.

Knowlton, R. G. Jr., Phillips, F. M., and Campbell, A. R. (1989). A stable-isotope investigation of vapor transport during ground-water recharge in New Mexico.

WRRI Report No. 237, New Mexico Resources Research Institute, Las Cruces.

Kodama, M., Kudo, S., and Kosuge, T. (1985). Application of atmospheric neutrons to soil moisture measurement. *Soil Science* 140, 237-242.

Kurz, M. D. (1986). Cosmogenic helium in a terrestrial igneous rock. *Nature* 320, 435-439.

Kurz, M. D., Colodner, D., Trull, T. W., Moore, R. B., and O'Brien, K. (1990). Cosmic ray exposure dating with in situ produced cosmogenic ^{3}He: Results from young Hawaiian lava flows. *Earth and Planetary Science Letters* 97, 177-189.

Lal., D, and Peter, B. (1967). Cosmic-ray produced radioactivity on earth. *In* "Handbook of Physics." (S. Fluegge, Ed.), 46/2, pp 551-612, Springer, Berlin.

Lal, D. (1988). In situ-produced cosmogenic isotopes in terrestrial rocks. *Annual Review of Earth and Planetary Sciences* 16, 355-388.

Lal, D. (1991). Cosmic ray labeling of erosion surfaces: *in situ* nuclide production rates and erosion models. *Earth and Planetary Science Letters* 104, 424-439.

Leavy, B. D., Phillips, F. M., Elmore, D., Kubik, P. W., and Gladney, E (1987). Measurement of cosmogenic ^{36}Cl/Cl in young volcanic rocks: an application of accelerator mass spectrometry in geochronology. *Nuclear Instruments and Methods in Physics Research* B29, 246-250.

List, R. J. (Ed.) (1963). "Smithsonian Meteorological Tables." Volume 114, pp 382-383, Smithsonian Institution, City of Washington.

Liu, B., Phillips, F. M., Fabryka-Martin, J. T., Fowler, M. M., and Biddle, R. S.

(1994a). Cosmogenic ^{36}Cl accumulation in unstable landforms, I. Effects of the thermal neutron distribution. *Water Resources Research* (in press).

Liu, B., Phillips, F. M., Hoines, S., and Sharma, P. (1994b). An alluvial surface chronology based on cosmogenic ^{36}Cl dating, Ajo Mountains, Organ Pipe Cactus National Monument, south-central Arizona. in preparation for *Quaternary Research*.

Lustig, L. K. (1966). The geomorphic and paleoclimatic significance of alluvial deposits in southern Arizona. *Journal of Geology* 74, 95-102.

Mabbutt, J. A. (1966). Mantle-controlled planation of pediments. *American Journal of Science* 264, 78-91.

Machette, M. N. (1985). Calcic soils of the southwestern United States. *In* "Soils and Quaternary Geology of the Southwestern United States, Special Paper 203" (D. L. Weide, Ed.), pp 1-21. The Geological Society of America, Boulder.

Manahan, S. E. (1991). "Environmental Chemistry." 5th edition, p 220, Lewis Publishers, Chelsea.

Marino, B. D., McElroy, M. B., Salawitch, R. J., and Spaulding, W. G. (1992). Glacial-to-interglacial variation in the carbon isotopic composition of atmospheric CO_2. *Nature* 357, 461-466.

Marion, G. M., Introne, D. S., and Van Cleve, K. (1991). The stable isotope geochemistry of $CaCO_3$ on the Tanana River floodplain of interior Alaska, U.S.A.: Composition and mechanism of formation. *Chemical Geology (Isotope Geoscience Section)* 86, 97-110.

Mattick, J. L., Duval, T. A., and Phillips, F. M. (1987). Quantification of groundwater recharge rates in New Mexico using bomb ^{36}Cl, bomb-^{3}H and chloride as soil water tracers. *WRRI Report No. 220*, New Mexico Resources Research Institute, Las Cruces.

McFadden, L. D., and Tinsley, J. C. (1985). Rate and depth of pedogenic-carbonate accumulation in soils: Formation and testing of a compartment model. *In* "Soils and Quaternary Geology of the Southwestern United States, Special Paper 203" (D. L. Weide, Ed.), pp 23-41. The Geological Society of America, Boulder.

McFadden, L. D., Amundson, R. G., and Chadwick, O. A. (1991). Numerical modeling, chemical, and isotopic studies of carbonate accumulation in soils of arid regions. *In* " Occurrence, Characteristics, and Genesis of Carbonate, Gypsum, and Silica Accumulations in Soils", Soil Science Society of America Special Publication No. 26.

McGee, W. J. (1897). Sheetflood erosion. *Geological Society of America Bulletin* 8, 87-112.

Montgomery, E. L., and Harshbarger, J. W. (1989). Arizona hydrogeology and water supply. *In* "Geologic Evolution of Arizona" (J. P. Henney, and S. J. Reynolds Eds.), pp. 827-840. Arizona Geological Sociaty Digest, 17, Tucson.

Morrison, R. B. (1991a). Quaternary geology of the southern Basin and Range province. *In* "Quaternary Nonglacial Geology: Conterminous U.S." (R. B. Morrison, Ed.), pp 353-371. The Geological Society of America, Boulder.

Morrison, R. B. (1991b). Quaternary stratigraphic, hydrologic, and climatic history

of the Great Basin, with emphasis on Lakes Lahontan, Bonneville, and Tecopa. *In* "Quaternary Nonglacial Geology: Conterminous U.S." (R. B. Morrison, Ed.), pp 283-320. The Geological Society of America, Boulder.

National Atmospheric Deposition Program (NRSP-3)/National Trends Network (1993). NADP/NTN Coordination Office, Natural Ecology Laboratory, Colorado State University, Fort Collins.

Nishiizumi, K., Lal, D., Klein, J., Middleton, R., and Arnold, J. R. (1986). Production of ^{10}Be and ^{26}Al by cosmic rays in terrestrial quartz in situ and implications for erosion rates. *Nature* 319, 134-136.

Nishiizumi, K., Winterer, E. L., Kohl, C. P., Klein, J., Middleton, R., Lal, D., and Arnold, J. R. (1989). Cosmogenic ray production rates of ^{10}Be and ^{26}Al in quartz from glacially polished rocks. *Journal of Geophysical Research* 94(B12), 17907-17915.

Nishiizumi, K., Kohl, C. P., Arnold, J. R., Klein, J., Fink, D., and Middleton, R. (1991). Cosmogenic ray produced ^{10}Be and ^{26}Al in Antarctic rocks: exposure and erosion history. *Earth and Planetary Science Letters* 104, 440-454.

Oberlander, T. M. (1989). Slope and pediment systems. *In* "Arid Zone Geomorphology" (D. S. G. Thomas, Ed.), pp 56-84, Belhaven Press, London.

O'Brien, K., Sandmeier, H. A., Hansen, G. E., and Campbell, J. E. (1978). Cosmic ray induced neutron background sources and fluxes for geometries of air over water, ground, iron, and aluminum. *Journal of Geophysical Research* 83, 114-120.

Olinger, C. T., Poths, J., Nishiizumi, K., Kohl, C. P., Finkel, R. C., Cattee, M. W., Southon, J., and Proctor, I. (1992). Attenuation lengths of cosmogenic production of ^{26}Al, ^{10}Be and ^{21}Ne in Bandelier Tuff. *Eos* 73/14, 185.

O'Neil, J. R., Clayton, R. N., and Mayeda, T. K. (1969). Oxygen isotope fractionation in divalent metal carbonates. *The Journal of Chemical Physics* 51, 5547-5558.

Paige, S. (1912). Rock-sut surfaces in the desert ranges. *Journal of Geology* 20, 442-450.

Parada, C B., Long, A., and Davis, S. N. (1983). Stable-isotopic composition of soil carbon dioxide in the Tucson Basin, Arizona, U.S.A.. *Isotope Geoscience* 1, 219-236.

Phillips, F. M., Leavy, B. D., Jannik, N. O., Elmore, D., and Kubik, P. W. (1986), The accumulation of cosmogenic chlorine-36 in rocks: a method for surface exposure dating. *Science* 231, 41-43.

Phillips, F. M., Mattick, J. L., Duval, T. A., Elmore, D., and Kubik, P. W. (1988). Chlorine-36 and tritium from nuclear weapons fallout as tracers for long-term liquid and vapor movement in desert soil. *Water Resources Research*, 24, 1877-1891.

Phillips, F. M., Zreda, M. G., Smith, S. S., Elmore, D., Kubik, P. W., and Sharma, P. (1990). Cosmogenic chlorine-36 chronology for glacial deposits at Bloody Canyon, eastern Sierra Nevada. *Science* 248, 1529-1532.

Phillips, F. M., Zreda, M. G., Smith, S. S., Elmore, D., Kubik, P. W., Dorn, R. I.,

and Roddy, D. J. (1991). Age and geomorphic history of Meteor Crater, Arizona from cosmogenic ^{36}Cl and ^{14}C in rock varnish. *Geochimica et Cosmochimica Acta* 55, 2695-2698.

Quade, J., Cerling, T. E., and Bowman, J. R. (1989). Systematic variations in the carbon and oxygen isotopic composition of pedogenic carbonate along elevation transects in the southern Great Basin, United States. *Geological Society of America Bulletin* 101, 464-475.

Quade, J., and Cerling, T. E. (1990). Stable isotopic evidence for a pedogenic origin of carbonates in Trench 14 near Yucca Mountain, Nevada. *Science* 250, 1549-1552.

Rabenhorst, M. C., Wilding, L. P., and West, L. T. (1984). Identification of pedogenic carbonates using stable carbon isotope. *Soil Science Society of America Journal* 48, 125-132.

Ritter, D. F. (1979). "Process Geomorphology." Wm. C. Brown, Dubuque.

Saxena, R. K., and Dressie, Z. (1984). Estimation of groundwater recharge and moisture movement in sandy formations by tracing natural oxygen-18 and injected tritium profiles in the unsaturated zone. *In* "Isotope Hydrology 1983, Proc. Symp.", pp 139-150, IAEA, Vienna.

Scanlon, B. R. (1992). Evaluation of liquid and vapor water flow in desert soils based on chlorine-36 and tritium tracers and nonisothermal flow simulations. *Water Resources Research*, 28(1), 285-297.

Shafiqullah, M., Damon, P. E., Lynch, D. J., Reynolds, S. J., Rehrig, W. A., and

Raymond, R. H. (1980). K-Ar geochronology and geologic history of southwestern Arizona and adjacent area. *In* "Studies in Western Arizona" (J. P. Jenney, and C. Stone, Eds.), pp. 201-260. Arizona Geological Society Digest, 12, Tucson.

Sharma, M. L., and Hughes, M. W. (1985). Groundwater recharge estimation using chloride, deuterium and oxygen-18 profiles in the deep coastal sands of Western Australia. *Journal of Hydrology*, 81, 93-109.

Simpson, D. T. (1991). "Soil and geomorphology of the Quaternary alluvial sequences on the western piedmont of the Ajo Mountains, Organ Pipe Cactus National Monument, Pima County, Arizona." the Unpublished M.S. thesis, University of New Mexico.

Smith, G. A., Wang, Y. Cerling, T. E., and Geissman, J. W. (1993). Comparison of a paleosol-carbonate isotope record to other records of Pliocene-early Pleistocene climate in the western United States. *Geology* 21, 691-694.

Socki, R. A., Karlsson, H. R., and Gibson, E. K. Jr. (1992). Extraction technique for the determination of oxygen-18 in water using pre-evacuated glass vials. *Analytical Chemistry*, 64, 829-831.

Stephenson, R. M. (1954). "Introduction to Nuclear Engineering". pp. 134-135, McGraw-Hill Book Company, New York.

Stone, W. J. (1984). Research in the Salt Lake coal field based on chloride in the unsaturated zone. *New Mexico Bureau of Mines and Mineral Resources Open-File Report* No. 214.

Stumm, W., and Morgan, J. J. (1981). "Aquatic Chemistry". p. 255. John Willey & Sons, New York.

Teeri, J. A., and Stowe, L. G. (1976). Climate patterns and the distribution of C_4 grasses in North America. *Oecologia* 23, 1-12.

Tuan, Yi-Fu (1959). "Pediments in southeastern Arizona." University of California Publications in Geography, 13.

Twidale, C. R. (1983). Pediments, peneplains and ultiplains. *Review of Geomorphologic Dynamics* 32, 1-35.

Van Devender, T. R. (1987). Holocene vegetation and climate in the Puerto Blanco Mountains, southwestern Arizona. *Quaternary Research* 27, 51-72.

Vogel, J. C. (1978). Recycling of carbon in a forest environment. *Oecologia Plantarum* 13, 89-94.

Yamashita, M., Stephens, L. D., and Patterson, H. W. (1966). *Journal of Geophysical Research* 71, 3817-3834.

Zimmermann, U., Munnick, K-O, and Roether, W. (1967). Downward movement of soil moisture traced by means of hydrogen isotopes. *In* "Isotope Techniques in the Hydrological Cycle, Geophysical Monograph No. 11." (G. E. Stout, Ed.), pp 28-35, American Geophysical Union, Washington D. C..

Zreda, M. G. (1994). " Development and Calibration of the Cosmogenic ^{36}Cl Method and its Applications to the Chronology of Late Quaternary Glaciations." Unpublished Ph.D. Dissertation, New Mexico Institute of Mining and Technology, Socorro.

Zreda, M. G., Phillips, F. M., Elmore, D., Kubik, P. W., Sharma, P., and Dorn, R. I. (1991). Cosmogenic chlorine-36 production rates in terrestrial rocks. *Earth and Planetary Science Letters* 105, 94-109.

Zreda, M. G., Phillips, F. M., Kubik, P. W., Sharma, P., and Elmore, D. (1993). Cosmogenic ^{36}Cl dating of a young basaltic eruption complex, Lathrop Wells, Nevada. *Geology* 21, 57-60.

Zreda, M. G., Phillips, F. M., Elmore, D.(1994). Cosmogenic ^{36}Cl accumulation in unstable landforms II. Monte Carlo simulations and experimental observations on eroding glacial moraines. *Water Resources Research* (in press).

Appendix 1 Field photographs of sampled boulders

Appendix 2 Procedure for Extracting Cl for $^{36}Cl/Cl$ Analysis

Samples are supposed to have been prepared by grading and leaching (see Zreda, 1994 for details) and are ready for chemically extracting Cl.

- Weigh appropriate amount of sample. The amount of sample depends on Cl concentration in a sample. The rule of thumb is to have at least total amount of 3 mg Cl mass in a sample being processed.
- Put the sample in a 1000-ml teflon bottle. Add concentrated HNO_3 (70%) in proportion 1 part of HNO_3 to 1 part of sample.
- Add HF (48%) slowly in proportion 2.5 parts of HF to 1 part of sample.
- Immediately close the bottle (not very tight) and leave it under the hood until it cools down.
- Put it in a hot bath at about 80 °C and keep it in until the sample is completely dissolved. This usually takes more than 24 hours.
- After complete dissolution, transfer the sample into a 250-ml teflon centrifuge bottle.
- When the sample cools to room temperature, centrifuge for 10 minutes.
- Decant the solution into a 500-ml teflon beaker and add 10 ml of 0.1 M $AgNO_3$ solution.
- Place the beaker on a hot plate at 60 °C to flocculate AgCl and to evaporate excess solution.

- When significant AgCl precipitate occurs (usually rosy gray color), transfer the whole solution into a 50-ml teflon centrifuge tube, and immediately centrifuge for 10 minutes at.
- Carefully decant the solution and keep the precipitate which is AgCl.
- Add deionized water and mix well with the precipitate.
- Add NH_4OH to dissolve AgCl, then centrifuge to separate any silica present.
- Transfer the solution in a 50-ml glass centrifuge tube. And HNO_3 to precipitate AgCl again.
- Dissolve the AgCl in 3 ml of NH_4OH and add 1.5 ml of $Ba(NO_3)_2$ to precipitate $BaSO_4$. Leave the solution for at least 8 hours (but preferably longer).
- Centrifuge the glass centrifuge tube for 10 minutes.
- Carefully transfer the supernatant into another clean glass centrifuge tube.
- If sample size is sufficient, repeat the last 4 steps one more time.
- Add small amount of HNO_3 to precipitate AgCl, then centrifuge the glass tube to separate the AgCl precipitate from the acidic solution.
- Remove acidic solution and rinse the AgCl 3 times in deionized water. Make sure the pH of the final rinse is about 7.
- Transfer the AgCl onto a clean watch glass. Remove excess water using small glass pipette. Cover the watch glass with aluminum foil.
- Place the sample in the oven at about 60 °C for 24 hours. The AgCl is ready to load into the sample holder for ^{36}Cl analysis.

Appendix 3.1 Chemical Compositions of Boulders on Qt2

Sample #	OP90-7	OP90-8	OP90-9	OP90-10	OP91-3	OP91-4	OP91-5	S5 #1
Rock	T-And	Rhy	T-And	Rhy	Tra	T-And	Rhy	Tra
Site #	2	2	2	2	5	5	5	7
(%)								
SiO2	58.50	72.58	57.96	77.66	63.50	59.93	73.33	68.20
TiO2	1.41	0.30	1.55	0.27	0.93	1.60	0.23	0.64
Al2O3	18.04	14.63	16.99	13.01	16.17	16.20	13.93	14.70
Fe2O3	7.10	2.70	7.91	2.12	5.54	8.25	2.13	3.46
MnO	0.09	0.06	0.10	0.05	0.10	0.11	0.05	0.07
MgO	2.23	0.56	2.19	0.85	1.37	1.66	0.57	0.63
CaO	3.99	1.37	4.29	1.08	2.70	3.09	1.05	1.74
Na2O	4.09	4.41	4.02	3.18	3.96	4.30	3.73	3.63
K2O	4.12	4.71	4.18	4.72	3.66	4.51	5.00	4.56
P2O5	0.32	0.06	0.31	0.06	0.24	0.51	0.07	0.14
%LOI	1.86	1.22	1.44	0.97	2.63	1.73	1.24	2.70
Total	101.74	102.58	100.93	103.97	100.78	101.88	101.33	100.50
(ppm)								
Cl	44.6	33.4	58.8	50.2	121	72.8	341	36.8
B	13.0	12.0	15.0	3.4	11.0	20.0	12.0	9.0
Gd	7.5	3.2	8.6	3.5	4.7	10.9	4.2	3.9

Appendix 3.2 Chemical Compositions of Boulders on Qt1 and Qf2

Sample #	OP392-2	OP392-3	OP1092-5	OP91-1	OP91-2	OP392-4	OP1092-3	S3 #1
Rock	Tra	Tra	Tra	Rhy	Tra	T-And	Rhy	Rhy
Unit	Qt1	Qt1	Qt1	Qf2	Qf2	Qf2	Qf2	Qf2
Site #	9	9	2	4	4	10	13	8
(%)								
SiO2	63.40	66.30	62.60	75.49	63.27	57.80	75.90	71.50
TiO2	0.80	0.70	1.01	0.13	0.93	1.52	0.14	0.37
Al2O3	15.60	15.30	15.80	11.84	16.09	15.90	11.40	14.10
Fe2O3	4.25	3.68	5.09	1.82	5.70	7.64	1.17	2.51
MnO	0.07	0.06	0.09	0.09	0.08	0.18	0.05	0.06
MgO	1.18	0.74	1.22	1.22	2.62	1.30	0.22	0.35
CaO	3.56	2.41	3.21	1.62	3.72	3.80	0.79	1.05
Na2O	4.10	4.20	4.31	2.38	4.26	3.80	2.70	3.73
K2O	3.29	4.18	3.37	6.23	3.35	4.21	4.51	4.49
P2O5	0.24	0.17	0.09	0.19	0.29	0.72	0.04	0.10
%LOI	1.80	1.85	1.10	2.16	1.88	1.60	1.25	2.00
Total	98.60	99.90	97.90	103.16	102.19	98.50	98.20	100.30
(ppm)								
Cl	84.1	79.1	49.8	59.6	86.4	63.9	36.8	42.2
B	8.0	10.7	3.0	10.0	7.6	22.3	2.9	7.7
Gd	6.0	5.2	1.9	3.7	5.4	13.3	4.9	4.7

Appendix 3.3 Chemical Compositions of Boulders on Qf1

Sample #	OP90-1	OP90-2	OP90-3	OP90-5	OP90-11	OP90-12	OP90-13	OP91-6	OP91-7	CP #2
Rock	Rhy	Rhy	Rhy	Tra	Rhy	Tra	T-And	Tra	Rhy	5 cm
Site #	1	1	1	1	3	3	3	6	6	6
(%)										
SiO2	72.51	69.21	75.87	59.18	74.09	64.30	62.07	64.05	70.02	67.30
TiO2	0.27	0.36	0.14	1.54	0.13	0.93	0.72	0.94	0.20	0.59
Al2O3	13.21	14.58	12.67	15.68	11.08	16.06	15.24	16.12	12.62	13.20
Fe2O3	2.23	2.69	1.65	7.45	1.46	5.70	4.38	5.69	1.99	3.55
MnO	0.05	0.06	0.04	0.12	0.05	0.07	0.05	0.10	0.06	0.07
MgO	0.58	0.71	0.46	1.91	1.12	1.49	1.71	2.38	1.26	1.29
CaO	2.21	1.56	1.23	3.18	2.19	3.40	2.76	3.29	3.68	3.09
Na2O	5.73	4.05	3.11	6.39	2.66	4.35	3.85	4.20	3.57	2.30
K2O	2.03	4.28	5.31	4.63	5.27	3.60	3.60	3.48	4.55	3.66
P2O5	0.06	0.07	0.05	0.35	0.08	0.23	0.15	0.31	0.14	0.16
%LOI	5.12	3.11	1.30	1.57	3.01	1.49	2.22	1.95	3.67	4.95
Total	103.92	100.67	101.82	102.01	101.14	101.63	96.74	102.50	101.77	100.40
(ppm)										
Cl	57.4	1226	55.5	53.1	35.7	110	55.1	71.6	36.5	49.3
B	22	14	6.0	20.0	19.0	8.6	7.1	8.4	9.6	22.3
Gd	3.1	4.9	3.8	10.0	3.4	5.9	7.1	7.3	3.9	6.9

Appendix 3.4 Chemical Compositions for Channel and Bedrock

Sample #	OP392-5	OP392-12	OP392-13	OP1092-1	OP1092-2	OP392-10
Rock	Tra	T-And	T-And	T-And	T-And	T-And
Unit	Qfc	Deb.	Deb.	Deb.	Deb.	Bedrock
Site #	11	11	11	11	11	12
(%)						
SiO2	67.90	58.80	56.40	58.80	58.80	54.50
TiO2	0.36	1.23	1.39	1.62	1.54	1.80
Al2O3	14.40	17.20	17.90	18.40	18.60	15.90
Fe2O3	2.48	5.94	6.65	6.70	6.29	8.78
MnO	0.07	0.08	0.16	0.10	0.10	0.14
MgO	0.56	1.27	1.18	0.67	1.09	2.70
CaO	1.43	4.75	4.29	3.93	4.19	4.81
Na2O	4.63	3.93	3.95	4.28	4.30	3.42
K2O	4.32	3.85	3.72	3.82	3.59	3.33
P2O5	0.08	0.42	0.54	0.07	0.07	0.49
%LOI	2.80	2.45	2.00	1.10	0.85	3.00
Total	99.30	100.30	98.20	99.50	99.40	99.20
(ppm)						
Cl	36.3	38.6	46.3	54.7	65.6	49.4
B	5.6	12.2	13.3	13.3	11.5	7.9
Gd	4.7	8.8	12.0	5.8	5.8	8.8

Appendix 3.5 Chemical Compositions for Cobble Profile on Qt2 (Site #2)

Sample#	BD 6cm	BD 28cm	BD 50cm	BD 86cm	BD 114cm
Rock	T-And	T-And	Tra	Rhy	Rhy
D (cm)	6	28	50	86	114
(%)					
SiO2	59.10	58.50	68.80	77.90	69.30
TiO2	1.29	1.48	0.36	0.25	0.35
Al2O3	17.20	18.50	14.30	9.99	14.60
Fe2O3	5.29	5.94	2.53	1.77	2.56
MnO	0.09	0.11	0.04	0.04	0.06
MgO	0.81	0.74	0.56	0.17	0.51
CaO	3.79	4.45	1.32	1.15	1.29
Na2O	4.30	4.24	4.22	2.38	4.24
K2O	4.06	3.46	4.26	4.02	4.41
P2O5	0.25	0.35	0.08	0.06	0.06
LOI	1.75	2.31	2.65	0.85	2.20
Total	98.30	100.40	99.40	98.80	99.90
Cl(ppm)	46.0	41.7	32.2	10.4	15.1
B(ppm)	19.2	14.9	8.9	5.9	6.5
Gd(ppm)	6.4	9.3	4.9	3.9	4.0

Note: T-And=Trachyte andesite, Rhy=Rhyolite, Tra=Trachyte.

Appendix 4. Procedure for Preparing Petrocalcic Samples

- Crush bulk petrocalcic samples into sizes less than 1 cm by rock chewer.
- Subdivide each crashed sample into two aliquots. Keep one as spare.
- Grand one aliquot sample into sizes less than 30 meshes.

Note: Sample should be sealed in plastic bags immediately after finishing each step to minimize moisture losing.

- Weigh 200 g of sample, put in a glass beaker, and dry in an oven at 105 °C for at least 24 hours.
- Weigh the sample again when it cools down to room temperature after taking our of oven. The difference between the two weights before and after drying will give information of gravimetric water content. Make sure seal the beaker after taking it out of the oven.
- Add 400 ml of deionized water. Stern thoroughly, then leave it for at least 24 hours in order to dissolve meteoric Cl into the water completely.
- Carefully decant the supernatant into a clean glass flask for determination of Cl concentration in the pore water of the petrocalcic sample. Avoid losing significant amount of solid particles.
- Rinse the sample in deionized water until there is no Cl (less than 1 mg/l) in the leachate.
- Dry the sample in the oven and weigh it again after drying. Usually the weight has little change.

- Dissolve carbonate fraction of the sample in about 15% HNO_3.
- Carefully transfer the acidic solution into a clean glass flask for extracting Cl for ^{36}Cl analysis. Avoid losing significant silicate residual.
- Rinse the residual in deionized water until the solution is neutral.
- Dry the residual in oven for 24 hours. Weigh the residual again after it cools down. This will provide information of the carbonate content in the petrocalcic sample.

Now the residual is ready for extracting Cl for $^{36}Cl/Cl$ analysis as described in Appendix 2.

Appendix 5.1 Chemical Compositions of Bulk Petrocalcic Samples on Qf1 (Site #6)

Sample #	0-4	8-10	12-16	17-19	21-24	25-28	31-34	35-38	47-51
D (cm)	5.1	22.9	36.2	45.7	57.2	67.3	82.6	92.7	124.5
(%)									
SiO2	67.30	56.90	43.80	43.20	46.40	43.90	39.10	28.60	55.50
TiO2	0.59	0.64	0.22	0.31	0.32	0.26	0.29	0.14	0.33
Al2O3	13.20	13.30	8.54	8.10	9.02	8.38	7.65	4.93	10.00
Fe2O3	3.55	4.52	1.59	2.05	2.09	1.80	1.86	1.05	2.19
MnO	0.07	0.06	0.04	0.03	0.04	0.05	0.03	0.03	0.04
MgO	1.29	2.11	0.93	1.34	1.26	1.37	1.50	2.20	1.61
CaO	3.09	7.06	21.50	22.40	19.50	21.10	24.50	32.50	12.60
Na2O	2.30	1.03	1.91	1.47	1.79	1.91	1.47	1.15	2.35
K2O	3.66	2.55	2.81	2.19	2.82	2.66	2.21	1.37	3.20
P2O5	0.14	0.08	0.12	0.13	0.13	0.09	0.12	0.08	0.11
LOI	4.95	11.30	18.90	19.80	17.20	18.20	21.50	27.20	12.10
Total	100.4	99.7	100.5	101.0	100.6	99.7	100.2	99.2	100.2
(%)									
H2O	3.0	7.8	2.5	1.3	1.3	1.6	2.0	1.7	7.0
CO2	1.7	3.5	16.9	17.6	15.3	16.6	19.2	25.5	8.6
(ppm)									
Cl(B)	49.3	196	660	130	547	1410	640	941	96.9
B	22.3	36.9	10.9	13.3	13.4	13.8	11.6	13.2	14.3
Gd	6.9	5.5	3.5	3.4	4.8	2.3	3.5	1.4	3.8

Appendix 5.2 Chemical Compositions of Silicate Residual (Site #6)

Sample #	0-4R	8-10R	12-16R	25-28R	35-38R	47-51R
D (cm)	5.1	22.9	36.2	67.3	92.7	124.5
(%)						
SiO2	69.91	65.76	72.66	69.41	72.03	73.15
TiO2	0.54	0.64	0.32	0.46	0.48	0.39
Al2O3	12.83	13.52	13.29	12.87	11.60	12.36
Fe2O3	3.27	4.31	2.48	2.87	2.81	2.41
MnO	0.05	0.05	0.06	0.06	0.06	0.06
MgO	0.73	1.41	0.37	1.01	0.62	0.26
CaO	1.16	0.87	1.02	1.22	1.49	1.25
Na2O	1.93	1.01	2.79	2.39	2.29	2.61
K2O	3.78	2.60	4.56	4.01	3.20	4.08
P2O5	0.07	0.07	0.05	0.04	0.04	0.05
LOI	3.88	7.69	2.45	3.81	4.81	2.89
Total	98.15	97.94	100.05	98.14	99.41	99.52

Appendix 6.1 Soil Water and Soil Cl for SP#1 and SP#1-1 (Site #5)

SP#1 (January 1991 on Qt2)						SP#1-1 (May 1991 on Qt2)			
Depth (cm)	H2O (w%)	Cl (mg/kg)	ΣH_2O (cm)	ΣCl (10^{-3} mg/cm^2)	Interval (cm)	Depth (cm)	H2O (w%)	ΣH2O (cm)	Interval (inch)
5	13.6	0.86 ±0.36	2.45	15.5	0- 10	5.1	1.5	0.27	0- 4
15	13.9	0.98 ±0.12	4.95	33.1	10- 20	15.2	2.5	0.74	4- 8
25	14.5	1.13 ±0.18	7.56	53.5	20- 30	25.4	3.0	1.28	8-12
35	14.4	1.42 ±0.13	10.15	79.0	30- 40	35.6	4.1	2.03	12-16
45	14.3	1.37 ±0.23	12.73	103.7	40- 50	45.7	4.2	2.81	16-20
55	13.4	1.54 ±0.34	15.14	131.4	50- 60	55.9	4.8	3.67	20-24
65	11.5	3.26 ±0.19	17.21	190.1	60- 70	66.0	3.6	4.32	24-28
75	3.6	1.30 ±0.06	17.86	213.5	70- 80	76.2	3.4	4.95	28-32
85	3.2	1.21 ±0.54	18.43	235.3	80- 90	86.4	3.8	5.65	32-36
95	3.2	1.57 ±0.31	19.01	263.5	90-100	96.5	3.5	6.28	36-40

Appendix 6.2 Soil Water and Soil Cl for SP#3 (Site #9)

(March 1992 on Qt2)

Depth (cm)	H2O (w%)	Cl (mg/kg)	ΣH_2O (cm)	ΣCl (10^{-3} mg/cm^2)	Interval (inch)
2.5	8.9	1.11 ±0.07	0.82	10.2	0- 2
7.6	11.8	0.95 ±0.06	1.90	18.9	2- 4
15.2	12.7	0.92 ±0.07	4.23	35.7	4- 8
25.4	13.4	0.64 ±0.02	6.69	47.4	8-12
35.6	13.1	0.81 ±0.13	9.08	62.2	12-16
45.7	12.7	0.82 ±0.12	11.39	77.2	16-20
55.9	12.6	0.78 ±0.02	13.69	91.5	20-24
66.0	11.8	1.33 ±0.02	15.85	115.8	24-28
76.2	10.3	1.86 ±0.08	17.73	149.8	28-32
86.4	8.3	1.33 ±0.01	19.24	174.2	32-36
96.5	6.0	1.22 ±0.14	20.34	196.5	36-40

Appendix 6.3 Soil Water and Soil Cl for SP#3-2 (Site #9)

(May 1992 on Qt2)

Depth (cm)	H2O (w%)	Cl (mg/kg)	ΣH_2O (cm)	ΣCl (10^{-3} mg/cm^2)	Interval (inch)
2.5	1.7	0.77 ±0.05	0.16	7.1	0- 2
7.6	3.4	0.60 ±0.01	0.47	12.6	2- 4
15.2	4.3	0.40 ±0.04	1.25	19.9	4- 8
25.4	5.0	0.46 ±0.04	2.16	28.3	8-12
35.6	5.3	0.40 ±0.04	3.12	35.6	12-16
45.7	4.9	0.88 ±0.04	4.02	51.7	16-20
55.9	5.2	0.33 ±0.02	4.97	57.7	20-24
66.0	5.0	0.40 ±0.09	5.89	65.1	24-28
76.2	4.7	0.77 ±0.24	6.74	79.1	28-32
86.4	4.2	1.33 ±0.26	7.51	103.5	32-36
96.5	4.5	1.69 ±0.05	8.34	134.4	36-40

Appendix 6.4 Soil Water and Soil Cl for SP#4 (Site #9)

(August 1992 on Qt2)

Depth (cm)	H2O (w%)	Cl (mg/kg)	ΣH_2O (cm)	ΣCl (10^{-3} mg/cm^2)	Interval (inch)
2.5	10.6	0.87 ±0.26	0.97	7.8	0- 2
7.6	11.8	0.99 ±0.11	2.05	17.1	2- 4
15.2	12.4	0.95 ±0.19	4.32	34.4	4- 8
25.4	12.0	1.15 ±0.09	6.51	55.5	8-12
35.6	8.1	0.79 ±0.05	7.98	69.9	12-16
45.7	4.0	0.64 ±0.08	8.71	81.6	16-20
55.9	4.2	0.99 ±0.09	9.48	99.7	20-24
66.0	4.3	3.28 ±0.06	10.26	159.7	24-28
76.2	4.2	3.46 ±0.02	11.03	223.0	28-32
86.4	4.1	5.08 ±0.38	11.78	315.9	32-36
96.5	3.4	7.49 ±0.13	12.39	452.9	36-40

Appendix 6.5 Soil Water and Soil Cl for SP#4-2 (Site #9)

(October 1992 on Qt2)

Depth (cm)	H2O (w%)	Cl (mg/kg)	ΣH_2O (cm)	ΣCl (10^{-3} mg/cm^2)	(Interval) (inch)
1.3	1.3	0.84 ±0.03	0.06	3.8	0- 1
3.8	1.7	1.58 ±0.12	0.14	11.0	1- 2
7.6	2.4	1.15 ±0.09	0.36	21.6	2- 4
15.2	3.2	0.91 ±0.03	0.95	38.2	4- 8
25.4	3.9	1.23 ±0.02	1.66	60.7	8-12
35.6	3.5	0.77 ±0.13	2.30	74.8	12-16
45.7	3.7	0.57 ±0.04	2.98	85.2	16-20
55.9	4.0	1.37 ±0.02	3.72	110.3	20-24
66.0	4.3	0.91 ±0.10	4.51	126.9	24-28
76.2	4.7	1.61 ±0.42	5.36	156.4	28-32
86.4	4.3	1.58 ±0.00	6.14	185.3	32-36
96.5	3.6	1.80 ±0.06	6.79	218.2	36-40

Appendix 6.6 Soil Water and Soil Cl for SP#2 (Site #10)

(March 1992 on Qf2)

Depth (cm)	H2O (w%)	Cl (mg/kg)	ΣH_2O (cm)	ΣCl (mg/cm^2)	Interval (inch)
1.3	9.9	2.5 ± 0.1	0.45	0.01	0- 1
6.4	14.6	2.7 ± 0.4	2.46	0.05	1- 4
15.2	11.3	2.8 ± 0.0	4.52	0.10	4- 8
25.4	11.3	10.6 ± 2.0	6.59	0.29	8-12
35.6	10.8	44.3 ±10.3	8.56	1.10	12-16
45.7	7.3	133.6 ± 9.2	9.90	3.55	16-20
55.9	7.4	165.2 ±20.5	11.25	6.57	20-24
66.0	7.2	253.8 ±42.3	12.57	11.21	24-28
76.2	5.0	403.3 ±45.4	13.48	18.59	28-32
86.4	7.5	479.9 ±72.9	14.85	27.36	32-36
96.5	6.2	544.8 ±15.7	15.99	37.32	36-40

Appendix 6.7 Soil Water and Soil Cl for SP#5 (Site #2)

(October 1992 on Qt1)

Depth (cm)	H2O (w%)	Cl (mg/kg)	ΣH_2O (cm)	ΣCl (mg/cm^2)	Interval (inch)
2.5	1.4	2.32 ± 0.03	0.12	0.02	0- 2
7.6	1.8	2.83 ± 0.05	0.29	0.05	2- 4
15.2	2.5	2.87 ± 0.41	0.76	0.10	4- 8
25.4	3.6	2.99 ± 0.04	1.41	0.15	8-12
35.6	4.3	13.24 ± 0.05	2.19	0.40	12-16
45.7	4.5	32.82 ± 5.99	3.01	1.00	16-20
55.9	4.8	71.90 ±17.76	3.89	2.31	20-24
66.0	5.0	99.77 ±15.51	4.80	4.14	24-28
76.2	4.8	209.93 ± 1.02	5.68	7.98	28-32
86.4	4.6	252.33 ± 1.01	6.53	12.59	32-36
96.5	4.9	355.65 ± 0.95	7.43	19.09	36-40

Appendix 7.1 O and H Isotopic Compositions in Soil Water (Site #5)

SP#1 (January 1991 on Qt2)			SP#1-2 (May 1991 on Qt2)		
Depth (cm)	δH-2 ($\pm\sigma$) (V-SMOW)	δO-18 ($\pm\sigma$) (V-SMOW)	Depth (cm)	δH-2 ($\pm\sigma$) (V-SMOW)	δO-18 ($\pm\sigma$) (V-SMOW)
5	-73.240±0.330	-10.534±0.028	5.1	-38.373±0.062	9.810±0.029
15	-74.117±0.320	-11.128±0.059	15.2	-23.439±0.171	11.567±0.028
25	-88.614±0.381	-11.166±0.029	25.4	-30.403±0.250	10.312±0.031
35	-78.024±0.335	- 8.632±0.016	35.6	-31.390±0.376	4.695±0.049
45	-57.596±0.379	- 7.010±0.013	45.7	-48.381±0.077	2.357±0.025
55	-48.804±0.266		55.9	-46.797±0.428	1.476±0.029
65	-40.169±0.073	- 3.257±0.028	66.0	-34.881±0.308	4.130±0.035
75	-42.145±0.111	- 0.461±0.024	76.2	-39.513±0.318	4.360±0.018
85	-41.871±0.165	- 3.298±0.027	86.4	-52.244±0.274	-0.009±0.059
95	-14.173±0.288	- 6.192±0.043	96.5	-55.452±0.294	-0.322±0.033

Appendix 7.2 O and H Isotopic Compositions in Soil Water (Site #9)

	SP#3 (March 1992 on Qt2)		SP#3-2 (May 1992 on Qt2)	
Depth (cm)	δH-2 ($\pm\sigma$) (V-SMOW)	δO-18 ($\pm\sigma$) (V-SMOW)	δH-2 ($\pm\sigma$) (V-SMOW)	δO-18 ($\pm\sigma$) (V-SMOW)
2.5	-58.489±0.172	-4.775±0.051	-38.223±0.408	8.058±0.038
7.6	-66.856±0.480	-5.345±0.042	-30.236±0.284	8.749±0.030
15.2	-84.483±0.189	-8.863±0.054	-44.811±0.224	0.865±0.019
25.4	-82.856±0.194	-8.670±0.040	-60.978±0.414	-3.824±0.030
35.6	-56.623±0.628	-6.555±0.057	-64.200±0.469	-4.296±0.019
45.7	-67.188±0.299	-6.194±0.041	-66.095±0.306	-5.676±0.020
55.9	-65.340±0.332	-4.226±0.037	-67.078±0.175	-5.315±0.061
66.0	-63.301±0.470	-3.059±0.037	-62.245±0.214	-3.186±0.017
76.2	-56.846±0.507	-2.589±0.030	-59.858±0.310	-1.112±0.044
86.4	-49.922±0.295	-1.338±0.052	-49.943±0.246	-1.852±0.012
96.5	-49.735±0.159	-1.928±0.055	-50.419±0.243	-1.315±0.030

Appendix 7.3 O and H Isotopic Compositions in Soil Water (Site #9)

SP#4 (August 1992 on Qt2)			SP#4-2 (October 1992 on Qt2)		
Depth (cm)	δH-2 (±σ) (V-SMOW)	δO-18 (±σ) (V-SMOW)	Depth (cm)	δH-2 (±σ) (V-SMOW)	δO-18 (±σ) (V-SMOW)
			1.3	-57.600±0.260	-1.602±0.025
2.5	-50.332±0.297	-2.671±0.056	3.8	-43.202±0.332	5.861±0.028
7.6	-40.924±0.270	-1.609±0.046	7.6	-12.174±0.073	11.529±0.025
15.2	-34.386±0.145	0.053±0.027	15.2	-19.848±0.252	9.146±0.047
25.4	-35.190±0.162	0.887±0.063	25.4	-29.221±0.399	4.948±0.027
35.6	-43.769±0.318	1.934±0.029	35.6	-41.348±0.126	1.718±0.052
45.7	-53.611±0.169	0.145±0.015	45.7	-48.056±0.394	-1.249±0.024
55.9	-57.153±0.310	-0.613±0.073	55.9	-52.383±0.379	-0.858±0.014
66.0	-56.483±0.252	-1.200±0.016	66.0	-52.464±0.474	-0.645±0.042
76.2	-47.689±0.258	-0.549±0.051	76.2	-52.668±0.329	-0.937±0.025
86.4	-54.752±0.253	-1.124±0.052	86.4	-50.287±0.405	-1.377±0.038
96.5	-53.529±0.182	-1.509±0.050	96.5	-48.415±0.234	-0.686±0.045

Appendix 7.4 O and H Isotopic Compositions in Soil Water SP#2 (March 1992 on Qf2, Site #10)

Depth (cm)	δH-2 ($\pm\sigma$) (V-SMOW)	δO-18 ($\pm\sigma$) (V-SMOW)
1.3	-41.212±0.353	-1.558±0.049
6.4	-58.607±0.261	-4.071±0.031
15.2	-63.588±0.182	-3.775±0.036
25.4	-46.194±0.142	2.105±0.022
35.6	-26.558±0.245	6.758±0.025
45.7	-28.368±0.368	7.297±0.039
55.9	-21.203±0.413	5.861±0.037
66.0	-30.754±0.257	5.036±0.041
76.2	-35.536±0.270	3.356±0.011
86.4	-35.452±0.129	2.979±0.030
96.5	-34.473±0.248	3.286±0.037

Appendix 8 $^{36}Cl/Cl$ Ratios and ^{36}Cl Concentrations in Soil Profile of January, 1991 (Qt2, Site #5)

Depth (cm)	Water Content (wt%)	Cl Concentration (mg/kg soil)	$^{36}Cl/Cl$ ($\pm\sigma$) $(10^{-15})^1$	$^{36}Cl/Cl$ ($+\sigma/-\sigma$) $(10^{-15})^2$	$^{36}Cl/L_{soil\ water}$ $(10^7\ atms)^3$
5	13.6	0.86 (±0.36)	661 (±51)	3824 (+2691/-1148)	41.1 (+ 6.3/- 5.9)
15	13.9	0.98 (±0.12)	1242 (±59)	4121 (+ 620/- 497)	49.2 (+ 4.3/- 4.1)
25	14.5	1.13 (±0.18)	346 (±17)	836 (+ 96/- 67)	11.0 (+ 1.3/- 1.2)
35	14.4	1.42 (±0.13)	189 (±20)	405 (+ 68/- 60)	6.8 (+ 1.1/- 1.0)
45	14.3	1.37 (±0.23)	407 (±29)	768 (+ 135/- 103)	12.5 (+ 2.1/- 1.9)
55	13.4	1.54 (±0.34)	183 (±13)	718 (+ 209/- 141)	14.0 (+ 1.8/- 1.7)
65	11.5	3.26 (±0.19)	591 (±34)	889 (+ 71/- 66)	42.8 (+ 4.2/- 4.0)
75	3.6	1.30 (±0.06)	489 (±26)	1227 (+ 106/- 96)	75.3 (+ 5.4/- 5.4)
85	3.2	1.21 (±0.54)	585 (±36)	1394 (+ 764/- 319)	89.5 (+23.5/-21.0)
95	3.2	1.57 (±0.31)	1196 (±70)	1971 (+ 318/- 238)	164.0 (+31.0/-28.0)

Appendix 8 Cont.

1. Measured $^{36}Cl/Cl$ ratio; 2. The actual $^{36}Cl/Cl$ ratio for soil samples; 3. The actual ^{36}Cl concentration in soil water.

Note: Since stable Cl (sample carrier) was added to soil samples during extracting Cl for $^{36}Cl/Cl$ ratio measurement, the measured $^{36}Cl/Cl$ ratios are the mixed values of soil samples and carrier, and therefore the actual $^{36}Cl/Cl$ ratios and ^{36}Cl concentrations for the soil samples must be corrected by the following equations.

36Cl/Cl ratio correction equation:

$$\left[\frac{36Cl}{Cl}\right]_{soil} = \left[\frac{Cl_{sample} + Cl_{carrier}}{Cl_{sample}}\right]\left[\frac{36Cl}{Cl}\right]_{measured}$$

^{36}Cl concentration Correction Equation:

$$\frac{36Cl_{soil}}{L_{soilwater}} = \left[\frac{Cl_{carrier}}{m_{sample}} + \frac{Cl_{soil}}{L_{soilwater}}\right]\left[\frac{36Cl}{Cl}\right]_{measured}$$

where m is the mass of dry soil in gram, and Cl is the mass of stable Cl in atom.

Appendix 9 Stable Isotope Expressions

1. Definition of isotope fractionation factor between two chemical forms:

$$\alpha_{AB} = \frac{R_A}{R_B} \qquad \text{A9.1}$$

where α_{AB} is the isotope fractionation factor between two chemical forms of A and B, and R is the ratio of a heavier isotope to a lighter isotope.

2. δ notation

Usually, a isotope concentration is reported relative to a standard (e.g., V-SMOW, PDB) in parts per mil as δ notation. For example, for carbon isotope,

$$\delta^{13}C = \frac{R_{sam} - R_{std}}{R_{std}} \times 1000 \quad ‰ \qquad \text{A9.2}$$

where R_{sam} and R_{std} are the ratios of $^{13}C^{16}O_2$ to $^{12}C^{16}O_2$ for a sample and a standard, respectively. A similar expression can be used for oxygen or hydrogen isotope. The international standard for carbon isotope is PDB and for hydrogen and oxygen isotopes it is V-SMOW or PDB for O on carbonates.

3. Equations for calculating isotope fractionation factors

a) Carbon isotope between $CaCO_{3(s)}$ and $CO_{2(g)}$ (Deines et al., 1974)

$$1000\ln\alpha = -3.63 + \frac{1.194 \times 10^6}{T^2} \qquad \text{A9.3}$$

where T is temperature in °K.

b) Oxygen isotope between $CaCO_{3(s)}$ and $H_2O_{(l)}$ (O'Neil et al., 1969)

$$1000\ln\alpha = \frac{2.78 \times 10^6}{T^2} - 3.39 \qquad \text{A9.4}$$

c) Oxygen isotope between $H_2O_{(l)}$ and $H_2O_{(v)}$ (Friedman and O'Neil, 1977)

$$\ln\alpha = \frac{1534}{T^2} - \frac{3.206}{T} + 0.00264 \qquad \text{A9.5}$$

where: s = solid, g = gas, l = liquid, and v = vapor.

4. Conversion from V-SMOW to PDB for oxygen isotope

$$\delta^{18}O_{PDB} = 0.97002\delta^{18}O_{V\text{-}SMOW} - 29.98 \qquad \text{A9.5}$$

Appendix 10 C and O Isotopes in Carbonate

Sample # (Qt2)	Depth (cm)	δC-13 ($\pm\sigma$) (PDB)	δO-18 ($\pm\sigma$) (PDB)
593t2 11	28	-5.112 ±0.022	-4.717 ±0.050
593t2 14	36	-5.747 ±0.024	-5.148 ±0.026
593t2 20	51	-6.467 ±0.025	-6.283 ±0.023
593t2 25	64	-7.520 ±0.037	-5.710 ±0.064
593t2 36	91	-7.895 ±0.069	-5.543 ±0.038
(Qt1)			
593t1 11	28	-5.225 ±0.037	-3.559 ±0.008
593t1 16	41	-5.602 ±0.035	-3.766 ±0.035
593t1 17	43	-5.251 ±0.011	-4.961 ±0.040
593t1 23	58	-5.455 ±0.032	-5.307 ±0.085
593t1 30	76	-6.148 ±0.029	-5.975 ±0.037
593t1 41	104	-6.366 ±0.022	-5.688 ±0.060
(Qf2)			
593f2 8	20	-3.886 ±0.037	-0.980 ±0.050
593f2 12	30	-5.210 ±0.016	-2.733 ±0.041
593f2 16	41	-5.573 ±0.023	-2.958 ±0.077

Appendix 11 Cont.

(Qf1)			
CP#2 4	29	-2.774 ±0.008	-1.313 ±0.021
CP#2 5	36	-2.806 ±0.019	-5.855 ±0.047
CP#1 1	39	-3.442 ±0.034	-5.565 ±0.031
CP#1 2	46	-3.429 ±0.006	-5.813 ±0.045
CP#1 3	57	-3.949 ±0.017	-6.140 ±0.058
CP#1 4	67	-4.004 ±0.023	-6.170 ±0.029
CP#1 5	83	-4.088 ±0.011	-6.140 ±0.024
CP#1 6	93	-4.054 ±0.017	-6.059 ±0.014
CP#1 7	105	-4.207 ±0.012	-6.229 ±0.031
CP#1 8	114	-4.822 ±0.053	-6.658 ±0.023
CP#1 9	124	-5.133 ±0.033	-6.269 ±0.045
CP#1 10	135	-4.930 ±0.017	-6.536 ±0.053
CP#1 11	147	-4.582 ±0.017	-6.177 ±0.028
(Channel)			
593-1	0	-7.300 ±280	-7.931 ±0.055